# Biological Applications of Surfaces with Extreme Wettabilities

by

Sarah A. Snyder

A dissertation submitted in partial fulfillment
of the requirements for the degree of
Doctor of Philosophy
(Materials Science and Engineering)
in the University of Michigan
2019

Doctoral Committee:

Assistant Professor Geeta Mehta, Co-Chair
Assistant Professor Anish Tuteja, Co-Chair
Associate Professor Sunitha Nagrath
Assistant Professor J. Scott VanEpps

Sarah A. Snyder

sarahsny@umich.edu

ORCID iD:  0000-0002-6741-297X

© Sarah A. Snyder 2019

# Dedication

To my parents

## Acknowledgements

First and foremost, I need to thank Prof. Geeta Mehta and Prof. Anish Tuteja. As co-advisors you continually encouraged me to be the best that I can be both academically and personally. I cannot thank you two enough, you not only taught me to push the boundaries with my ideas but also gave me the tools to make those ideas realities. Thanks also to my committee members, Prof. Sunitha Nagrath and Prof. Scott VanEpps. Scott, thank you so much for the insight and encouragement you provided. I have truly enjoyed working with you and your lab.

I want to thank the National Science Foundation's Graduate Research Fellowship Program for their resources and support during my time at the University of Michigan.

To the lab members of both the PSI and ECM groups, thank you. Thank you for the encouragement, thank you for teaching me valuable skills, and thank you for just generally helping me get through the day. Matt, thank you, I could not have done this without all of your help and support. Catherine and Caymen, thank you for always making me smile, you two made lab fun. Thank you Dhyani, I cannot wait to see where you take our project, I've always admired your drive. Shreya, thank you for your guidance and friendship. Chao and Kevin, thank you for shaping me into the scientist that I am today. And thank you Sai, Ethan, Brian, Alex, Brian, Elena, Zoe, Eric, Pooja, Mike, Maria, and Bryce, I will miss you all.

To the lab members of the VanEpps lab, thank you for teaching me how to work with bacteria and how to keep a smile on my face after hours of pipetting. Usha, Erika, Shannon, John, and Harrison, I am so happy to have met and worked with you all. Usha, I wish you all the best with your PhD, I know your work will be great.

I am so grateful for all of the friendships I've made during my time at Michigan. Jill, Erika, Avi, Rosy, and James, it was a pleasure to live with you and I look forward to our next family dinner. Brooke, Patrick, Sean, and Jake, thank you for so many fun memories, I cannot wait to make more.

To my Tucker, Cookies & Cream ('CC'), Milo, Rapunzel ('Punzi') and all my cold-blooded children, thank you for the endless supply of joy and kisses. I love you all so much.

Matthew, words cannot express how thankful I am for all that you have done for me. Thank you for believing in me when I could not believe in myself. I have and will always appreciate you for everything that you've done for me. I also want to thank both the Stephan and Kielty families for their love and support; RJ was a wonderful man and will surely be missed.

They say you can't choose your family, but boy did I luck out. For all of their unwavering love and support, for the endless amount of smiles, and for countless memories, I thank my family. Nanay, Pop-pop, and Grammy, thank you for always believing in me and I hope I've made you proud.

Lastly, mom and dad, I am who am I today because of you. This would all not be possible without your endless love, support, and encouragement. Thank you so much, I will be forever grateful.

## Table of Contents

Dedication ii

Acknowledgements iii

List of Tables viii

List of Figures x

Abstract xix

Chapter 1. Wettability Background 1

- 1.1 Fundamentals of Wetting 1
- 1.2 Design of Superomniphobic Surfaces 2
- 1.3 Robust, Non-wetted States 3

Chapter 2. Paper-Based Surfaces with Extreme Wettabilities for Novel, Open-Channel Microfluidic Devices 5

- 2.1 Introduction 5
- 2.2 Materials and Methods 7
  - 2.2.1 Preparation of Fluorinated Paper Substrates 7
  - 2.2.2 Test Liquids and Dyes 7
  - 2.2.3 Masking of Fluorinated Paper Surface and Selective O2 Plasma Treatment to Produce Microfluidic Devices 8
  - 2.2.4 Printed Channels of Fluoro-Paper B 9
  - 2.2.5 Surface Emulsification on Fluoro-Paper A 10
  - 2.2.6 Patterning of OVCAR3 Cancer Cells on Fluoro-Paper C 11
  - 2.2.7 Characterization Methods 11
- 2.3 Results 12
  - 2.3.1 Generation of All Four Extreme Wettabilities on Fluorinated Paper 12

2.3.2 Generation of 2D and 3D Fluidic Channels on Fluoro-Paper A ........ 20
2.3.3 Printing of Fluidic Channels on Fluoro-Paper B ........ 25
2.3.4 Continuous Oil-Water Separation on Fluoro-Paper A ........ 26
2.3.5 Continuous Liquid-Liquid Extraction on Fluoro-Paper A ........ 28
2.3.6 Surface Emulsification for Particle Fabrication on Fluoro-Paper A ........ 31
2.3.7 Surface Tension/Composition Measurement Using Fluoro-Paper A ........ 34
2.3.8 Ovarian Cancer Cell Microarrays on Fluoro-Paper C ........ 36
2.5 Acknowledgements ........ 39

Chapter 3. Lysis and Detection of Coliforms on a Printed Paper-based Microfluidic Device ..... 40

3.1 Introduction ........ 40
3.2 Materials and Methods ........ 42
3.2.1 Substrate Preparation ........ 42
3.2.2 Ink Preparation ........ 42
3.2.3 Device Fabrication ........ 42
3.2.4 Device Testing ........ 43
3.2.5 Design of Cell Lysis Device ........ 43
3.2.6 E. coli Culture and Growth ........ 44
3.2.7 Lysis-on-a-chip Assay ........ 45
3.2.8 Image Thresholding ........ 45
3.3 Results ........ 45
3.3.1 Printing Omniphilic Channels on an Omniphobic Paper Background ........ 45
3.3.2 Optimization of the Printed Device Design ........ 47
3.3.3 E. coli Detection ........ 50
3.4 Conclusion ........ 52
3.5 Acknowledgments ........ 52

Chapter 4. Long Lasting Antimicrobial Surfaces Based on the Crosslinking of Natural Oils within Polymer Networks ........ 53

4.1 Introduction ........ 53
4.2 Materials and Methods ........ 56
4.2.1 Surface Fabrication ........ 56
4.2.2 Surface Characterization ........ 57
4.2.3 Antibacterial Performance ........ 57
4.2.4 Durability Testing ........ 59

4.3 Results & Discussion ........ 60
  4.3.1 Engineering the surface ........ 60
  4.3.2 Bacterial Testing ........ 63
4.4 Conclusion ........ 69
4.5 Acknowledgements ........ 70
Chapter 5. Summary and Future Work ........ 71

5.1 Paper-Based Surfaces with Extreme Wettabilities for Novel, Open-Channel Microfluidic Devices 71
  5.1.1 Fluoro-paper A ........ 71
  5.1.2 Fluoro-paper C ........ 72
5.2 Lysis and Detection of Coliforms on a Printed Paper-based Microfluidic Device ........ 73
5.3 Long Lasting Antimicrobial Surfaces Based on the Crosslinking of Natural Oils within Polymer Networks ........ 73
5.4 Closing Remarks ........ 74
Appendix ........ 75

References ........ 79

# List of Tables

Table 2.1. Fabrication parameters and the resulting contact angles with water and hexadecane for each of the three different fluorinated paper substrates developed in this work. ................. 14

Table 2.2. $\theta^*_{adv}$, $\theta^*_{rec}$ and contact angle hysteresis ($\Delta\theta$) values for various liquids on fluoro-paper A............................................................................................................................ 16

Table 2.3. Maximum wetting length, *i.e.* the maximum horizontal distance that the liquid front covers, for 20 μL of test liquid placed into channels on fluoro-paper A. The liquid channels are 50 mm in length. ........................................................................................... 21

Table 2.4. Average wetting velocity, *i.e.* maximum wetting length divided by the total wetting time. ......................................................................................................................... 22

Table 2.5. Wetting depth, *i.e.* the vertical distance that the test liquid wets within the channel. The thickness of paper is 390 μm. ........................................................................... 22

Table 4.1. The various individual tea tree and eucalyptus oil components and their relative weight percentages. About 48% of the tea tree oil is capable of reacting with the diisocyanate from the polyurethane while the rest of the tea tree oil is not......................... 61

Table 4.2. Adhered bacteria per unit surface from quantitative culture experiments conducted on surfaces with various essential oils and essential oil components. The lower the number of colony forming units (CFU) on a tested surface, the better their antimicrobial performance. The data is presented as log(CFU). Tested surfaces had a surface area of 100 mm$^2$ and at least three replicates were tested for each surface. ............................................................ 64

Table S.1. Liquid properties (surface tension, viscosity, polarity index, boiling point) of the seven test liquids. .......... 75

## List of Figures

Figure 1.1 A liquid droplet on a smooth solid surface. 1

Figure 1.2. Liquid droplets on textured surfaces. (a) A schematic of a liquid droplet in the Cassie-Baxter state forming a composite solid-liquid-air interface. (b) A schematic of a liquid droplet in the 'fully-wetted' Wenzel state. 3

Figure 2.1 Paper-based surfaces with extreme wettability. (a) A wettability landscape illustrating the concept of surfaces with extreme wettability. The x- and y-axes on this plot vary from the minimum (0º) to the maximum (180º) contact angles for water and oil respectively. Quadrant I (top right on this plot) illustrates omniphobic surfaces, *i.e.* surfaces that are simultaneously hydrophobic and oleophobic. Quadrant II (bottom right) illustrates hydrophobic and oleophilic surfaces. Quadrant III (bottom left) illustrates omniphilic surfaces, *i.e.* surfaces that are simultaneously hydrophilic and oleophilic. Quadrant IV (top left) illustrates hydrophilic and oleophobic surfaces. Values of the robustness factor $A^*$ on the different paper-based surfaces are also provided. (b) An illustration of the changes in wettability of an omniphobic paper (fluoro-paper A) surface upon continuous exposure to $O_2$ plasma. Short exposure time yields a hydrophobic and oleophilic surface. Further $O_2$ plasma exposure yields an omniphilic surface. Extended etching eventually yields a hydrophilic and oleophobic surface due to fluorine recovery, as discussed in the main text. Thus, it is possible to systematically transition between surfaces with all four extreme wettabilities by simply changing the $O_2$ plasma exposure time. 13

Figure 2.2. Fluoro-silanization of different cellulose papers by vapor phase deposition. Typical SEM images of cellulose filter paper (A), cellulose copy paper (B) and cellulose filter paper pretreated by $O_2$ plasma etching (Plasmatherm 790, 200 W, 10 min) (C). Scale bars on SEMs of Type A, B, and C are 100, 100, and 10 mm respectively. .................................... 15

Figure 2.3. $\theta^*_{adv}$ values for various liquids on fluoro-paper A treated by $O_2$ plasma etching for varying times (0–900 sec). ........................................................................................ 17

Figure 2.4. (a-d) SEM images and XPS peak data for fluoro-paper A treated by $O_2$ plasma etching for different times (0–900 sec) showing the dramatic change in the fiber surface texture. All scalebars are 10 μm. (e) XPS spectra at various etching times, with the fluorine 1s and oxygen 1s peaks highlighted. Note the rapid initial decrease in fluorine content and increase in oxygen content as the fluorosilane is replaced by oxygen-rich species from the reactive oxygen plasma. At extended etching times, the redeposition of fluorocarbon fragments on the $O_2$ plasma-etched surface is visible as an increase in the fluorine 1s peak and a decrease in the oxygen 1s peak. The ratio between the peak heights for fluorine and oxygen versus time are plotted in (f). ....................................................................... 18

Figure 2.5. Schematic illustration of the procedure to make a wettability-patterned paper device by selective $O_2$ plasma etching of fluoro-paper A. ............................................................ 20

Figure 2.6. Lateral flow in two-dimensional channels treated by 200 W $O_2$ plasma etching for varying times on fluoro-paper A. (a) Fluoro-paper A devices with straight 50 mm × 2 mm channels that were treated by $O_2$ plasma with etching times between 5 and 900 sec. For different paper devices exposed for each time (increasing from top to bottom), water (blue), DMF (pink), chloroform (black), acetone (light purple), ethanol (light pink), hexane (maroon), and hexadecane (dark red) were tested. The paper substrates were positioned horizontally and each channel was filled with 20 μL of test liquid. Scale bar is 1 cm. (b) Optical image of the cross-section of two-dimensional channels etched for various times filled with seven test liquids. The paper thickness is 390 μm, scale bar is 5 mm. ............... 21

Figure 2.7. Three-dimensional paper device. (a) A schematic illustrating the three-dimensional patterning of fluidic channels on a single piece of paper, by incorporating channels on both sides of a fluoro-paper A substrate. Two groups of channels are patterned orthogonally in the *x*- and *y*-directions. These are labeled as a, b, c, d and 1, 2, 3, 4, respectively. (b and c) The top and bottom of a three-dimensional paper device after being filled with four test liquids: water (blue), DMF (red), heptane (brown) and ethanol (green). Scale bars are 5 mm. ........................................................................................................................ 23

Figure 2.8. (a) Schematic illustration of three-dimensional channels each with a single bridge (fluoro-paper A). The channels are 18 mm long × 2 mm wide. Each bridge was 7.5 mm long and contained an array of five 500 μm diameter perforations on either side. (b) Three-dimensional channels filled with water (dyed blue). (c) Three-dimensional channels filled with DMF (dyed pink) and ethanol (dyed green). (d) Three-dimensional channels filled with heptane (dyed maroon). Scale bars are 1 cm. ...................................................................... 24

Figure 2.9. Mask-free, direct printing of fluidic channels on omniphobic paper. (a) The printing apparatus. (b) A printed pattern on a fluoro-paper B surface. The channels have been filled with silicone oil ($\gamma_{lv}$ = 19.8 mN/m), dyed red. The inset is the 5.3 × 4.4 cm pattern being printed. Scale bar is 5 mm. (c-e) SEM images highlighting the magnified texture for different areas on the patterned surface shown in (b) after the channel is filled with silicone oil. The corresponding areas are labeled as c, d, and e in (a). Scale bars are 50 μm for (c), 500 μm for (d), and 200 μm for (e). ......................................................................... 26

Figure 2.10. (a) Continuous oil-water separation device. A HP/OL channel is combined with a HL/OP channel on a fluoro-paper A surface and used to separate a mixture (50% by volume) of heptane and water. Scale bar is 1 cm. (b) Multiplexed oil-water dispenser, composed of four HL/OP and four HP/OL channels radially arranged from a central reservoir. Any oil or water droplets when added to this reservoir are automatically split and dispensed into four HP/OL or HL/OP channels, respectively. Scale bar is 5 mm. .............. 27

Figure 2.11. Geometry of the device for continuous surface oil-water separation (fluoro-paper A). The HP/OL channel was $O_2$ plasma etched at 200 W for 15 sec, while the HL/OP channel was etched for 900 sec. Scale bar is 5 mm. ........................................................... 27

Figure 2.12. Surface liquid-liquid extraction. (a) A schematic highlighting the design of a device that enables continuous, co-current, liquid-liquid extraction on paper. (b) A HP/OL channel is combined with a HL/OP channel, side-by-side, on a fluoro-paper A surface and used for liquid-liquid extraction. The bottom channel is HL/OP. This channel is filled with water, which serves as the extractant. The top channel is HP/OL and is filled with a mixture of octane and ethanol. Scale bar is 1 cm. ..................................................................... 29

Figure 2.13. (a) Geometry of the device for continuous surface liquid-liquid extraction (fluoro-paper A). The HP/OL channel was etched at 200 W for 15 sec, and the HL/OP channel was etched for 900 sec. Scale bar is 1 cm. (b, c) Refractive index measurements of the feed and extractant before ($F_1$, $E_1$) and after extraction ($F_2$, $E_2$). A calibration curve for each mixture was first obtained by measuring mixtures of known composition (black data points), which was then used to quantify the composition of the test samples. .......................................... 30

Figure 2.14. Control experiment for liquid-liquid extraction. (a) Geometry of side-by-side omniphilic channels patterned on fluoro-paper A, with 200 W $O_2$ plasma etching for 120 sec. (b) Failure to form a clear and stable oil-water interface between the feed and the extractant in the absence of channels possessing selective wettability. Scale bars are 1 cm. ........ 31

Figure 2.15. Paper-based device for microparticle fabrication. (a) A schematic highlighting the design of a flow-focusing geometry for microfluidic emulsification and micro-particle fabrication on paper. (b) The micro-particle fabrication device on a fluoro-paper A surface illustrated in (a). Scale bar is 5 mm. (c) A photograph of the cross-linked micro-particles collected after 1 hour of operation (particles are dyed red and collected in a glass vial). Scale bar is 5 mm. (d) An SEM image of the UV cross-linked micro-particles. Scale bar is 500 μm. ........ 33

Figure 2.16. (a) Surface emulsification apparatus. The syringe pump highlighted in blue is used to control the flow rate of the outer carrier fluid. The other pump, highlighted in red, controls the inner precursor fluid. The area highlighted in yellow includes the paper-based microfluidic device and a glass trough for particle collection. The UV lamp used for crosslinking is highlighted in purple, and would be located above the trough during operation. (b, c) The flow focusing geometry patterned on fluoro-paper A. Scale bar is 1 cm for (b) and 5 mm for (c). ........ 34

Figure 2.17. Measurement of the surface tension/composition of mixtures. A paper-based alcoholmeter developed on a fluoro-paper A surface. The alcoholmeter consists of patterned HP/OL channels on an omniphobic background. ........ 35

Figure 2.18. Schematic illustration of the procedure employed to prepare omniphobic fluoro-paper C, omniphobic-omniphilic patterns on this surface, and their use for generating patterned OVCAR3 cell arrays. Scale bars on the SEMs are 10 μm. All other scale bars are 1 cm. 37

Figure 2.19. Generation of cell microarrays on surfaces with patterned wettability. (a-f) Growth of OVCAR3 (ovarian cancer) cells on an omniphobic (fluoro-paper C) surface patterned with omniphilic domains. This paper has a high $A^*$ value for the growth culture medium used, ensuring longevity of the non-wetted state while immersed. The cells preferentially grow on the omniphilic regions and not on the omniphobic background. Scale bars are 500 μm in (a), (b), 200 μm in (c), (d), and 50 μm in (e), (f). 38

Figure 3.1. The fabrication and characterization of the paper-based *E. coli* detection devices. a) The steps required to manufacture a complete *E. coli* detection device, including $O_2$ plasma cleaning, vapor phase silanization with a fluorinated silane, printing of the $TiO_2$ channels and exposure of the devices to 254 nm UV light. b) 20 μL of water wetting channels printed with and without ink containing $TiO_2$. The UV activated $TiO_2$ containing ink allows high surface energy water to easily wet the channel. c) The omniphilic channel printing apparatus developed using an XYZ stage can be utilized to print any device design. d) An SEM image shows the $TiO_2$ thin film on top of the silanized copy paper. e & f) Liquid drops repelled and contained on the omniphobic and superomniphilic regions, respectively. g) A channel in the shape of a single *E. coli* bacterium filled with dyed silicone oil ($\gamma_{lv}$ = 22 mN/m), demonstrates the ability to confine low surface tension liquids and to print any desired microfluidic channel shape with this technique. 46

Figure 3.2. Optimization of device design to achieve complete mixing. a) Concentration profiles generated from COMSOL models of lysis devices with zero or seven turns in the mixing channel. Dark red represents a 100% concentration of liquid A and dark blue represents a

100% concentration of liquid B. (b-c) Images demonstrating the effective mixing in the serpentine region of the device with (b) dyed water and (c) LB and 2X B-PER. The addition of more turns in the serpentine region increased mixing, allowing for nearly homogenous mixing in the 7-turn device. .......................................................................................... 48

Figure 3.3. Optimization of the detection patch design. a) RGB schematic with a white outlined box showing the colors contained within the thresholding limits of R >140, G < 200, and B < 200. All pixels with RGB values within those limits indicate a color change and are counted, and pixels with RGB values outside those limits are ignored. b) Bright field images and corresponding processed images via thresholding for both circular and diamond shaped detection patches. c) Counted pixels per unit area of the processed images for both circular and diamond shaped detection patches. With a higher number of counted pixels, diamond shaped detection patches exhibit a statistically significant (*p* = 0.0228) increase in sensitivity compared to circular detection patches. ........................................................... 49

Figure 3.4. *E. coli* lysis and detection results on the paper-based device. a) *E. coli* lysed on chip at a concentration of ~$10^7$ CFU mL$^{-1}$ with the *E. coli* inlet, 2X B-PER lysis buffer inlet and the CPRG detection patch labeled. The *E. coli* spent approximately 1 minute mixing with the lysis buffer in the serpentine region before reaching the detection patch, and there was a noticeable color change within 5 minutes at the detection patch. After 15 minutes, the color change nearly reached completion. b) The growth curve and corresponding color change images with their respective processed images on the lysis devices for ~1 CFU mL$^{-1}$ incubated in medium over time. With a minimal detection limit of ~$10^4$ CFU/mL after 6 hours of incubation, there was a noticeable onset of color change...................................... 51

Figure 4.1. A schematic showing free oil (red circles) stabilized by oil crosslinked (blue circles) into the crosslinkable polymer (polyurethane in this case) network (black lines). While some free oil remains in the bulk, most assembles onto the surface. .................................. 62

Figure 4.2. Thermogravimetric analysis (TGA) data of the Desmo PU (red), Desmo PU reacted with 30% TTO (blue), and Desmo PU swelled in TTO (green) at the 200 °C isotherm. Desmo PU loses ~2 wt % while Desmo PU reacted with TTO loses ~12 wt %, indicating the presence of ~10 wt % of free oil in the reacted samples. The Desmo PU that was simply swelled with TTO loses ~29 wt % and when compared to the Desmo PU reacted with TTO sample, the higher weight loss percentage is attributed to the lack of TTO stability within the Desmo PU network, both chemically and physically. Thus, reacting in the TTO with the Desmo PU instead of simply swelling the PU fabricates a more stable PU + TTO network. ........................................................................................................................ 63

Figure 4.3. Bar graph representation of the adhered bacteria data for various surfaces and various surface testing conditions with both *E. coli* (blue) and *S. aureus* (red). All PU surfaces reacted with 30% TTO show at least a ~2.4 log reduction of adhered bacteria when compared to the PS and PU controls, with the fresh PU + 30% TTO samples showing a 99.8% and 99.9% reduction of adhered bacteria with *E. coli* and *S. aureus*, respectively, when compared to the Desmo PU. Results are similar with the abraded samples (99.6% and 99.9% of adhered *E. coli* and *S. aureus*, respectively, when compared to the Desmo PU), demonstrating the physical durability of the surface. Even after 8 and 12 weeks of exposure in a chemical fume hood, the PU + 30% TTO samples show a significant reduction in adhered bacteria: at least 99% for both *E. coli* and *S. aureus*, when compared to the Desmo PU. In comparison, while the Epoxy + 30% TTO and PDMS + 30% TTO surfaces initially show a ~2 log reduction in adhered bacteria, the Epoxy + 30% TTO, 2 weeks and PDMS + 30% TTO, 2 weeks surfaces showed significant fouling. This can be attributed to the fact that tea tree oil does not chemically crosslink into epoxy and PDMS, and therefore, the free oil is not stabilized in the polymeric network. ..... 66

Figure 4.4. ISO 22196 test results as performed by Microchem Laboratory. Results indicate a 99.998% and a >99.995% reduction for *E. coli* and *S. aureus*, respectively, and are consistent with our antibacterial experiments. ..... 67

Figure 4.5. Contact plate experiments aimed at determining the time taken for the polyurethane crosslinked with tea tree oil surface to kill *S. aureus* bacteria. This image shows the total number of colonies of *S. aureus* that grow on an Agar plate after a 100,000 colonies of the bacteria come in contact with a polystyrene surface, a polyurethane surface or the same polyurethane surface crosslinked with tea tree oil for 10 minutes ..... 68

Figure 5.1. Top view and side view schematics of patterned fluoro-paper C being utilized as a Transwell® like device. ..... 72

Figure 5.2. Example schematic of malaria detection on an all-in-one, open-channel, paper-based microfluidic device. ..... 73

# Abstract

Surfaces with extreme wettabilities have become an increasingly popular topic due to their wide range of applications – from simply keeping dirt off clothing to oil-water separation in the event of an oil spill. In particular, these surfaces have been of keen interest for a diverse range of biological applications as they can be fabricated from biocompatible materials.

First, a facile methodology involving fluoro-silanization followed by oxygen plasma etching, for the fabrication of surfaces with extreme wettabilities is discussed. Open channel, paper-based microfluidic devices fabricated using these surfaces with extreme wettabilities allow for the localization, manipulation, and transport of virtually all high- and low- surface tension liquids. This in turn expands the utility of paper-based microfluidic devices to a range of applications never before considered. These include, continuous oil-water separation, liquid-liquid extraction, open-channel microfluidic emulsification, micro-particle fabrication, the precise measurement of a mixtures' composition, and cell patterning.

Next, a particular paper-based microfluidic device is expanded upon for the detection of *E. coli* and all coliforms. Coliforms are one of the most common families of bacteria responsible for water contamination, and certain pathogenic strains can be extremely harmful, leading to death if consumed. Current technologies for detection are expensive, requiring bulky setups, and can take up to 24 hours to produce accurate results. In this work, we have created an integrated microfluidic coliform lysis and detection device, the first of its kind to demonstrate successful lysing on-chip as it can allow for the flow and control of both high and low surface tension. The fabricated, optimized microfluidic device was able to successfully detect *E. coli*, via the presence

of the coliform-specific enzyme, $\beta$-galactosidase. These devices can be implemented for real world *E. coli* contamination detection in multiple applications, including food and water safety.

Finally, antifouling and antibacterial surfaces have been of extreme interest due to a plethora of potential applications. Many natural oils, including tea tree oil, possess antimicrobial properties. However, these oils are typically volatile, and depending on the environment can evaporate from a surface within a few minutes to several hours. In this work, we produce long lasting antimicrobial surfaces by partially crosslinking different natural oils within a cross-linkable polyurethane matrix. The remaining free oil is then stabilized by the partially crosslinked oil, yielding an antimicrobial surface that can remain antimicrobial for extended periods of time. These surfaces exhibit significant reductions in attached bacteria and there is currently no other known antimicrobial surface with this combination of instant and persistent kill.

Taken together, this thesis lays the building blocks for a plethora of current and future biological applications of surfaces with extreme wettabilities.

# Chapter 1. Wettability Background

Surfaces exhibiting extreme wettabilities, omniphobic (all liquids non-wetting *i.e.* contact angle > 90°)[1] or omniphilic (all liquids wetting *i.e.* contact angle < 90°)[2], have been of interest to many researchers because of their potential for a wide variety of applications. The information presented in this chapter lays the foundation for the science behind this entire dissertation.

## 1.1 Fundamentals of Wetting

All extreme wettability surfaces are engineered by varying two key material parameters: surface energy and roughness. Young's equation,[3] governed by a minimization of surface energy, relates a liquid's contact angle ($\theta_E$) on an ideal, smooth surface to the relative solid-vapor, solid-liquid, liquid-vapor surface tensions ($\gamma_{sv}$, $\gamma_{sl}$, & $\gamma_{lv}$, respectively), $\cos\left(\theta_E\right) = \left(\nu_{sv} * \nu_{sl}\right) / \nu_{lv}$. Figure 1.1 displays a static liquid droplet resting on a smooth surface with equilibrium contact angle, $\theta_E$.

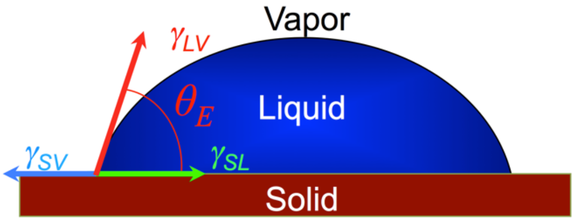

**Figure 1.1** A liquid droplet on a smooth solid surface.

On real surfaces, a range of contact angles may be measured, from a maximum advancing contact angle exhibited when liquid is added to a droplet on the surface, to a minimum receding contact angle exhibited when liquid is removed from the droplet. Contact angle hysteresis ($\Delta\theta$) is defined as the difference between the advancing contact angle ($\theta_{adv}$) and the receding contact angle ($\theta_{rec}$): $\Delta\theta = \theta_{adv} - \theta_{rec}$.[4] For most applications, surfaces are designed to minimize $\Delta\theta$ to promote or maximize droplet mobility on a surface.[1, 2] However, particular applications, like the printing of ink on an omniphobic background, require a maximization of $\Delta\theta$ so the ink drags or prints onto the particular surface.[5]

## 1.2 Design of Superomniphobic Surfaces

A droplet of liquid on a rough substrate can adopt one of the following two configurations to minimize its overall free energy.[6, 7] In the first case, the liquid droplet may completely wet a given surface, covering all of the surface features that are present underneath the droplet. Such complete surface coverage leads to the so-called 'fully-wetted' interface or the Wenzel state (Figure 1.2b)[8].

On the other hand, on a sufficiently rough surface, a 'composite' interface may lead to a lower overall free energy. In this case, the rough surface is not fully wetted by the liquid, and pockets of air remain trapped underneath the liquid droplet. The apparent contact angle in this state is typically calculated using the Cassie-Baxter model,[9] (Figure 1.2a) given as

$$\cos\theta^* = r_\varphi \varphi_s \cos\theta - (1 - \varphi_s) \tag{1}$$

where $\theta$ is the Young's contact angle, *i.e.* the contact angle on a smooth non-textured surface,[3] $\theta^*$ is the apparent contact angle on a textured surface, $\phi_s$ is the projected area of the wetted solid over the total projected area, and $r_\phi$ is the roughness of the wetted solid. A textured surface can yield either a fully wetted or a composite interface with a given liquid as determined by the overall free energy of the system.[7, 10-12] A composite interface is required for surfaces to display very high contact angles with different liquids. We have previously shown that the presence of re-entrant texture is critical for a surface to achieve a composite interface with extremely low surface tension liquids, such as different oils and alcohols.[13-15]

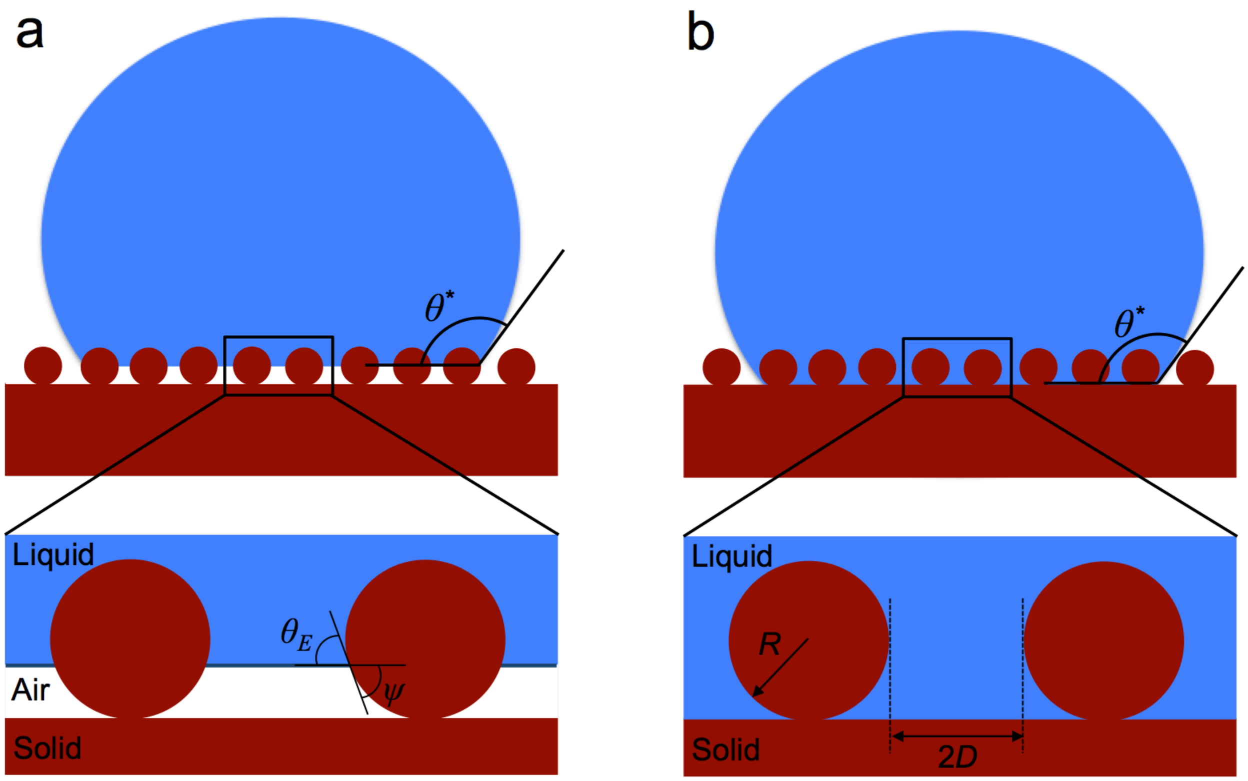

**Figure 1.2.** Liquid droplets on textured surfaces. (a) A schematic of a liquid droplet in the Cassie-Baxter state forming a composite solid-liquid-air interface. (b) A schematic of a liquid droplet in the 'fully-wetted' Wenzel state.

## 1.3 Robust, Non-wetted States

The two important physical characteristics for a composite state on a textured surface with a particular contacting liquid are (i) the robustness of the composite interface to pressure perturbations and (ii) the areal fraction ($1 - \phi_s$ in Eq. 1) of the air/vapor pockets within the composite interface, as a larger areal fraction typically yields higher contact angles with a given liquid. The breakthrough pressure ($P_b$) is defined as the pressure at which a given composite interface is disrupted by sagging of the liquid-vapor interface.

A dimensionless design parameter, $A^*$, is used to predict the robustness of the composite interface, which is defined as $A^* = P_b / P_{ref}$. $P_{ref}$ is a characteristic reference pressure, given as $P_{ref} = 2\gamma_{lv}/\ell_{cap}$. Here $\ell_{cap} = \sqrt{\gamma_{lv}/\rho g}$, where $\gamma_{lv}$ is the surface tension of the liquid, $\rho$ is the fluid density, and $g$ is the acceleration due to gravity. As defined, $P_{ref}$ is close to the minimum pressure difference across the composite interface for millimetric or larger liquid droplets or puddles.[16]

For a texture that is dominated by periodic cylindrical features, such as the fibrous paper samples considered here, the robustness parameter $A^*$ may be calculated as

$$A^* = \frac{P_{breakthrough}}{P_{ref}} = \frac{R\ell_{cap}}{D^2}\left(\frac{1-\cos\theta}{1+2(R/D)\sin\theta}\right) \tag{2}$$

Here $R$ is the fiber radius and $D$ is half of the space between adjacent cylinders (Figure 1.2b). Large values of the robustness factor ($A^* >> 1$) indicate the formation of a robust composite interface, with very high breakthrough pressures, while $A^* < 1$ predicts complete wetting of the rough interface. Our previous work has shown that the $A^*$ parameter does a good job of providing an *a priori* estimation of experimentally measured breakthrough pressure.[15, 16]

# Chapter 2. Paper-Based Surfaces with Extreme Wettabilities for Novel, Open-Channel Microfluidic Devices

This chapter is an excerpt from an article published in *Advanced Functional Materials[5]* authored with Dr. Chao Li and Dr. Mathew Boban. Sarah Snyder contributed to a substantial portion of the experiments and helped edit the manuscript.

## 2.1 Introduction

Surfaces exhibiting extreme wettabilities (Figure 1a), hydrophobic (HP)/oleophobic (OP) (omniphobic, all liquids non-wetting),[15] HP/oleophilic (OL) (water non-wetting, oil wetting),[14] hydrophilic (HL)/OP (water wetting, oil non-wetting),[17] and HL/OL (omniphilic, all liquids wetting),[18] have a large number of applications including chemical and biological protection, oil-water separation, stain-resistant textiles, 'non-stick' coatings, controlling protein and cell adhesion on surfaces, reduction of biofouling, and enhanced heat transport. However, there is no established technique that allows for selectively generating and patterning all four extreme wettabilities[19, 20] on a single surface, especially at the length scale necessary for microfluidic control. In this work, we discuss a facile methodology for the fabrication of surfaces with extreme wettabilities by selectively modifying the surface energy and roughness of different paper surfaces.

Paper has recently emerged as a promising materials platform for microfluidic devices due to its low cost, easy disposal, high surface area, capillary-based wetting, flexibility, and compatibility with a wide range of patterning and printing techniques.[21] Since the first report of using paper as a base material in microfluidics by Whitesides *et al.* in 2007,[22] a new era of paper-based microfluidic devices has arisen.[23-27] The ability to pattern wetting/non-wetting channels on paper has allowed multiplexed, small-volume fluid control both in two-dimensional lateral flow on a single surface[28-34] and three-dimensional flow on stacked layers connected through pores.[35-40]

Generally, fluidic channels introduced on paper surfaces are composed of wettable domains bounded by non-wettable domains, or by air gaps.[41-44] In most cases, paper-based microfluidic channels have been developed to contain only water or aqueous solutions.[45] Few reported techniques used for generating patterned wettability on paper result in devices compatible with even a limited number of non-aqueous liquids.[46-48] Further, the wettable channels in the paper-based microfluidic systems reported thus far show no selective wettability with liquids possessing different surface tensions and/or polarities. In other words, all liquids wet these fluidic channels. Overall, there is no established technique that allows for the selective generation of all four "extreme wettabilities" [19, 20] on paper-based microfluidic channels; that is, the four possible combinations of wetting of oil (oleophilic – OL or oleophobic – OP) and water (hydrophilic – HL and hydrophobic – HP) on a surface. The four extreme wettabilities are: HP/OP (omniphobic, all liquids non-wetting),[15] HP/OL (water non-wetting, oil wetting),[14] HL/OP (water wetting, oil non-wetting),[17] and HL/OL (omniphilic, all liquids wetting).[18]

In this work, we have developed a method of generating omniphobic paper surfaces that are resistant to wetting by a broad range of liquids, including numerous low surface tension solvents. Further, we have also developed a methodology to induce selective wetting of liquids with different surface tensions and polarities on a paper surface. This allows us to realize the four extreme wettabilities with oil and water, as discussed above, on paper surfaces. Such selective extreme wettabilities of fluidic channels, combined with improved fluidic control, make several new applications of paper-based microfluidic devices possible. These applications rely on the separation or compartmentalization of liquids based on their surface tensions and/or polarities, and include oil-water separation, liquid-liquid extraction, droplet generation for micro-particle fabrication, and the measurement of the surface tension/composition of a mixture.

## 2.2 Materials and Methods

### *2.2.1 Preparation of Fluorinated Paper Substrates*

Substrates were either cellulose filter papers (GE Life Sciences, Whatman Grade 3, pore size 6 μm, thickness 390 μm) or cellulose copy paper (Boise X-9 Multiuse OX9001, OfficeMax). Fluorosilanes, (heptadecafluoro-1,1,2,2-tetrahydrodecyl trichloro-silane and heptadecafluoro-1,1,2,2-tetrahydrodecyl triethoxy-silane), were purchased from Gelest. Asahiklin AK-225 (dichloropentafluoropropane) was purchased from SPI Supplies. All of the materials and reagents were used as received. See Table 1 for a summary of the three types of fluoro-paper developed in this manuscript.

For fluoro-paper A, each batch of cellulose filter papers was treated with trichlorosilane (400 μL per 400 $cm^2$, an excess quantity) by vapor phase deposition in a vacuum oven (Precision Scientific, 50 °C, < 5 mmHg) for 18 hours. After fluorosilanization, the paper was soaked in AK--225 for 24 hours to remove the unreacted fluorosilanes.

### *2.2.2 Test Liquids and Dyes*

Deionized water was generated with a Pall Corporation Cascada RO-water purification system. Other test liquids: DMF, chloroform, acetone, methanol, ethanol, and alkanes (n-hexane, n-heptane, n-octane, n-decane, n-dodecane, n-hexadecane), were all purchased from Fisher Scientific (see Table S.1 in the Appendix for liquid properties). Solvent Blue 38, Disperse Red 1, Methylene Blue Indicator (MBI) (Sigma Aldrich), and food coloring (McCormick) were used to dye polar liquids. Oil Red O (Alfa Aesar) was used to dye non-polar liquids.

### *2.2.3 Masking of Fluorinated Paper Surface and Selective O2 Plasma Treatment to Produce Microfluidic Devices*

Fluoro-paper A was masked by Kapton polyimide adhesive tape (3.175, 6.35, or 12.5 mm wide, 25.4 μm thick, purchased from ULINE) by manual application. The masked paper was selectively $O_2$ plasma etched (Plasmatherm 790, chamber vacuum 20 mTorr, $O_2$ flow rate 20 sccm, bias RF source power 200 W-350 W) to obtain functional devices. Plasma etching time was varied to obtain the desired wettability in each channel. The maximum wetting length, average wetting velocity, and wetting depth were characterized for a range of liquids for different times in simple two-dimensional channels (Appendix section 1.1; Tables 2.3-2.5). Functional devices for oil-water separation, liquid-liquid extraction, droplet emulsification, and surface tension measurement were produced by this masked $O_2$ plasma etching method and are described in the main text.

To fabricate a three-dimensional paper device, both sides were masked in the desired geometry, and arrays of 500 μm diameter perforations were manually introduced at the appropriate locations to allow liquid to transfer to the opposite side of the paper. $O_2$ plasma etching was applied onto both sides to make the channels wettable to the target liquids, with varying times to obtain maximum wettability for each target liquid. The $O_2$ plasma etching was optimized for channels with one, two, and four bridges for each target liquid, with increasing time and power required for more bridges (Appendix section 1.2; Figure 2.7 & 2.8). For four bridges, the optimal etching times were: 180 sec for water channels, 60 sec for DMF channels, 30 sec for heptane channels, and 15 sec for ethanol channels, all with the plasma power set at 350 W.

### *2.2.4 Printed Channels of Fluoro-Paper B*

A mask-free patterning method to generate channels was developed by directly depositing high surface energy material on fluoro-paper B. Compared to fluoro-paper A, the nearly zero receding contact angles for both water and oil on the fluoro-paper B guaranteed good contact and adhesion between the ink and the paper surface, with no dewetting during application. Meanwhile, the retention of high advancing contact angles prevented the ink from further wicking or spreading on the surface of fluoro-paper B.

The ink was a water-based polyurethane (Aleene's Fabric Fusion permanent fabric adhesive), dissolved in ethanol to make a 500 mg/mL solution, and then diluted 1 : 3 by volume with a 20 mg/mL sodium dodecyl sulfate aqueous solution. The final solution was probe sonicated (Heat Systems Ultrasonic Processor Sonicator) for 2 min and filtered through a 0.2 μm syringe filter. This material formed uniform, colorless films, with minimal dewetting (related to surface tension, viscosity, and evaporation rate of the ink), excellent adherence to the paper, and was wet by most liquids other than water.

The ink was selectively applied to the paper with a lab-made printing apparatus (Figure 2.9). The printing head is a tapered polypropylene dispensing nozzle (24 gauge or 570 μm outer diameter, McMaster-Carr) connected via silicone tubing (1/16” inner diameter, McMaster-Carr) to a syringe pump (KD Scientific Model 200) operating at 1 mL/h. A motorized XYZ motion stage (Shapeoko 2) allows selective deposition. The motion of each axis was computer-controlled, as was the syringe pump. The fluoro-paper B substrates were temporarily attached to glass plates with a spray adhesive, which were then mounted to a carefully leveled hot plate held at 45 °C.

Patterns for the XYZ platform were generated by drawing them in vector graphics software (Inkscape) and then converting them to G-code commands. The pattern chosen was a line drawing of the Lurie Bell Tower at the University of Michigan, with an overall size of 5.3 cm × 4.4 cm. When ~25 μL of low viscosity silicone oil (dyed with Oil Red O) was placed in each of the four reservoirs, the whole pattern was completely filled, with wetting driven only by capillary forces.

### *2.2.5 Surface Emulsification on Fluoro-Paper A*

An outer HL/OP channel (200 W $O_2$ plasma etched, 300 sec) was integrated with an inner HP/OL channel (200 W $O_2$ plasma etched, 15 sec). The common boundary between the channels was designed to be a flow-focusing nozzle (Figure 2.16). The HL/OP channel was filled with a continuously flowing carrier fluid (2 wt.% aqueous solution of sodium dodecyl sulfate, purchased from Hoefer). The HP/OL channel was filled with a continuously flowing crosslinkable polymer (1,1-trimethylolpropane triacrylate (TMPTA, purchased from Polysciences) with 5% wt. initiator (2-hydroxy-2-methylpropiophenone, purchased from Sigma Aldrich)). The geometry of the two channels and the flow rates of the precursor and carrier fluids (1500 μL/min and 5 μL/min, respectively, controlled by independent syringe pumps (KD Scientific KDS-230)) forced the formation of monodisperse droplets of the UV crosslinkable precursor in the carrier fluid. These droplets were carried downstream to a UV lamp (UVP BLAK-RAY B-100SP, 140 W, 365 nm) which caused them to cross-link and solidify. The particles were then collected and imaged.

### *2.2.6 Patterning of OVCAR3 Cancer Cells on Fluoro-Paper C*

All tissue culture reagents were purchased from Life Technologies (Carlsbad, CA) unless specified otherwise. The growth medium used was phenol red free RPMI 1640 supplemented with 10% fetal bovine serum, 1X L-Glutamine and 1X Antibiotics/Antimycotics. Human ovarian adenocarcinoma cell line, NIH:OVCAR3, was purchased from ATCC (Manassas, VA).

Fluoro-paper C substrates were covered with porous stainless steel masks with patterns of squares (500 μm × 500 μm, 1.5 mm spacing) and stripes (500 μm wide, 1.5 mm spacing) purchased from Metal Etch Services. Omniphilic domains were obtained on an omniphobic background with $O_2$ plasma etching (Plasmatherm 790, chamber vacuum 20 mTorr, $O_2$ flow rate 20 sccm, bias RF source power 30 W for 2 min) (Figure 2.18). The patterned paper was sterilized by exposure to a 254 nm germicidal UV lamp for 2 hours.

Cells were cultured in growth medium until ~80% confluency and then trypsinized per regular passage. Counts were performed with a hemocytometer and 0.75 million cells were plated on each paper sample with 5 ml growth medium in a 6-well plate. The samples were incubated for 10 hours at 37 °C with 5% $CO_2$ and then stained with iodonitrotetrazolium chloride (Sigma-Aldrich). Samples were rinsed once with 1X Dulbecco's Phosphate-Buffered Saline (DPBS) and allowed to air dry prior to imaging with an Olympus BX-51 visible light microscope.

### *2.2.7 Characterization Methods*

Photographs and video were recorded by a digital camera (Casio EX-F1). SEM images were acquired with a Hitachi SU8000 ultra-high resolution SEM with an accelerating voltage of 10 kV. XPS analysis was conducted using a Kratos Axis Ultra XPS. The monochromatic Al-Kα X-ray source was operated at 15 kV and 10 mA. Photoelectrons were collected at a takeoff angle of ~65° relative to the sample surface. Wide-scan survey spectra were acquired at an analyzer pass energy of 160 eV and a step size of 1 eV. O 1s, F 1s and C 1s high-resolution spectra were collected at an analyzer pass energy of 60 eV and a step size of 1 eV.

All contact angle measurements were obtained using a Ramé-Hart 200-F1 goniometer. 3 μL droplets were used for static contact angle measurement. The advancing and receding contact angles measurements were performed starting with a 3 μL droplet on the surface and then growing and shrinking it by adding and removing a small volume (~2 μL) using a 2 mL micrometer syringe (Gilmont) while continually measuring contact angles. Contact angle hysteresis was calculated as the difference between advancing and receding contact angles. At least three measurements were performed on each sample surface. Typical error in measurements was ± 2°.

To measure $A^*$, a series of droplets of varying volume were put on sample surfaces. A higher Laplace pressure can be expected from a smaller droplet due to the increase in curvature.[49] A decrease in the apparent contact angle of droplet will result from an increase in Laplace pressure as it causes the composite interface to sag deeper into the texture. The apparent contact angle was measured with the goniometer. If the apparent contact angle was below 90° with a specific droplet volume, the droplet was considered to have wetted the surface, and the corresponding Laplace pressure considered to be greater than the breakthrough pressure for the surface. $A^*$ can then be calculated as the Laplace pressure divided by the reference pressure.

## 2.3 Results

### *2.3.1 Generation of All Four Extreme Wettabilities on Fluorinated Paper*

We first developed an omniphobic cellulose paper that resists wicking or spreading of most liquids, including low surface tension solvents (Figure 2.1a, quadrant I). This surface was prepared by fluoro-silanization of commercially available cellulose filter paper (Methods). The re-entrant texture of the cellulose fibers, combined with the low surface energy of the fluoro-silane, yielded a porous omniphobic substrate, referred to as fluoro-paper A (Table 2.1; Figure 2.2).

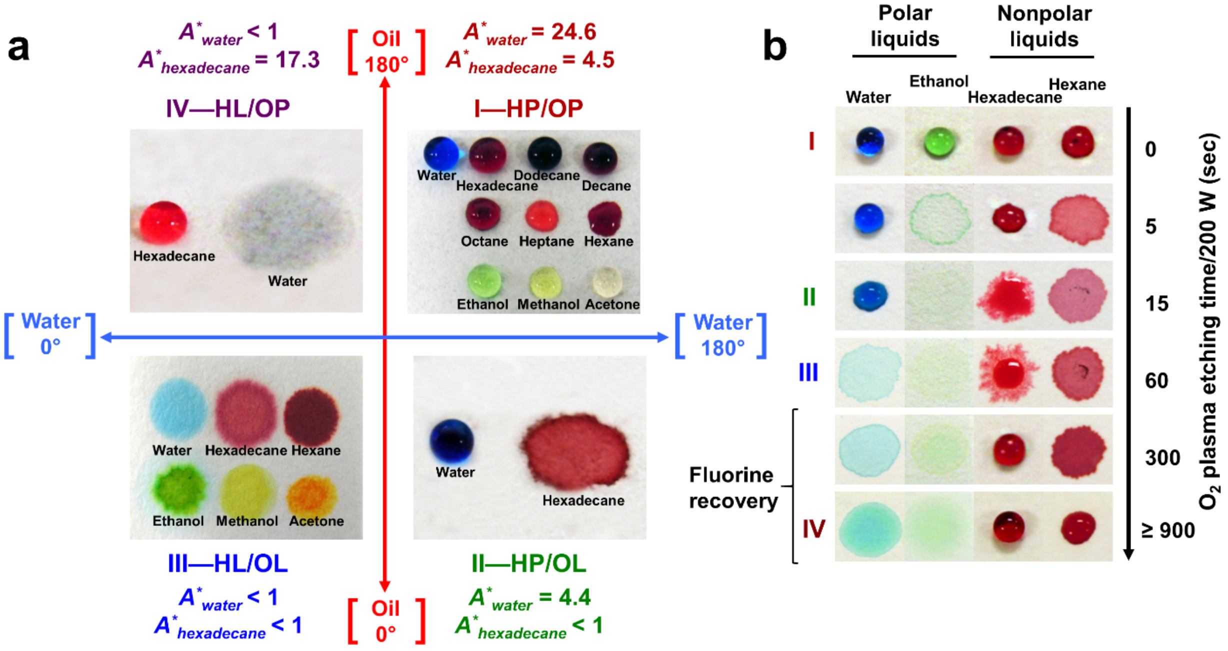
a
A*water < 1
A*hexadecane = 17.3
Oil 180°
A*water = 24.6
A*hexadecane = 4.5
IV—HL/OP
I—HP/OP
Hexadecane
Water
Water
Hexadecane
Dodecane
Decane
Octane
Heptane
Hexane
Ethanol
Methanol
Acetone
Water 0°
Water 180°
Water
Hexadecane
Hexane
Ethanol
Methanol
Acetone
Water
Hexadecane
III—HL/OL
A*water < 1
A*hexadecane < 1
Oil 0°
II—HP/OL
A*water = 4.4
A*hexadecane < 1
b
Polar liquids
Nonpolar liquids
Water
Ethanol
Hexadecane
Hexane
I
II
III
IV
Fluorine recovery
0
5
15
60
300
≥ 900
O2 plasma etching time/200 W (sec)

**Figure 2.1** Paper-based surfaces with extreme wettability. (a) A wettability landscape illustrating the concept of surfaces with extreme wettability. The x- and y-axes on this plot vary from the minimum (0º) to the maximum (180º) contact angles for water and oil respectively. Quadrant I (top right on this plot) illustrates omniphobic surfaces, *i.e.* surfaces that are simultaneously hydrophobic and oleophobic. Quadrant II (bottom right) illustrates hydrophobic and oleophilic surfaces. Quadrant III (bottom left) illustrates omniphilic surfaces, *i.e.* surfaces that are simultaneously hydrophilic and oleophilic. Quadrant IV (top left) illustrates hydrophilic and oleophobic surfaces. Values of the robustness factor $A^*$ on the different paper-based surfaces are also provided. (b) An illustration of the changes in wettability of an omniphobic paper (fluoro-paper A) surface upon continuous exposure to $O_2$ plasma. Short exposure time yields a hydrophobic and oleophilic surface. Further $O_2$ plasma exposure yields an omniphilic surface. Extended etching eventually yields a hydrophilic and oleophobic surface due to fluorine recovery, as discussed in the main text. Thus, it is possible to systematically transition between surfaces with all four extreme wettabilities by simply changing the $O_2$ plasma exposure time.

**Table 2.1.** Fabrication parameters and the resulting contact angles with water and hexadecane for each of the three different fluorinated paper substrates developed in this work.

| Fluoro-paper | Substrate | Silanization conditions | Contact angles [°] | | | | $A^*$ | | |
|---|---|---|---|---|---|---|---|---|---|
| | | | Water | | Hexadecane | | Water | Hexa-decane | Cell medium |
| | | | $\theta^*_{adv}$ | $\theta^*_{rec}$ | $\theta^*_{adv}$ | $\theta^*_{rec}$ | | | |
| **A** | filter paper | 50 °C, < 5 mmHg, 18 h trichlorosilane | 161 | 143 | 136 | 103 | 24.6 | 4.5 | - |
| **B** | copy paper | 70 °C, < 5 mmHg, 24 h trichlorosilane | 153 | 0 | 113 | 0 | 19.3 | 3.1 | - |
| **C** | filter paper | 120 °C, < 5 mmHg, 24 h triethoxysilane | 167 | 157 | 162 | 128 | > 45.0 [a)] | 13.6 | 25.4 |

[a)] No breakthrough could be observed for the minimum measurable droplet size (1 nL)

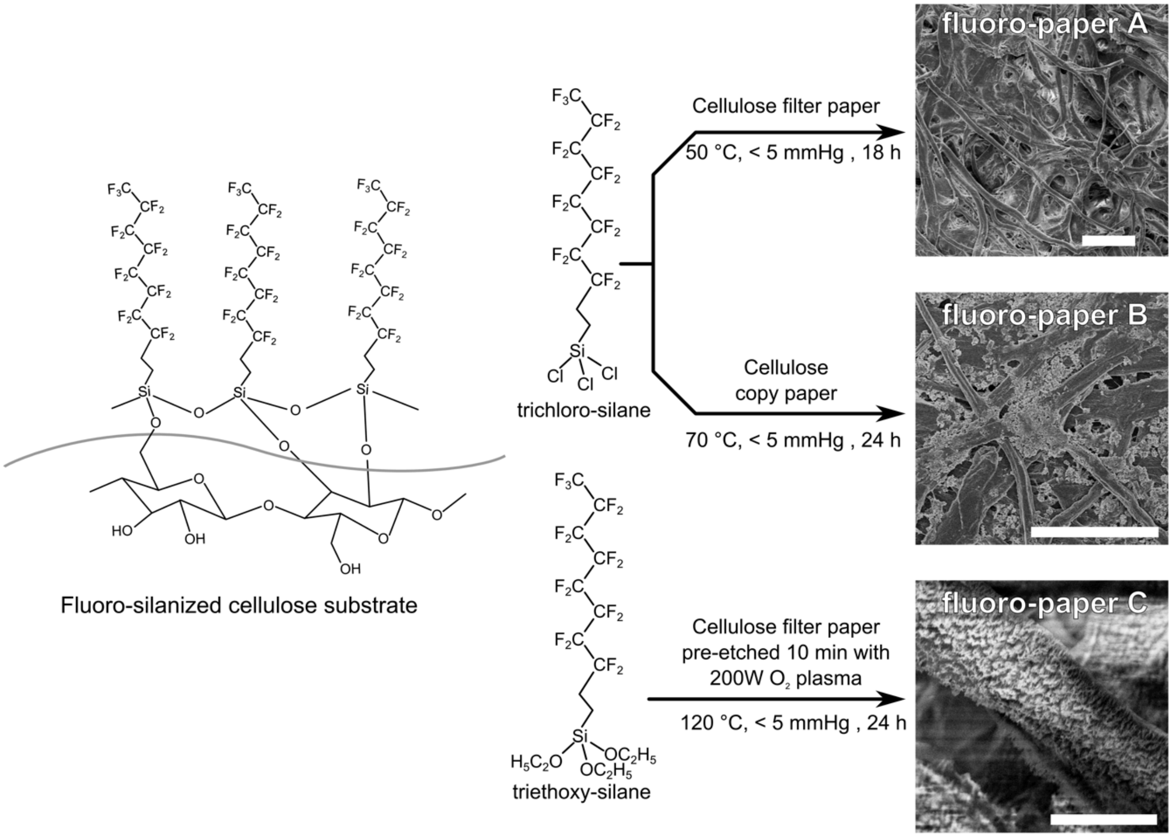
fluoro-paper A
Cellulose filter paper
50 °C, < 5 mmHg , 18 h
fluoro-paper B
Cellulose
copy paper
70 °C, < 5 mmHg , 24 h
trichloro-silane
Fluoro-silanized cellulose substrate
fluoro-paper C
Cellulose filter paper
pre-etched 10 min with
200W O2 plasma
120 °C, < 5 mmHg , 24 h
triethoxy-silane

**Figure 2.2.** Fluoro-silanization of different cellulose papers by vapor phase deposition. Typical SEM images of cellulose filter paper (A), cellulose copy paper (B) and cellulose filter paper pretreated by $O_2$ plasma etching (Plasmatherm 790, 200 W, 10 min) (C). Scale bars on SEMs of Type A, B, and C are 100, 100, and 10 mm respectively.

The apparent advancing contact angle ($\theta^*_{adv}$) of water on fluoro-paper A was > 160°, and the robustness parameters $A^*_{water}$ = 24.6 and $A^*_{hexadecane}$ = 4.5, indicated that both water and hexadecane were in a stable, non-wetted, Cassie-Baxter state (see Methods for details). In addition, even very low surface tension liquids, including hexane (non-polar, 18.4 mN/m, $\theta^*_{adv}$ = 91°), and ethanol (polar, 22.3 mN/m, $\theta^*_{adv}$ = 112°) did not wet this surface (Table 2.2).

**Table 2.2.** $\theta^*_{adv}$, $\theta^*_{rec}$ and contact angle hysteresis ($\Delta\theta$) values for various liquids on fluoro-paper A.

| **Solvent** | $\gamma_{lv}$ [mN/m at 20 °C] | $\theta^*_{adv}$ [°] | $\theta^*_{rec}$ [°] | $\Delta\theta$ [°] |
|---|---|---|---|---|
| Water | 72.7 | 161 | 143 | 19 |
| Propylene Glycol | 45.6 | 150 | 122 | 28 |
| N,N-Dimethylformamide | 34.4 | 143 | 100 | 43 |
| o-Xylene | 29.6 | 138 | 97 | 40 |
| Hexadecane | 27.1 | 136 | 103 | 33 |
| Chloroform | 26.7 | 126 | 90 | 36 |
| Tetrahydrofuran | 26.7 | 125 | 90 | 36 |
| Acetone | 23 | 121 | 84 | 37 |
| Methanol | 22.1 | 114 | 60 | 54 |
| Ethanol | 22 | 112 | 59 | 53 |
| 1-Propanol | 20.9 | 113 | 60 | 52 |
| Hexane | 17.9 | 91 | 35 | 57 |

This omniphobic fluoro-paper A was subsequently treated with $O_2$ plasma (200 W unless stated otherwise; Methods) for different times to obtain surfaces that were selectively wet by different liquids depending on their surface tension and polarity. Typically, $O_2$ plasma treatment increases the surface energy of a polymer surface through oxidation.[50] As a consequence, the wettability of a surface generally increases with $O_2$ plasma exposure time, with the lower surface tension liquids wetting the surface first. This trend was observed at relatively short exposure times < 60 sec (Figure 2.1b; Figure 2.3).

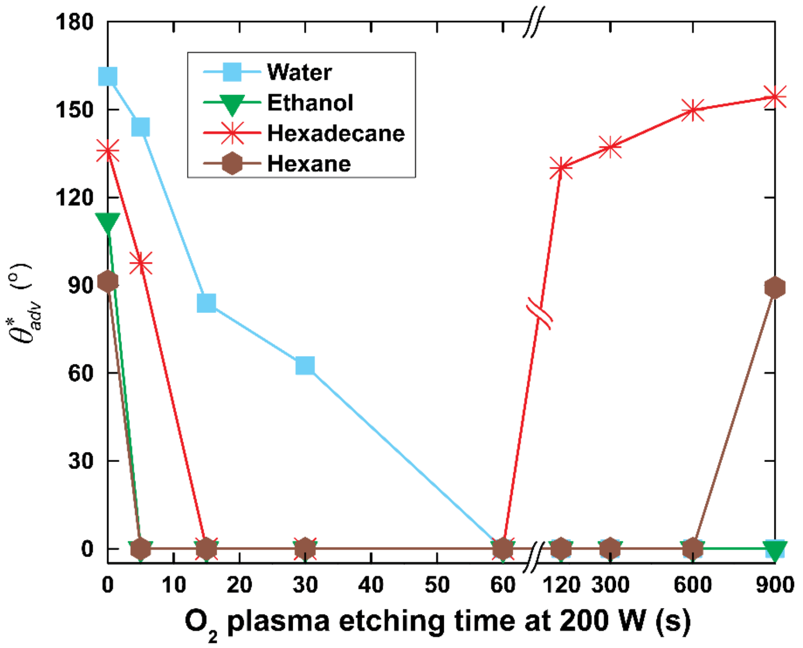

**Figure 2.3.** $\theta^*_{adv}$ values for various liquids on fluoro-paper A treated by $O_2$ plasma etching for varying times (0–900 sec).

For example, a 15 sec application of $O_2$ plasma transformed the originally omniphobic fluoro-paper A into a HP/OL surface ($A^*_{water} = 4.4$, $A^*_{hexadecane} < 1$). Low surface tension liquids like alkanes and ethanol wetted the surface, while high surface tension liquids like water remained non-wetting. A further increase in $O_2$ plasma etching time to 60 sec yielded an omniphilic surface, on which even a high surface tension liquid like water completely wets ($A^*_{water}$ and $A^*_{hexadecane} < 1$) (Figure 2.1b).

This initial enhancement in surface wettability is mainly due to the simultaneous defluorination and oxidation of the fluoro-paper A surface. This is evident from X-ray photoelectron spectroscopy (XPS) analysis of the surface chemistry (Figure 2.4e,f).

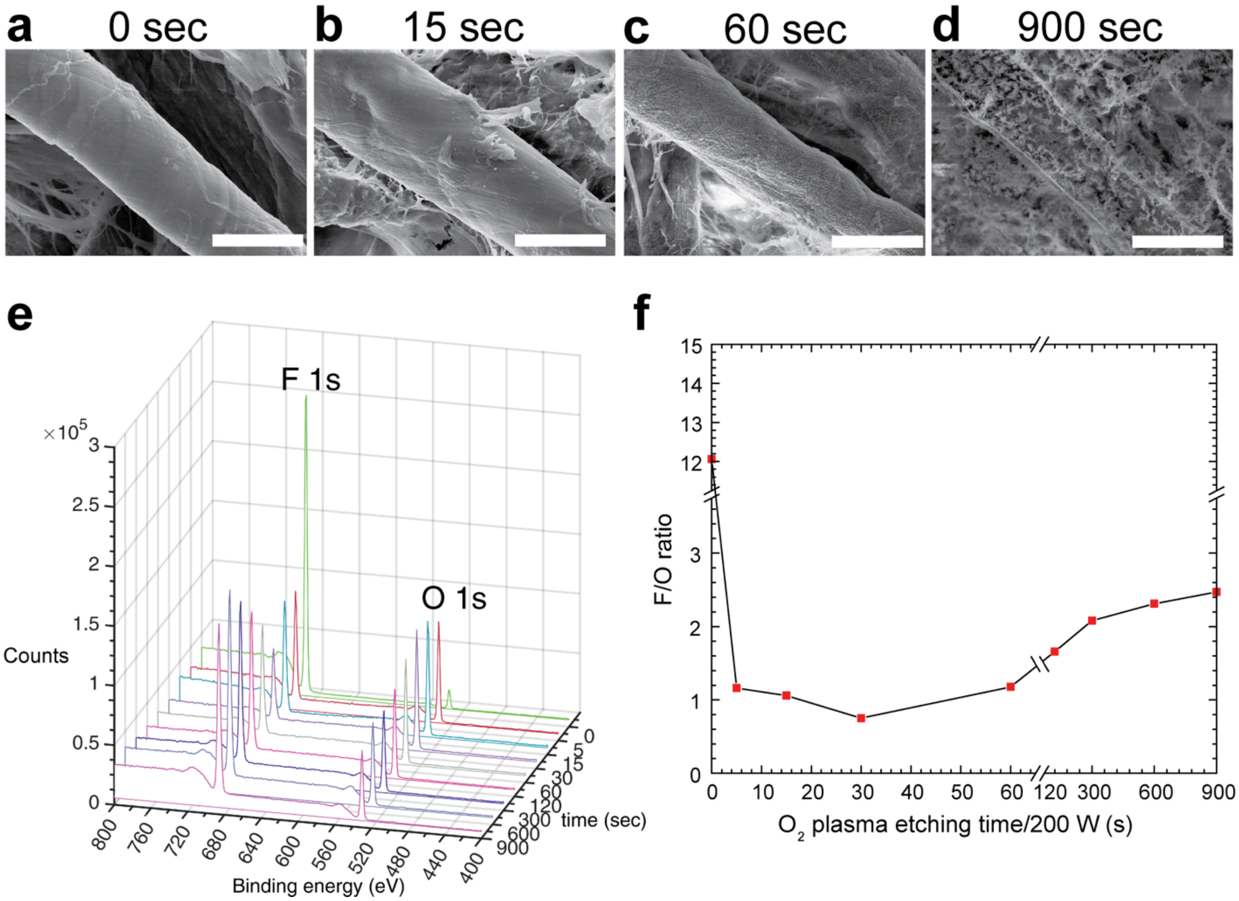

**Figure 2.4.** (a-d) SEM images and XPS peak data for fluoro-paper A treated by $O_2$ plasma etching for different times (0–900 sec) showing the dramatic change in the fiber surface texture. All scalebars are 10 μm. (e) XPS spectra at various etching times, with the fluorine 1s and oxygen 1s peaks highlighted. Note the rapid initial decrease in fluorine content and increase in oxygen content as the fluorosilane is replaced by oxygen-rich species from the reactive oxygen plasma. At extended etching times, the redeposition of fluorocarbon fragments on the $O_2$ plasma-etched surface is visible as an increase in the fluorine 1s peak and a decrease in the oxygen 1s peak. The ratio between the peak heights for fluorine and oxygen versus time are plotted in (f).

For example, after a short burst (5 sec) of $O_2$ plasma, a dramatic increase in the surface oxygen content can be observed. Increasing the $O_2$ plasma etching time to 30 sec yields the minimum value for the fluorine to oxygen (F/O) ratio. In addition to analyzing the changes in surface chemistry, scanning electron microscopy (SEM) was used to observe the development of fibrillar nanostructures along the cellulose microfibers (Figure 2.4a-d). This nano-texturing occurs due to the selective etching of amorphous components within the cellulose fibers.[51] After 60 sec of etching, the increased solid surface energy, and increased surface roughness, transform the originally omniphobic fluoro-paper A surface into an omniphilic material.

Counter-intuitively, exposure to $O_2$ plasma for an even longer time yields the HL/OP extreme wettability (Figure 2.1b; Figure 2.3). When the $O_2$ plasma etching time was > 300 sec, the surface became non-wettable by hexadecane, and when it was > 900 sec, the surface became non-wettable even by hexane ($A^*_{water} < 1$, $A^*_{hexadecane} = 17.3$). Note that the $A^*$ value for hexadecane on fluoro-paper A after 900 sec of etching is even greater than that on the original omniphobic surface. It was found that after the F/O ratio reaches its minimum value at around 30 sec of etching, the ratio begins to increase again (Figure 2.4e,f). This fluorine recovery may be attributed to the redeposition of fluorocarbon fragments present in the vacuum chamber after the fluorosilane is removed during the initial stages.[52] Simultaneously, the extended etching also causes the surface of the cellulose microfibers to be significantly roughened due to the development of fibrillar nanostructures (Figure 2.4d). Through a synergistic effect from both enhanced roughness and recovered fluorine content, the surfaces eventually resist wetting by low surface tension alkanes (*e.g.* $\theta^*_{adv}$ for hexadecane is 154° on fluoro-paper A etched for 900 sec).

Surfaces that repel low surface tension liquids almost always repel water as well, due to its higher surface tension. However, the partially fluorinated, extremely rough surface produced by extended etching yields a reconfigurable or “hygro-responsive” surface, similar to those we have reported previously.[17] When a polar liquid like water contacts this HL/OP surface, the surface reconfigures to enable the polar hydroxyl groups along the cellulose fibers to hydrogen bond with the water molecules. This interaction/surface reconfiguration does not occur with non-polar liquids, and the result is a surface that can be wet by water, but not by non-polar liquids like hexane. Overall, by simply changing the time a fluoro-paper A surface is exposed to $O_2$ plasma, we can create surfaces with all four extreme wettabilities (Figure 2.1b). Further, in our testing, the different surfaces maintained their extreme wettabilities for several days following fabrication.

### *2.3.2 Generation of 2D and 3D Fluidic Channels on Fluoro-Paper A*

Two-dimensional microfluidic channels with defined dimensions and wettabilities were initially fabricated by selectively covering fluoro-paper A substrates with polyimide tape prior to $O_2$ plasma etching (Figure 2.5; Methods).

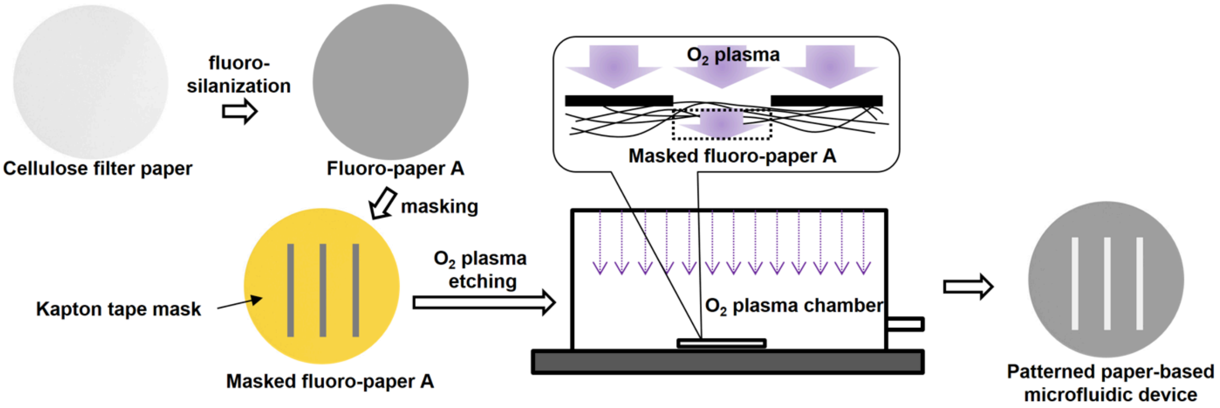
fluoro-
silanization
Cellulose filter paper
Fluoro-paper A
masking
$O_2$ plasma
Masked fluoro-paper A
Kapton tape mask
$O_2$ plasma
etching
$O_2$ plasma chamber
Masked fluoro-paper A
Patterned paper-based
microfluidic device

**Figure 2.5.** Schematic illustration of the procedure to make a wettability-patterned paper device by selective $O_2$ plasma etching of fluoro-paper A.

Seven different polar and nonpolar liquids (surface tensions from $\gamma_{lv}$ = 18.4–72.8 mN/m) were placed into channels exposed for 5–900 sec (Figure 2.6a), and their maximum wetting length (Table 2.3), average wetting velocity (total wetting length over total time[53]) (Table 2.4), and wetting depth (Table 2.5) were measured.

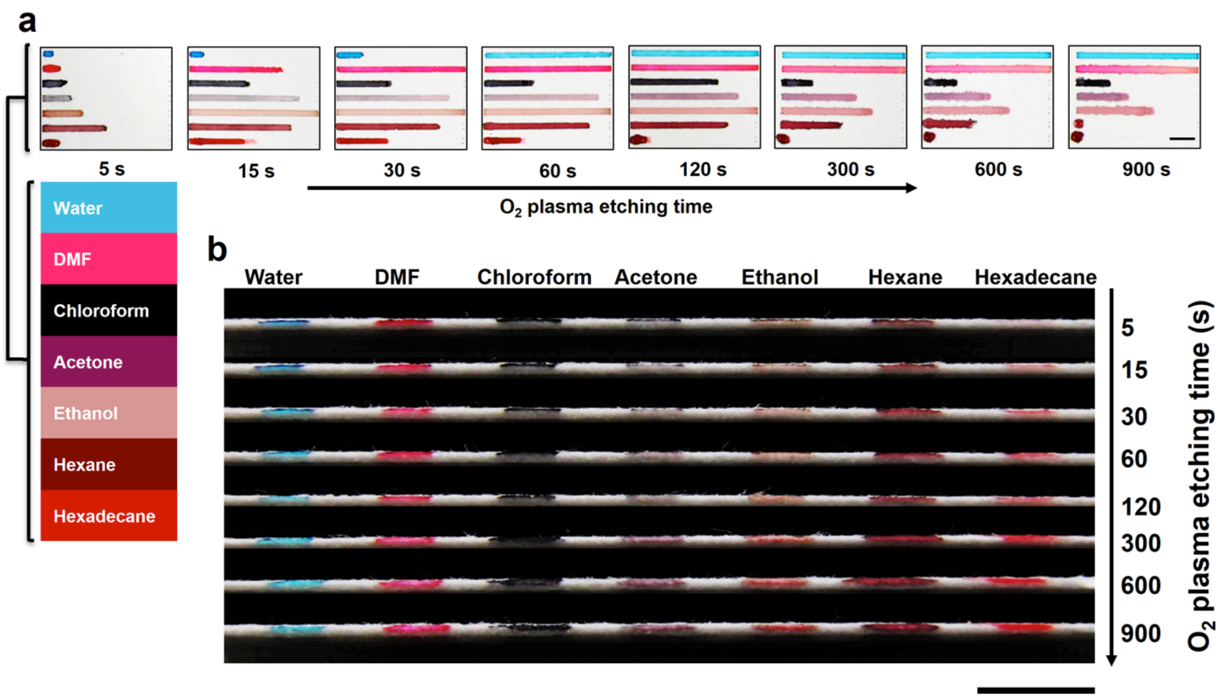
a
5 s
15 s
30 s
60 s
120 s
300 s
600 s
900 s
$O_2$ plasma etching time
Water
DMF
Chloroform
Acetone
Ethanol
Hexane
Hexadecane
b
Water
DMF
Chloroform
Acetone
Ethanol
Hexane
Hexadecane
5
15
30
60
120
300
600
900
$O_2$ plasma etching time (s)

**Figure 2.6.** Lateral flow in two-dimensional channels treated by 200 W $O_2$ plasma etching for varying times on fluoro-paper A. (a) Fluoro-paper A devices with straight 50 mm × 2 mm channels that were treated by $O_2$ plasma with etching times between 5 and 900 sec. For different paper devices exposed for each time (increasing from top to bottom), water (blue), DMF (pink), chloroform (black), acetone (light purple), ethanol (light pink), hexane (maroon), and hexadecane (dark red) were tested. The paper substrates were positioned horizontally and each channel was filled with 20 µL of test liquid. Scale bar is 1 cm. (b) Optical image of the cross-section of two-dimensional channels etched for various times filled with seven test liquids. The paper thickness is 390 µm, scale bar is 5 mm.

**Table 2.3.** Maximum wetting length, *i.e.* the maximum horizontal distance that the liquid front covers, for 20 µL of test liquid placed into channels on fluoro-paper A. The liquid channels are 50 mm in length.

| **$O_2$ plasma etching time at 200 W [sec]** | **Maximum wetting length [mm]** | | | | | | |
|---|---|---|---|---|---|---|---|
| | **Water** | **DMF** | **Chloroform** | **Acetone** | **Ethanol** | **Hexane** | **Hexadecane** |
| **5** | 4.0 | 7.2 | 9.6 | 11.6 | 16.0 | 25.0 | 6.9 |
| **15** | 5.8 | 36.4 | 23.5 | 42.7 | 50 | 39.5 | 33.5 |
| **30** | 10.7 | 50 | 21.5 | 43.7 | 50 | 40.5 | 23.6 |
| **60** | 50 | 50 | 20.0 | 45.5 | 50 | 42.6 | 24.6 |
| **120** | 50 | 50 | 34.5 | 42.5 | 50 | 38.6 | 21.4 |
| **300** | 50 | 50 | 13.0 | 30.9 | 37.6 | 25.5 | 3.8 |
| **600** | 50 | 50 | 13.6 | 27.0 | 35.2 | 22.1 | 3.8 |
| **900** | 50 | 50 | 14.2 | 21.4 | 31.8 | 3.8 | 3.8 |

**Table 2.4.** Average wetting velocity, *i.e.* maximum wetting length divided by the total wetting time.

| $O_2$ plasma etching time at 200 W [sec] | Average wetting velocity [mm/s] | | | | | | |
|---|---|---|---|---|---|---|---|
| | Water | DMF | Chloroform | Acetone | Ethanol | Hexane | Hexadecane |
| **5** | 0 | 0 | 0 | 0.50 | 0.43 | 1.04 | 0 |
| **15** | 0 | 0.14 | 0.56 | 2.03 | 2.27 | 1.88 | 0.08 |
| **30** | 0.47 | 1.35 | 0.50 | 2.43 | 2.63 | 2.25 | 0.06 |
| **60** | 0.16 | 1.67 | 0.21 | 2.28 | 1.85 | 2.84 | 0.05 |
| **120** | 0.81 | 1.00 | 0.82 | 2.66 | 1.39 | 2.27 | 0.01 |
| **300** | 0.25 | 0.61 | 0.14 | 1.82 | 0.63 | 1.70 | 0 |
| **600** | 0.15 | 0.16 | 0.10 | 0.73 | 0.35 | 0.88 | 0 |
| **900** | 0.15 | 0.10 | 0.12 | 0.40 | 0.25 | 0 | 0 |

**Table 2.5.** Wetting depth, *i.e.* the vertical distance that the test liquid wets within the channel. The thickness of paper is 390 μm.

| $O_2$ plasma etching time at 200 W [sec] | Wetting depth [μm] | | | | | | |
|---|---|---|---|---|---|---|---|
| | Water | DMF | Chloroform | Acetone | Ethanol | Hexane | Hexadecane |
| **5** | 52 | 75 | 94 | 66 | 56 | 94 | 28 |
| **15** | 65 | 94 | 103 | 81 | 85 | 108 | 66 |
| **30** | 93 | 101 | 92 | 69 | 70 | 149 | 58 |
| **60** | 85 | 160 | 89 | 240 | 273 | 211 | 94 |
| **120** | 116 | 202 | 99 | 273 | 287 | 226 | 99 |
| **300** | 160 | 273 | 197 | 282 | 301 | 230 | 216 |
| **600** | 183 | 291 | 240 | 318 | 321 | 291 | 150 |
| **900** | 211 | 305 | 245 | 339 | 341 | 310 | 211 |

Both the maximum wetting length and the peak average wetting velocity for each liquid occurred at different plasma etching times. This is consistent with the selective variation in wettability with etching time as shown in Figure 2.1b. Additionally, only the upper surface of the etched paper sample became more wettable, as directional $O_2$ etching did not penetrate deep into the paper. This enables the confinement of liquid to a limited depth, reduces liquid retention within the channels, limits unproductive sample consumption, and also permits the fabrication of multi-layer flow devices on a single paper substrate, as discussed below.

Next, we fabricated three-dimensional flow channels on a single piece of fluoro-paper A that were capable of confining liquids with a wide range of surface tensions and polarities (Methods). As shown in Figure 2.7a, eight fluidic channels were arranged orthogonally on a device, with four channels each along the *x*- and *y*-directions.

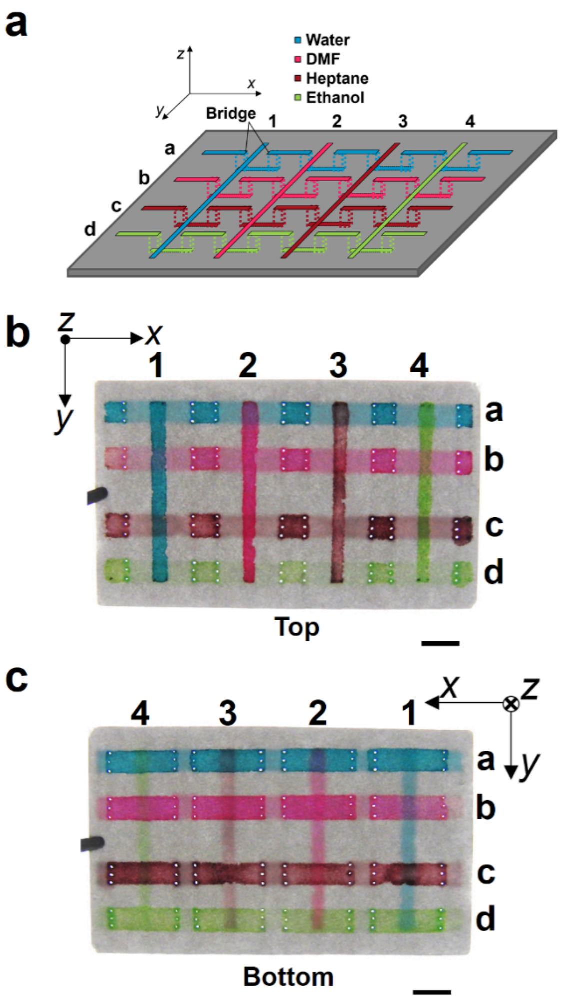

**Figure 2.7.** Three-dimensional paper device. (a) A schematic illustrating the three-dimensional patterning of fluidic channels on a single piece of paper, by incorporating channels on both sides of a fluoro-paper A substrate. Two groups of channels are patterned orthogonally in the *x*- and *y*-directions. These are labeled as a, b, c, d and 1, 2, 3, 4, respectively. (b and c) The top and bottom of a three-dimensional paper device after being filled with four test liquids: water (blue), DMF (red), heptane (brown) and ethanol (green). Scale bars are 5 mm.

To traverse from one edge of the device to the other, liquids filling the channels along the *x*-direction must bridge straight channels in the *y*-direction by flowing to the bottom surface of the paper. This is accomplished by passing the liquid through short bridge channels on the bottom surface using arrays of vertical perforations (500 μm diameter) penetrating the entire thickness of the paper at the junctions, then returning it to the top surface via more perforations (Figure 2.8).

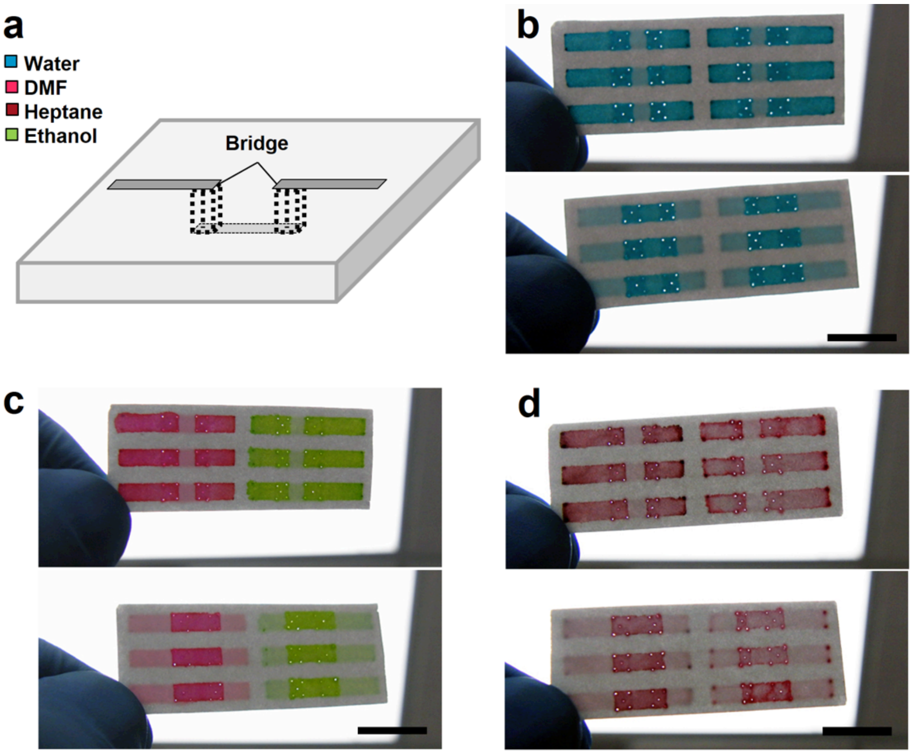

**Figure 2.8.** (a) Schematic illustration of three-dimensional channels each with a single bridge (fluoro-paper A). The channels are 18 mm long × 2 mm wide. Each bridge was 7.5 mm long and contained an array of five 500 μm diameter perforations on either side. (b) Three-dimensional channels filled with water (dyed blue). (c) Three-dimensional channels filled with DMF (dyed pink) and ethanol (dyed green). (d) Three-dimensional channels filled with heptane (dyed maroon). Scale bars are 1 cm.

The channels were selectively $O_2$ plasma etched for different times at 350 W to obtain maximum flow rates for each of the four liquids used (Methods). Approximately 20 μL droplets of water, dimethylformamide (DMF), ethanol and heptane were loaded at the ends of the channels. Complete filling of the 4 × 4 bridge device was observed for water and DMF, but ethanol and heptane had to be filled from both ends to counteract their higher evaporation rates. No mixing between test liquids in the separate *x*- or *y*-direction channels was observed at any point (Figure 2.7b,c). Overall, these three-dimensional channels can increase the available interfacial area for the patterning of channels, facilitate routing of channels in complex devices, and enable the incorporation of different assays on different sides of paper-based microfluidic devices.[35-40]

### *2.3.3 Printing of Fluidic Channels on Fluoro-Paper B*

To increase the ease of use, and reduce the time required for the patterning process, we also developed a mask-free, direct printing technique to produce fluidic channels of arbitrary geometry, capable of containing very low surface tension liquids (Figure 2.9a; Methods). To enable such direct printing of fluidic channels, we first developed a second type of fluorinated-paper, fluoro-paper B, which exhibits high advancing contact angles, but zero receding contact angles with both water and oil (Table 2.1; Figure 2.2). While the hysteresis on this surface was significantly higher than on the fluoro-paper A surface, the $A^*$ values remain >> 1, indicating that the paper still strongly resists wetting by all liquids ($A^*_{water} = 19.3$, $A^*_{hexadecane} = 3.1$). The zero receding contact angles, and very high advancing contact angles, enabled the facile deposition of defect-free films of a high surface energy polyurethane adhesive by preventing the dewetting and spreading of the adhesive. The films were deposited by directly applying a viscous solution of the polyurethane adhesive through a tapered deposition nozzle attached to an XYZ motorized stage (Methods). The minimum width of the printed lines, and the interstitial spacing between lines, were 700 μm and 400 μm respectively. A line drawing of the Lurie Bell Tower at the

University of Michigan (5.3 × 4.4 cm) was successfully printed on fluoro-paper B and filled with a low viscosity (5 cSt) silicone oil ($\gamma_{lv}$ = 19.8 mN/m) (Figure 2.9b-e).

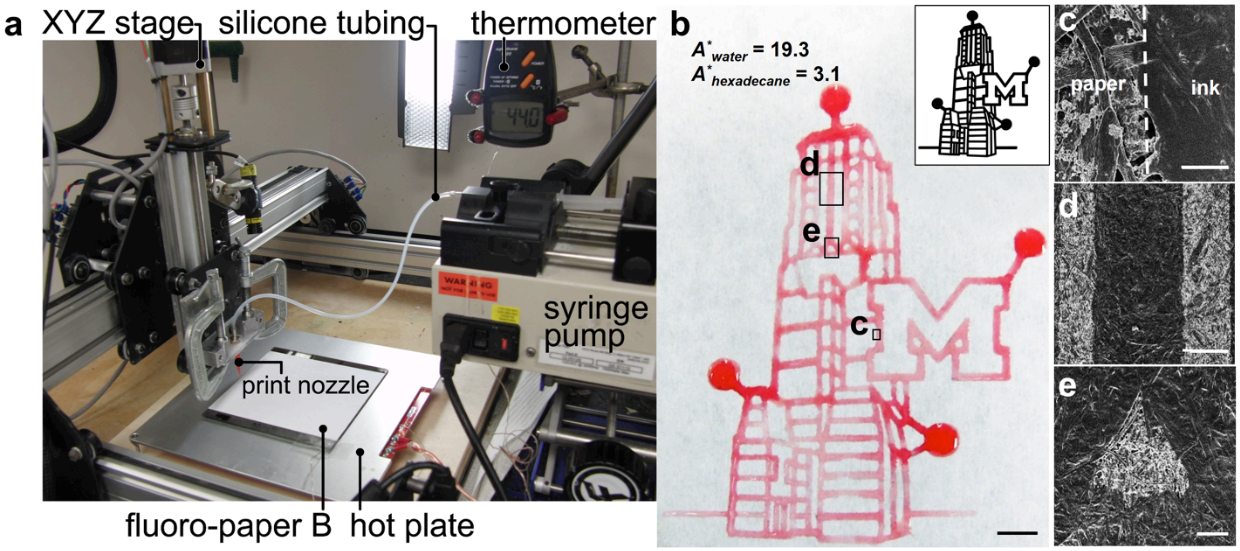

**Figure 2.9.** Mask-free, direct printing of fluidic channels on omniphobic paper. (a) The printing apparatus. (b) A printed pattern on a fluoro-paper B surface. The channels have been filled with silicone oil ($\gamma_{lv}$ = 19.8 mN/m), dyed red. The inset is the 5.3 × 4.4 cm pattern being printed. Scale bar is 5 mm. (c-e) SEM images highlighting the magnified texture for different areas on the patterned surface shown in (b) after the channel is filled with silicone oil. The corresponding areas are labeled as c, d, and e in (a). Scale bars are 50 μm for (c), 500 μm for (d), and 200 μm for (e).

### *2.3.4 Continuous Oil-Water Separation on Fluoro-Paper A*

Next, we focused on multiple novel applications of paper-based microfluidic devices that necessitate the utilization of surfaces with extreme wettabilities, which would not have been possible with simple omniphilic channels patterned on an omniphobic background. These applications, including liquid-liquid extraction, and droplet generation by flow focusing, require the selective confinement of oil and water phases and the maintenance of a stable organic-aqueous liquid-liquid interface. To verify this selectivity in wettability, and the stability of the oil-water interface, we first fabricated an oil-water separation device consisting of a HP/OL channel placed head-to-head against a HL/OP channel on fluoro-paper A (Figure 2.10a; Figure 2.11).

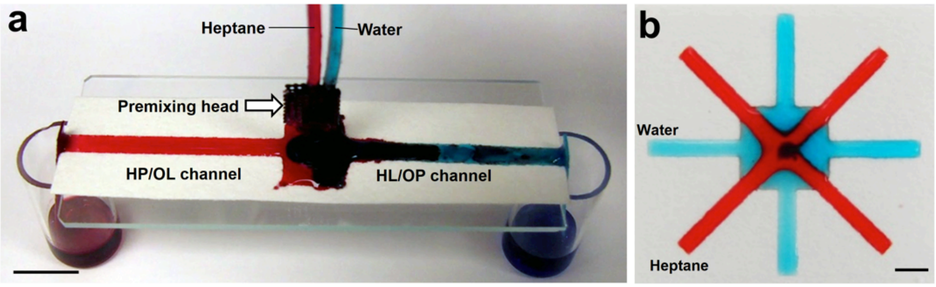

**Figure 2.10.** (a) Continuous oil-water separation device. A HP/OL channel is combined with a HL/OP channel on a fluoro-paper A surface and used to separate a mixture (50% by volume) of heptane and water. Scale bar is 1 cm. (b) Multiplexed oil-water dispenser, composed of four HL/OP and four HP/OL channels radially arranged from a central reservoir. Any oil or water droplets when added to this reservoir are automatically split and dispensed into four HP/OL or HL/OP channels, respectively. Scale bar is 5 mm.

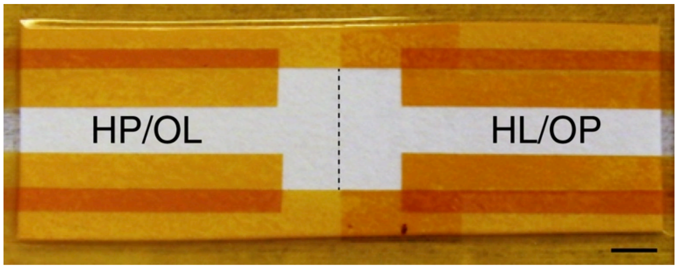

**Figure 2.11.** Geometry of the device for continuous surface oil-water separation (fluoro-paper A). The HP/OL channel was $O_2$ plasma etched at 200 W for 15 sec, while the HL/OP channel was etched for 900 sec. Scale bar is 5 mm.

Heptane was pre-mixed with water by pumping at 100 μL/min through a stainless steel mesh, and the mixture was continuously added onto the central reservoir containing the interface between the HP/OL and HL/OP channels. The heptane-water mixture spontaneously separated as the heptane selectively wet the HP/OL channel, while the water selectively wet the HL/OP channel. Pure heptane (> 99.9%) and water (> 99.9%) were collected at the opposite ends of the device. With this approach, continuous separation of an oil-water mixture could be realized on a paper substrate, based solely on the difference in wettabilities of the patterned channels. To demonstrate the scalability of this approach, we also fabricated a multiplexed oil-water dispenser with four outlets each for both oil and water (Figure 2.10b; Methods). Continuous separation and dispensing of a heptane-water mixture could be readily achieved with this device.

### *2.3.5 Continuous Liquid-Liquid Extraction on Fluoro-Paper A*

We also demonstrated continuous liquid-liquid extraction on a paper-based microfluidic device. Liquid-liquid extraction is a well-known unit operation in chemical engineering, used to extract one or more miscible components from a liquid mixture by exposing it to another liquid with preferential solubility for the target components. It is also widely utilized in analytical chemistry, biology, and the environmental sciences. It is particularly well suited for lab-on-a-chip based purification and analytical units.[54]

We fabricated a liquid-liquid extraction device consisting of a HP/OL channel that is placed alongside a HL/OP channel on fluoro-paper A (Figure 2.12a; Figure 2.13a). The feed was a mixture of octane and ethanol (dyed with methylene blue, which is preferentially soluble in ethanol), and the extractant was water. The flow rate of the feed and the extractant were both 50 μL/min to maintain a 1 : 1 volume ratio. The HL/OP channel was first filled with water. The water was completely confined in the channel and did not overflow into the background or the adjacent HP/OL channel. The octane-ethanol mixture was subsequently introduced into the HP/OL channel, yielding a well-defined and stable organic-aqueous liquid-liquid interface (Figure 2.12b). Ethanol was continuously extracted by the water stream, moving from the top channel to the bottom channel. The extractant (water) started out transparent in the inlet tube and at the beginning of the extraction zone, but became blue, due to the presence of the blue-dyed ethanol, by the time it reached the end of the HL/OP channel. In comparison, the feed (octane +

ethanol) started out blue in the extraction zone and became clear by the time it reached the end of the HP/OL channel, due to the near-complete removal of dyed ethanol. After the system reached steady state, the three zones (extraction, transition, and clear) in the HP/OL channel were clearly observed.

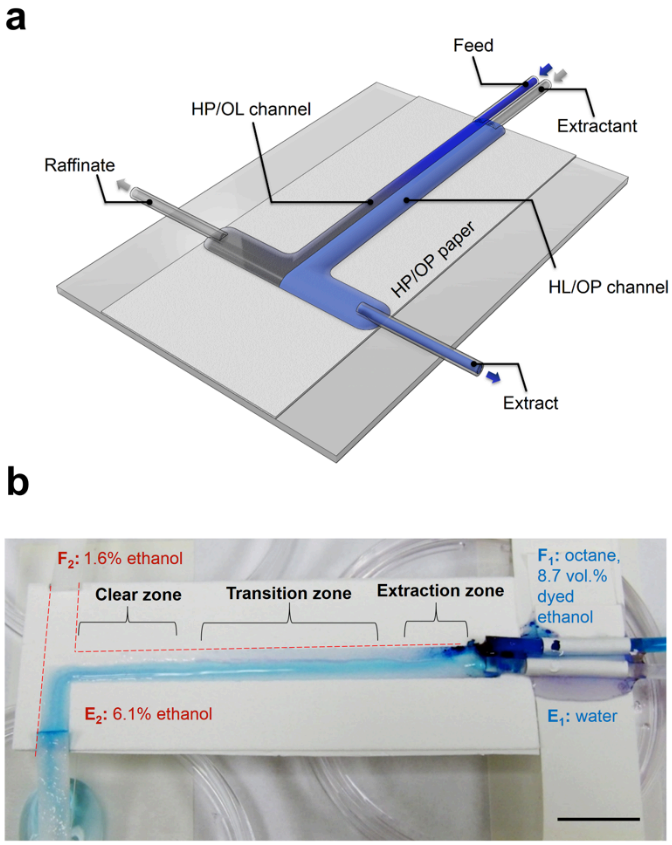
a
Feed
Extractant
HP/OL channel
Raffinate
HP/OP paper
HL/OP channel
Extract
b
$F_2$: 1.6% ethanol
Clear zone
Transition zone
Extraction zone
$F_1$: octane, 8.7 vol.% dyed ethanol
$E_2$: 6.1% ethanol
$E_1$: water

**Figure 2.12.** Surface liquid-liquid extraction. (a) A schematic highlighting the design of a device that enables continuous, co-current, liquid-liquid extraction on paper. (b) A HP/OL channel is combined with a HL/OP channel, side-by-side, on a fluoro-paper A surface and used for liquid-liquid extraction. The bottom channel is HL/OP. This channel is filled with water, which serves as the extractant. The top channel is HP/OL and is filled with a mixture of octane and ethanol. Scale bar is 1 cm.

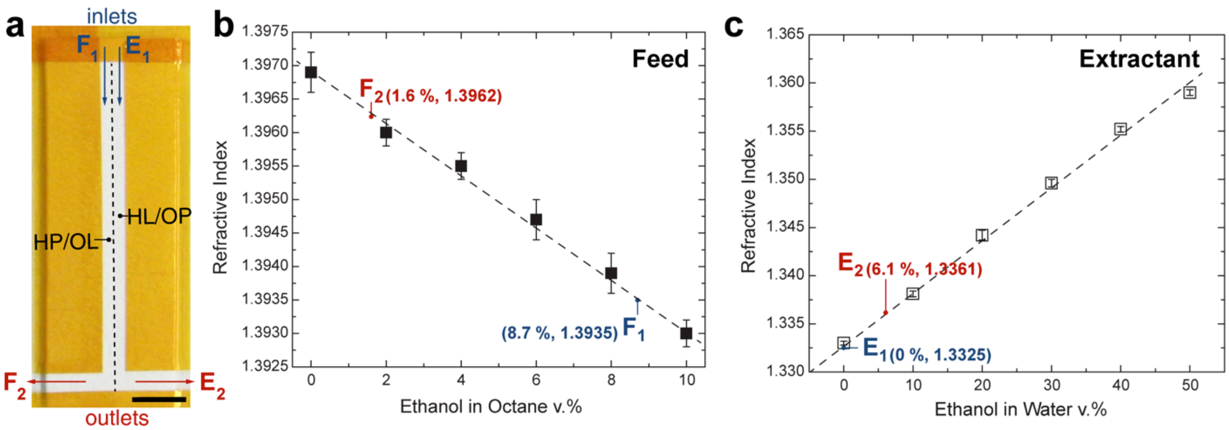

**Figure 2.13.** (a) Geometry of the device for continuous surface liquid-liquid extraction (fluoro-paper A). The HP/OL channel was etched at 200 W for 15 sec, and the HL/OP channel was etched for 900 sec. Scale bar is 1 cm. (b, c) Refractive index measurements of the feed and extractant before ($F_1$, $E_1$) and after extraction ($F_2$, $E_2$). A calibration curve for each mixture was first obtained by measuring mixtures of known composition (black data points), which was then used to quantify the composition of the test samples.

In this experiment, the majority of the ethanol (~82%) was removed from the feed. This was evaluated by performing refractive index measurements on the feed and the extractant before flowing through the device, as well as on the raffinate (feed minus extracted material) and the extract (extractant mixture with extracted material) produced downstream. The compositions were determined by comparing these refractive index values with calibration curves generated using mixtures of a known composition (Figure 2.13b,c). Note that in this case, the movement of ethanol from the organic (octane) phase to the aqueous phase occurred due to the imbalance in chemical potential of ethanol across the liquid-liquid interface. A control experiment was performed with the same geometry but with adjacent omniphilic channels (Figure 2.14). Without the selectivity in wettability between the organic and aqueous phases, the organic phase, due to its lower surface tension, will always undercut and displace the aqueous phase, causing the formation of an irregular organic-aqueous liquid-liquid interface. This prevented successful liquid-liquid extraction.

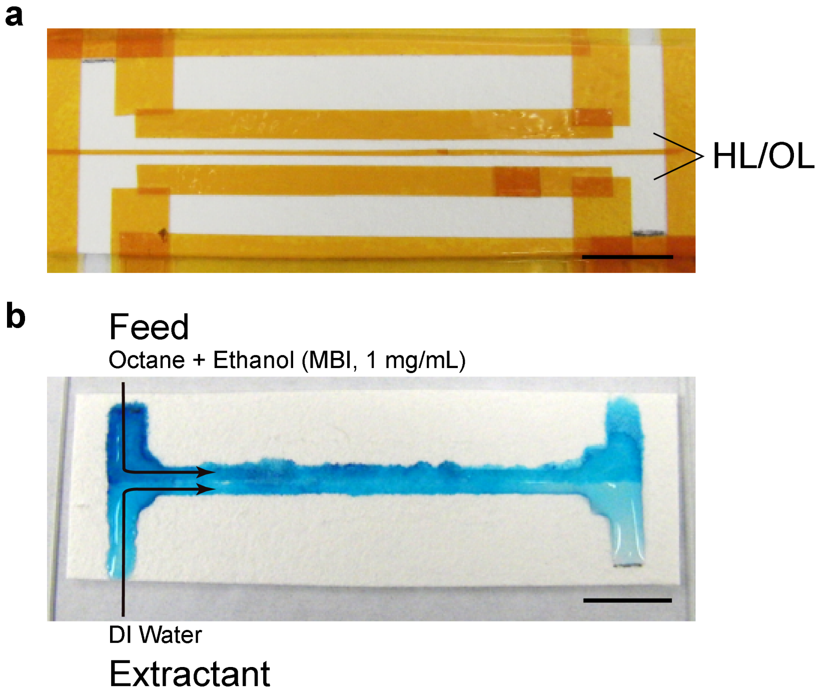

**Figure 2.14.** Control experiment for liquid-liquid extraction. (a) Geometry of side-by-side omniphilic channels patterned on fluoro-paper A, with 200 W $O_2$ plasma etching for 120 sec. (b) Failure to form a clear and stable oil-water interface between the feed and the extractant in the absence of channels possessing selective wettability. Scale bars are 1 cm.

### *2.3.6 Surface Emulsification for Particle Fabrication on Fluoro-Paper A*

Paper-based microfluidic devices reported in the literature are mainly designed and used for analysis and/or detection, rather than fabrication or synthesis.[40] We now discuss the development of an open-channel paper-based microfluidic device to fabricate polymeric microparticles. The fabricated device performs droplet emulsification using a “flow-focusing” geometry, previously only possible with traditional closed-channel devices.[55, 56]

Emulsification in a microfluidic device is performed to produce discrete droplets of a target substance with highly controlled, uniform dimensions at high production rates. Among the numerous applications of this technique are the production of polymeric micro- and nanoparticles, parallel experimentation with reactions occurring in droplets, which may be individually controlled, and encapsulation of single cells for analysis.[57, 58] Droplet microfluidics can also lower the overall volume required for effective sample transport through a device and prevent waste due to wetting of the microfluidic substrate, as a scarce or expensive target fluid may be suspended in an inexpensive, abundant carrier fluid.[59] Microfluidic emulsification performed in an open channel may also be preferable for a number of reasons. It is simpler to add samples and re-agents to specific locations on an open-channel device, the devices are less prone to clogging, and they have a large liquid-vapor interfacial area. Open channels also have a reduced hydraulic resistance, so less applied pressure is required for flow. This in turn leads to less applied shear stress on potentially sensitive samples such as encapsulated cells.[60-62]

The functionality of our open-channel emulsification device again relies on the selective wetting of adjacent HP/OL and HL/OP channels, and their ability to stabilize an organic-aqueous, liquid-liquid interface (Figure 2.15a; Figure 2.16; Methods). An aqueous surfactant solution was introduced within the HL/OP outer channel. The HP/OL inner channel was then filled with a UV cross-linkable precursor, immiscible with water. Both the aqueous and organic phases remained within their respective channels as they were pumped through the device, which was crucial in achieving stable emulsification (droplets of the organic phase suspended within the continuous aqueous phase) using the flow-focusing geometry (Figure 2.15b). Over a thousand micro-particles could be collected within one hour from a single surface emulsification device (Figure 2.15c). After crosslinking by passing under a UV lamp, the prepared polymeric microparticles were collected and found to be hemispheres (~500 μm base diameter) (Figure 2.15d). This geometry is attributed to the fact that the precursor droplets (organic phase) float on top of the aqueous phase in the open channel. Multiple parallel devices could easily be fabricated on the paper surface to increase the production rate.

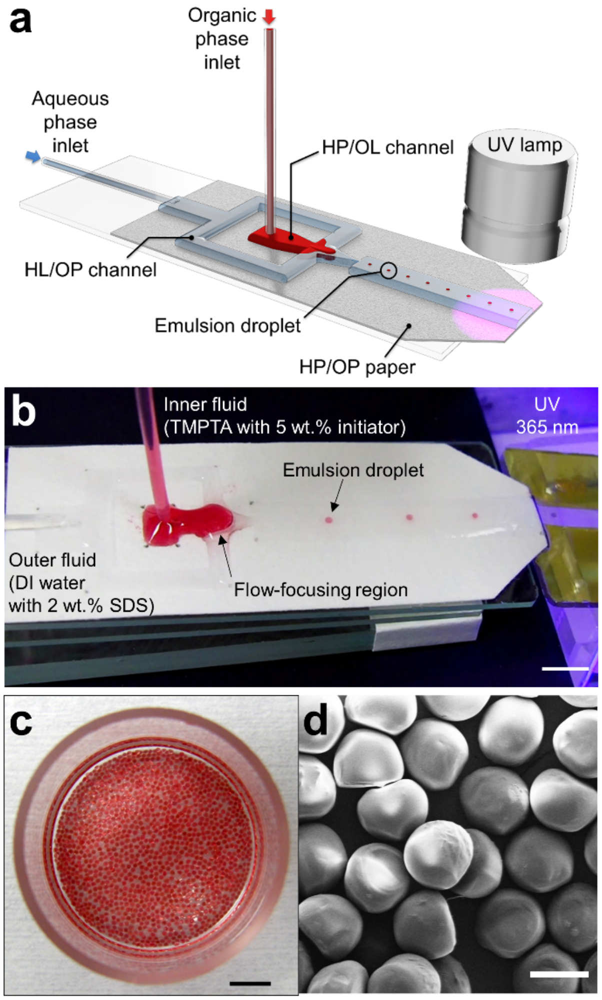
a
Organic phase inlet
Aqueous phase inlet
HP/OL channel
UV lamp
HL/OP channel
Emulsion droplet
HP/OP paper
b
Inner fluid (TMPTA with 5 wt.% initiator)
UV 365 nm
Emulsion droplet
Outer fluid (DI water with 2 wt.% SDS)
Flow-focusing region
c
d

**Figure 2.15.** Paper-based device for microparticle fabrication. (a) A schematic highlighting the design of a flow-focusing geometry for microfluidic emulsification and micro-particle fabrication on paper. (b) The micro-particle fabrication device on a fluoro-paper A surface illustrated in (a). Scale bar is 5 mm. (c) A photograph of the cross-linked micro-particles collected after 1 hour of operation (particles are dyed red and collected in a glass vial). Scale bar is 5 mm. (d) An SEM image of the UV cross-linked micro-particles. Scale bar is 500 μm.

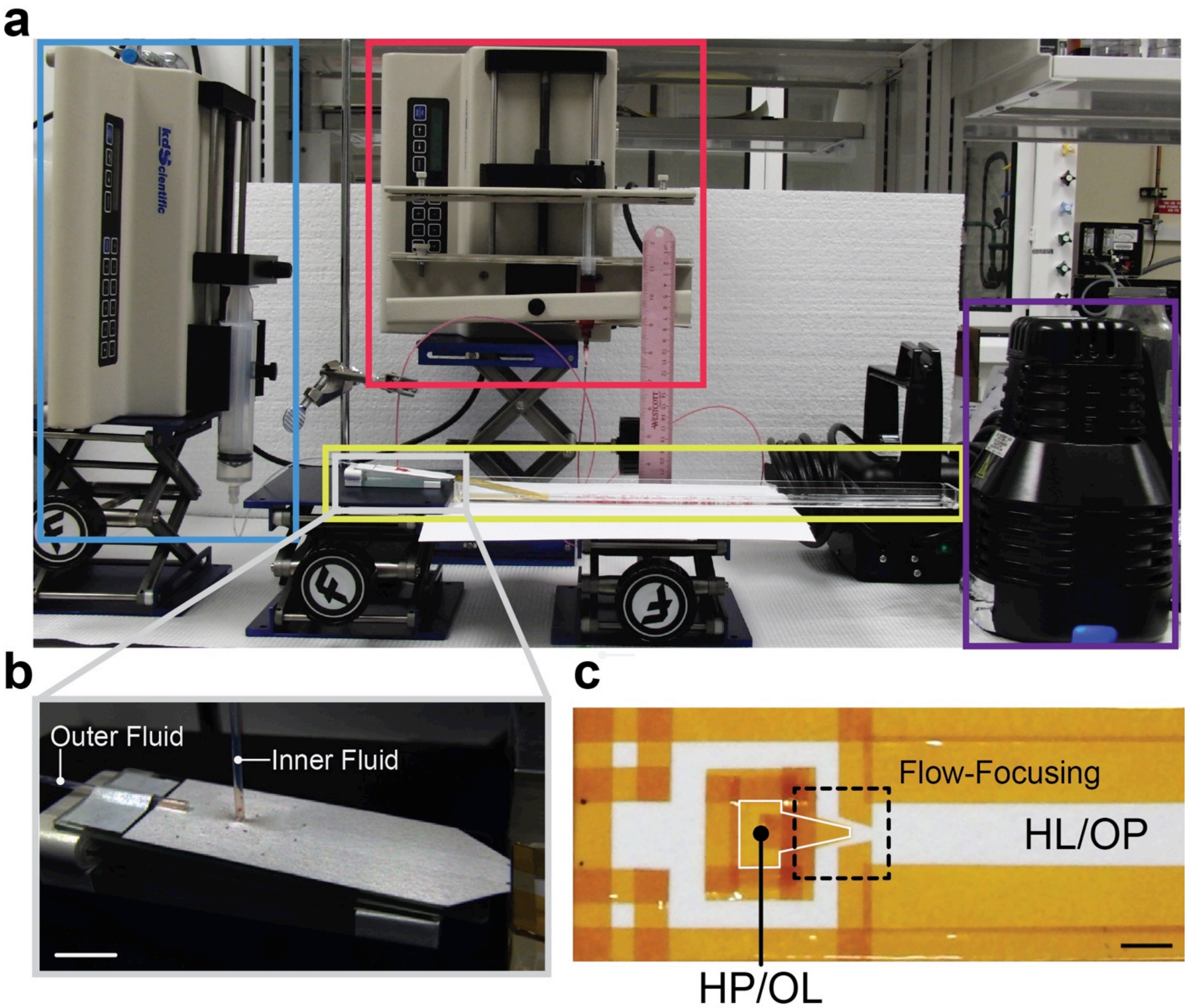

**Figure 2.16.** (a) Surface emulsification apparatus. The syringe pump highlighted in blue is used to control the flow rate of the outer carrier fluid. The other pump, highlighted in red, controls the inner precursor fluid. The area highlighted in yellow includes the paper-based microfluidic device and a glass trough for particle collection. The UV lamp used for crosslinking is highlighted in purple, and would be located above the trough during operation. (b, c) The flow focusing geometry patterned on fluoro-paper A. Scale bar is 1 cm for (b) and 5 mm for (c).

### *2.3.7 Surface Tension/Composition Measurement Using Fluoro-Paper A*

The developed microfluidic devices can also be useful for the facile determination of a binary mixture's composition. As an example, we have developed a so-called "alcohol-meter", that can readily determine the volume composition of an unknown ethanol-water mixture. Ethanol-water mixtures of varying composition were placed within a set of parallel HP/OL channels on fluoro-paper A (Figure 2.17).

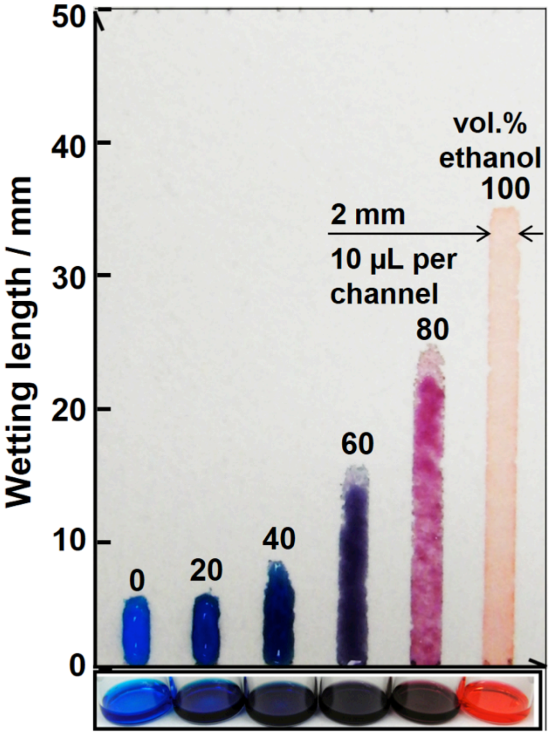

**Figure 2.17.** Measurement of the surface tension/composition of mixtures. A paper-based alcoholmeter developed on a fluoro-paper A surface. The alcoholmeter consists of patterned HP/OL channels on an omniphobic background.

The wetting length in these channels increases with decreasing liquid surface tension, *i.e.* the wetting length increased with increasing ethanol concentration.[63] By measuring the maximum liquid wetting length for any unknown ethanol-water mixture, it is easy to determine its surface tension, and therefore its composition, by comparing to wetting lengths of mixtures with known compositions. The developed device could similarly be calibrated for use with a range of different binary mixtures.

### *2.3.8 Ovarian Cancer Cell Microarrays on Fluoro-Paper C*

Finally, we investigated biological applications of the developed paper-based microfluidic devices. In particular, we developed a paper-based device that could be used for generating patterned arrays of mammalian cells. Patterned cell arrays can be used for the inexpensive, high-throughput, testing of different bioactive substances such as drugs, oligonucleotides, and peptides.[62] For this application, in order to limit cell adhesion to the background, we developed a third type of fluorinated paper, fluoro-paper C. It exhibits higher contact angles and lower contact angle hysteresis with both water and hexadecane than fluoro-paper A, as well as, higher $A^*$ values ($A^*_{water} > 45.0$, $A^*_{hexadecane} = 13.6$) (Table 2.1; Figure 2.2). This indicates that it has a significantly higher resistance to wetting. This was required to prevent the wetting of the omniphobic channels during the extended immersion under cell growth medium, required as part of the cell culture process. The fluoro-paper C fabrication involves the creation of a hierarchical texture of cellulose nanofibrils on filter paper with extended $O_2$ plasma etching prior to fluorosilanization (Methods). The fluoro-paper C was then patterned with omniphilic square spots and channels (~500 μm wide) by exposure to $O_2$ plasma through porous stainless steel masks (Figure 2.18).

These patterned omniphobic substrates with omniphilic domains were subsequently exposed to OVCAR3 cells (human ovarian adenocarcinoma cell line) in supplemented growth medium for 10 hours, and then stained with iodonitrotetrazolium chloride (Methods). The OVCAR3 cells selectively adhered to and grew on the omniphilic domains as opposed to the omniphobic background (Figure 2.19).

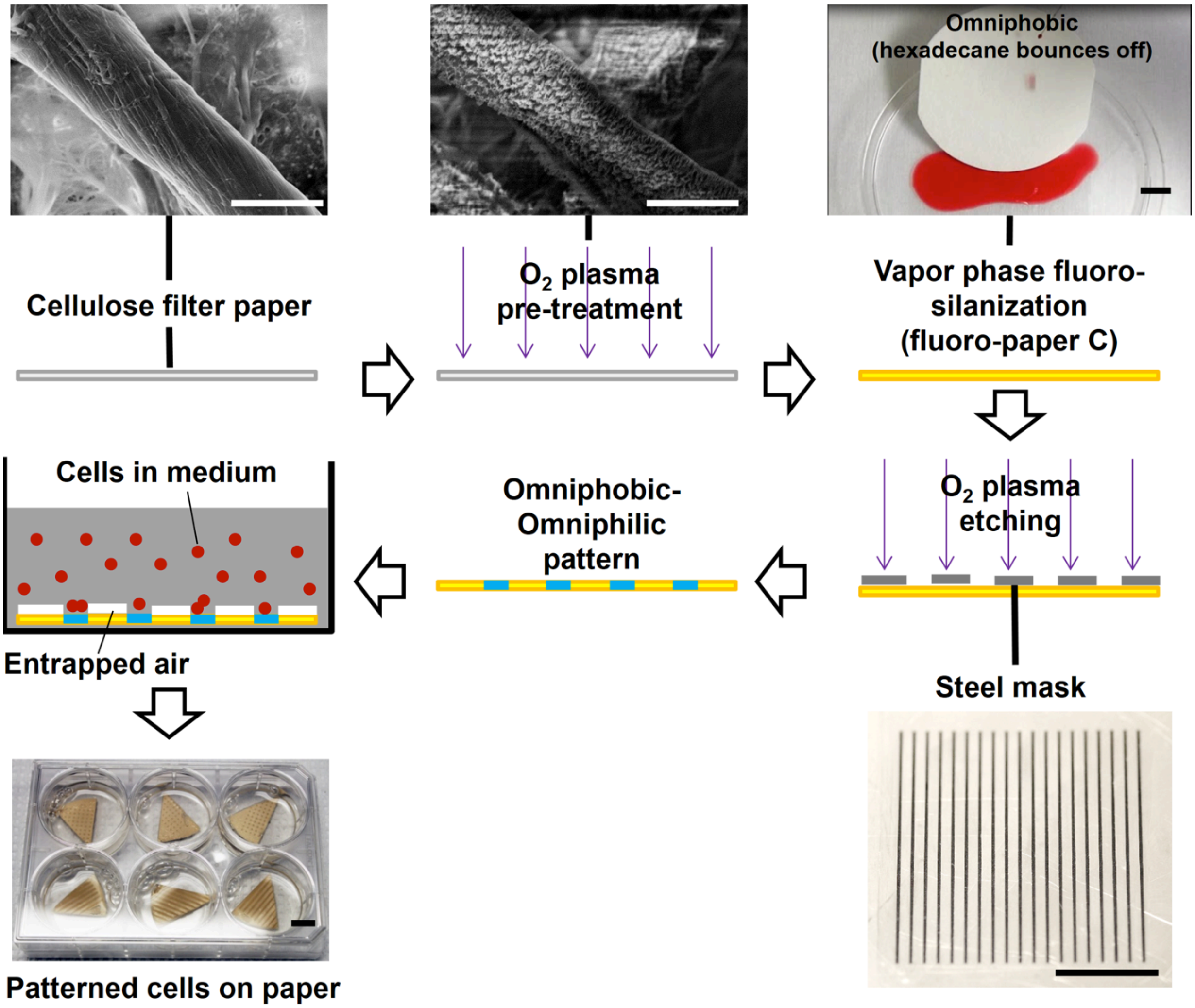
Omniphobic
(hexadecane bounces off)
Cellulose filter paper
$O_2$ plasma
pre-treatment
Vapor phase fluoro-
silanization
(fluoro-paper C)
Cells in medium
Omniphobic-
Omniphilic
pattern
$O_2$ plasma
etching
Entrapped air
Steel mask
Patterned cells on paper

**Figure 2.18.** Schematic illustration of the procedure employed to prepare omniphobic fluoro-paper C, omniphobic-omniphilic patterns on this surface, and their use for generating patterned OVCAR3 cell arrays. Scale bars on the SEMs are 10 μm. All other scale bars are 1 cm.

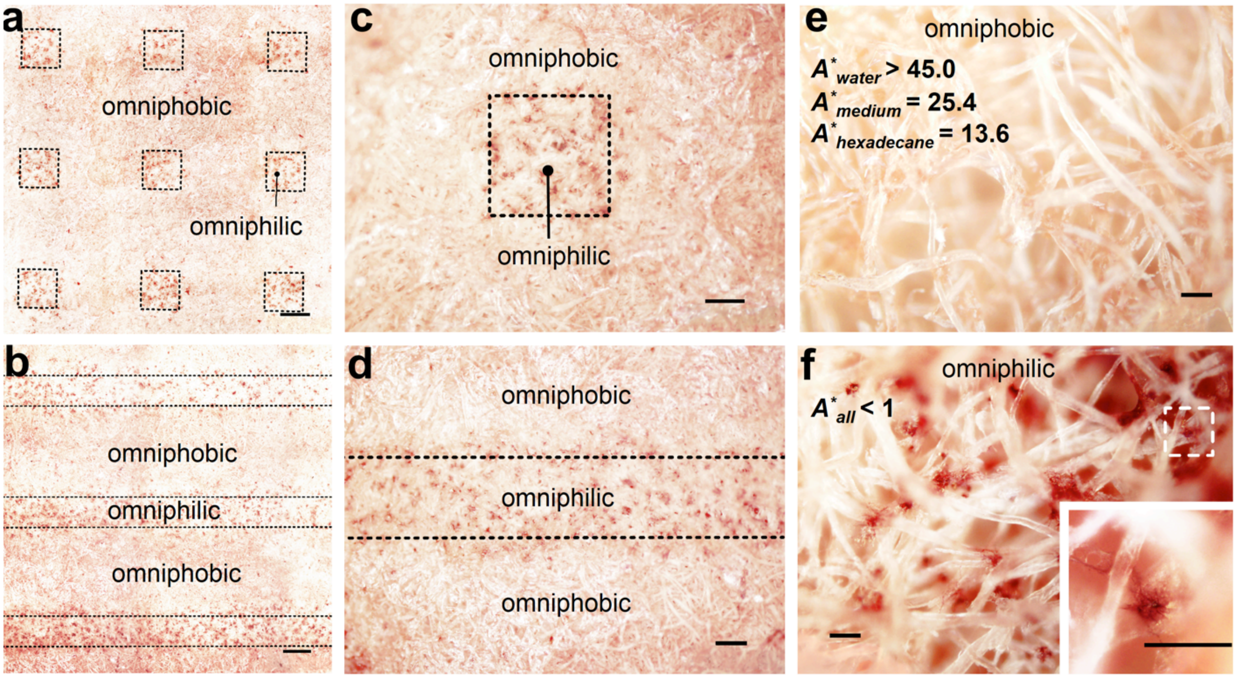
a
omniphobic
omniphilic
b
omniphobic
omniphilic
omniphobic
c
omniphobic
omniphilic
d
omniphobic
omniphilic
omniphobic
e
omniphobic
$A^*_{water} > 45.0$
$A^*_{medium} = 25.4$
$A^*_{hexadecane} = 13.6$
f
omniphilic
$A^*_{all} < 1$

**Figure 2.19.** Generation of cell microarrays on surfaces with patterned wettability. (a-f) Growth of OVCAR3 (ovarian cancer) cells on an omniphobic (fluoro-paper C) surface patterned with omniphilic domains. This paper has a high $A^*$ value for the growth culture medium used, ensuring longevity of the non-wetted state while immersed. The cells preferentially grow on the omniphilic regions and not on the omniphobic background. Scale bars are 500 μm in (a), (b), 200 μm in (c), (d), and 50 μm in (e), (f).

## 2.4 Conclusion

In summary, we have developed paper-based microfluidic devices that demonstrate, for the first time, all four possible combinations of extreme wettabilities with water and different oils. The fabricated devices allow for the selective localization, manipulation, and transport of virtually all high- and low-surface tension liquids based on differences in surface tension and/or polarity. The developed designs are compatible with both two-dimensional lateral flow, and three-dimensional multilayer flow, and can also be fabricated using a mask-free, direct printing technique. Finally, by enabling the generation of stable, immiscible organic-aqueous liquid-liquid interfaces in open channels, the fabricated devices greatly expand the potential applications of paper-based microfluidic devices in a wide range of fields such as oil-water separation, chemical analysis, purification, chemical/particle synthesis, and high-throughput testing of different bioactive substances.

## 2.5 Acknowledgements

We thank the National Science Foundation and the Nanomanufacturing program for supporting this work through grant #1351412 and through the Graduate Research Fellowship Program. We thank Dr. Ki-Han Kim and the Office of Naval Research (ONR) for financial support under grant N00014-12-1-0874. We also thank Dr. Charles Y. Lee and the Air Force Office of Scientific Research (AFOSR) for financial support under grant FA9550-15-1-0329. This work was performed in part at the University of Michigan Lurie Nanofabrication Facility.

# Chapter 3. Lysis and Detection of Coliforms on a Printed Paper-based Microfluidic Device

This work builds on the previous chapter with a specific application for one of the paper-based microfluidic devices. This is an excerpt from a manuscript submitted to *Advanced Materials* co-authored with Dr. Mathew Boban. Sarah Snyder performed all bacterial experiments, wrote and edited the manuscript.

## 3.1 Introduction

The coliform, *Escherichia coli,* is a major pathogen worldwide due to its ability to cause fatal diarrheal and extraintestinal diseases.[64] Currently, the 'gold standard' for the determination of *E. coli* contamination are methods that use automated polymerase chain reaction (PCR) and fluorescence detection.[65] While those systems can provide accurate results within 24 hours, they rely on expensive, complex instrumentation, as well as user expertise. With the numerous food safety incidents involving *E. coli* and *Listeria monocytogenes* in the last few years, there has been significant, recent interest in developing paper-based detection devices to not only reduce the cost of *E. coli* detection on a food-handling surface, but to also decrease the contamination detection time. Within the last ten years, paper-based microfluidic devices have been increasing in popularity due to their inexpensive nature and wide range of potential applications. They can also be flexible, simple to dispose, easy to scale up, facile to fabricate, and biocompatible.[21] Current paper-based devices for *E. coli* detection utilize a variety of mechanisms for rapid detection, including gold nanoparticle aggregation,[66, 67] Mie scattering, [68] and microfluidic origami.[69] However, these techniques can involve several complicated fabrication and experimental steps, including nanoparticle functionalization, antibody conjugation, and several folding and unfolding steps, respectively. We recently developed a simple, cheap device fabrication methodology to contain low surface tension liquids on paper.[5] However, while the channels could contain low surface tension liquids, they were not omniphilic enough to facilitate flow with higher surface tension liquids. In this work, we developed a new way of making omniphilic channels via titanium dioxide to design a device capable of not only containing low surface tension liquids, but also capable of promoting steady flow with high surface tension liquids. With these capabilities combined, we have created the first ever, all in one coliform lysis and colorimetric detection device that can be employed as an affordable, portable detector for water or food contamination.

To detect *E. coli*, we utilized chlorophenol red-*β*-D-galactopyranoside (CPRG) as a substrate for the enzyme, *β*-galactosidase (*β*-gal). *β*-gal is an enzyme present inside all coliforms, including *E. coli.* When *β*-gal cleaves the glycosidic bond within the CPRG substrate, the CPRG is converted to chlorophenol red, with an accompanying color change from vibrant yellow to a deep red-purple.[70] Reports have previously employed this method, utilizing a paper-based *μ*PAD and a hydrophobic sol-gel patterned paper-based device to detect *E. coli* at a concentration of $10^1$ colony forming units (CFU) $mL^{-1}$ in 12 hours and a concentration of $10^7$ CFU $mL^{-1}$ within 30 minutes, respectively.[71, 72] Still, these devices require at least two steps for sample analysis: lysing the bacterial cells to release the *β*-gal enzyme off-chip and adding the lysed cells to the paper-based device for detection. This is due to the fact that most paper-based microfluidics systems cannot contain low surface tension lysing solutions for extended periods.[45] However, recently developed paper devices have shown the capability to contain low surface tension liquids, including lysing solutions, but do not incorporate flow of both low and high surface tension liquids into their designs.[5, 72-78] Our work leverages these advances, surpasses their shortcomings, and presents, to the best of our knowledge, the first time that *E. coli* has been lysed and detected through $\beta$-gal on a simple, paper-based microfluidic device.

## 3.2 Materials and Methods

### *3.2.1 Substrate Preparation*

To produce a substrate resistant to wetting by most liquids, copy paper was reacted with a low surface energy fluorinated silane. The paper (Boise X-9 Multiuse OX9001, OfficeMax) was pre-treated with oxygen plasma to enhance reactivity (Harrick Plasma PDC-001, 250 mTorr, 30 W, 30 min). It was then placed into a vacuum oven held at <5 mmHg, 70 °C for 24 h with 400 μL of fluorosilane (heptadecafluoro-1,1,2,2-tetrahydrodecyl trichlorosilane, Gelest). The fluorosilane reacts with the hydroxyl groups on the plasma treated cellulose, rendering it non-wettable by most liquids. The advancing/receding contact angles were 153/0° and 113/0° for water and hexadecane, respectively.

### *3.2.2 Ink Preparation*

The omniphilic ink was composed of 70 wt.% $TiO_2$ and 30 wt.% polyurethane adhesive, dissolved at a concentration of 25 mg $mL^{-1}$ in acetone (Fisher Scientific), and agitated with a probe ultrasonicator (Heat Systems XL-2020) until evenly dispersed. Anatase titanium dioxide nanopowder (32 nm) was obtained from Alfa Aesar. Aleene's Fabric Fusion permanent fabric adhesive, a water-borne polyurethane, was used as the binder.

### *3.2.3 Device Fabrication*

Pieces of the fluorinated paper were adhered to glass slides with solvent resistant double-sided tape (3M 9629PC) and placed onto a leveled heated stage (~70 °C) in a lab-built printing apparatus (Figure 1b). This consisted of an XYZ motion stage (Shapeoko 2) holding a tapered polypropylene dispensing nozzle (20 gauge or 610 μm outer diameter, McMaster-Carr) connected via polytetrafluoroethylene tubing (1/32" inner diameter, McMaster-Carr) to a syringe pump (KD Scientific Model 200) dispensing the solution at 2.25 mL $h^{-1}$ from a glass syringe. The motion and operation of the pump and XYZ stage were computer-controlled with GCODE commands, which were generated from design files produced in Inkscape, an open-source vector drawing software. This apparatus allows the mask-free patterning of arbitrary polymer solutions on a variety of substrates with ~500 μm resolution. Two passes were performed to ensure uniform coverage of the $TiO_2$ ink on the fluorinated paper. Once deposited, the ink was exposed to 254 nm UV light in a sterilizer cabinet (purchased from Salon Sundry) for 5 hours to render it wettable by all liquids prior to use.

### *3.2.4 Device Testing*

Dynamic contact angles were measured on the fluorinated paper with a Ramé-Hart 200-F1 goniometer, using the sessile drop technique. Dyed deionized water, hexadecane (Alfa Aesar), 3 wt.% aqueous solutions of Triton X-100 (MP Biomedicals) and sodium dodecyl sulfate (Hoefer) surfactants, and 2X B-PER Bacterial Protein Extraction Reagent (Fisher Scientific) were used to test the capacity of the printed devices to contain a broad range of liquids. The pendant drop method was used to measure the surface tensions of these liquids with the goniometer.

### *3.2.5 Design of Cell Lysis Device*

An approximate model of the cell lysis device was generated in COMSOL 5.2 to guide the design of the channel to ensure thorough mixing of the cell lysis reagents and the *E. coli*, in order to enhance the reproducibility and speed of the assay. The central segment of the device was modeled as a laminar flow channel, with a no-slip boundary condition at the solid-liquid contact at the channel base, and a slip boundary condition for the liquid-air interfaces at the top and sides. A chemical species was introduced at one inlet of the flow channel, and its concentration was plotted to evaluate the effectiveness of mixing of various geometries. The results were compared to photographs taken of aqueous food-dye solutions (McCormick) mixing in the channels.

### *3.2.6 E. coli Culture and Growth*

Colonies of *Escherichia coli* (UTI89) were grown overnight at 37°C onto LB broth (Lennox) agar (from Fisher Scientific) plates and all colonies were used within two weeks of growth. To perform experiments, one colony scraped from the LB agar plate was grown in LB Broth (MP Biomedicals) on a shaker at 37°C with 10 mM isopropyl *β*-D-1-thiogalactopyranoside (IPTG, a lactose-like molecule used to induce *β*-gal production, purchased from Invitrogen). When the optical density at 600 nm reached 0.6 ± 0.1 (measured with an Ultrospec 2100 pro UV/Visible Spectrophotometer), indicating an approximate concentration of $10^7$ colony forming units (CFU) $mL^{-1}$, the *E. coli* were tested on the serpentine devices. Here, the term colony forming units is used in place of number of cells because although a cell may be viable, it is not necessarily culturable. The total concentrations of cells in all experiments performed were quantified by simultaneously plating on an LB agar plate while testing the devices.

For the sensitivity tests, one colony of *E. coli* was grown in LB until the optical density reached 0.6 ± 0.1. The *E. coli* in LB was serially diluted down to approximately $10^2$ CFU $mL^{-1}$ and 1 mL was placed into 99 mL of sterile LB, yielding an effective cell concentration of 1 CFU $mL^{-1}$. The *E. coli* were incubated with 10 mM IPTG and samples were taken out at various time points. At each time point, the withdrawn sample was used to measure optical density and to induce a color change on the diamond shaped devices.

### *3.2.7 Lysis-on-a-chip Assay*

1 μL of chlorophenol red-$\beta$-D-galactopyranoside (CPRG) (purchased from Sigma-Aldrich) dissolved in 2X Bacterial Protein Extraction Reagent (B-PER, purchased from Fisher Scientific) at a concentration of 3 mg mL$^{-1}$ was placed in the detection region of the device and allowed to evaporate. *E. coli* in LB and 2X B-PER were pipetted into their respective inlets and were allowed to wet the omniphilic regions of the device. Characterization images were taken on a Nikon D3200 camera with fixed exposure and lighting settings.

### *3.2.8 Image Thresholding*

All thresholding was performed in MATLAB R2014a. Counted, white pixels indicate RGB values where R > 140, G < 200, and B < 200 while black pixels indicated RGB values outside of those limits. Statistical analysis was performed with a standard two-sample t-test.

## **3.3 Results**

### *3.3.1 Printing Omniphilic Channels on an Omniphobic Paper Background*

Our paper-based microfluidic devices are designed with omniphilic domains printed on an omniphobic background. On most surfaces, a range of contact angles may be measured, from a maximum advancing contact angle when liquid is added to a droplet on the surface, to a minimum receding contact angle when liquid is removed from the droplet.[1, 2] Maximizing the advancing contact angle of the non-wettable background maximizes its capacity to contain a low surface tension liquid within a wettable channel, while minimizing the receding contact angle in the wettable domains allows for the retention of the working fluid.

To engineer the devices, we leveraged two key parameters: surface energy and roughness. We produced a low surface energy, rough background by covalently bonding a fluorinated silane to a fibrous paper substrate, rendering it omniphobic. Our choice of paper, composed of large, flat fibers with relatively high liquid-solid contact area, facilitated printability while maintaining the high advancing contact angles necessary for liquid confinement. To fabricate the omniphilic channels, we selectively printed omniphilic ink onto the omniphobic paper substrate. To minimize defects, the ink solution needed to leave a complete film when wiped across the substrate, that is, it needed to exhibit a low receding contact angle. Thus, we selected a high surface energy, nanotextured ink composed of titanium dioxide ($TiO_2$) nanoparticles and an adhesive polymer. $TiO_2$ is a well-known photocatalyst that undergoes a hydrophilic conversion upon UV irradiation.[79]

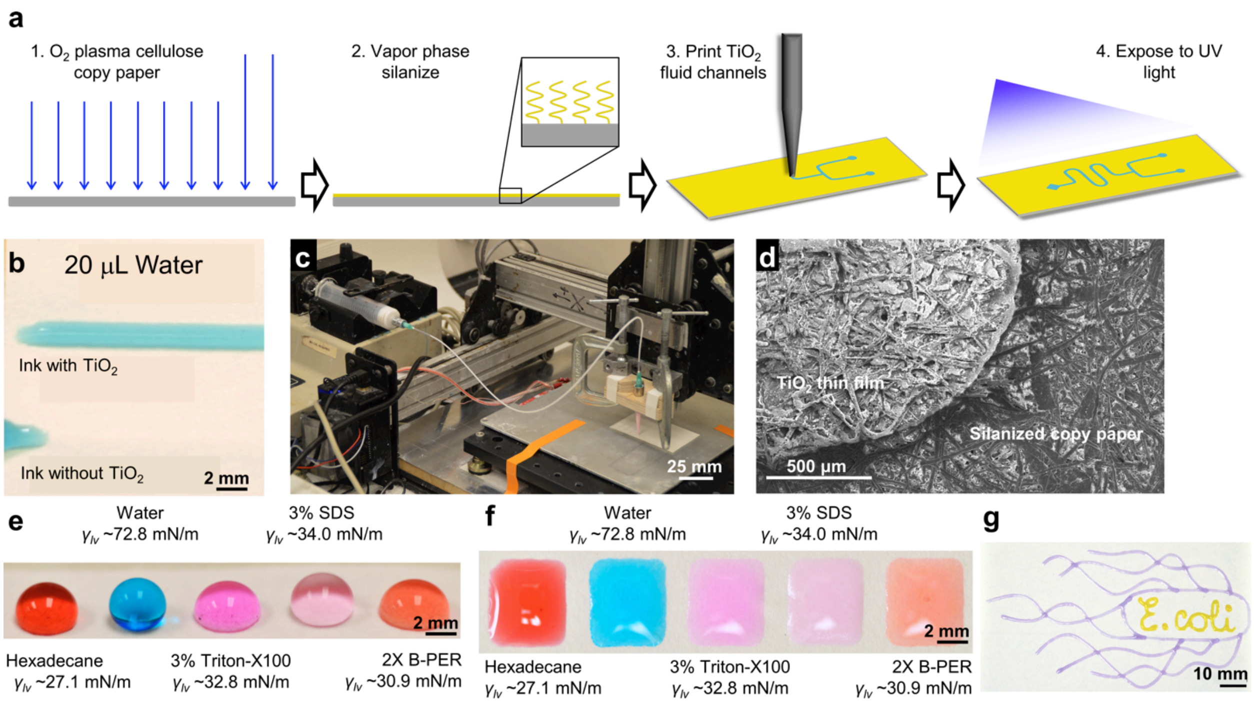
a
1. O2 plasma cellulose copy paper
2. Vapor phase silanize
3. Print TiO2 fluid channels
4. Expose to UV light
b
20 μL Water
Ink with TiO2
Ink without TiO2
2 mm
c
25 mm
d
TiO2 thin film
Silanized copy paper
500 μm
e
Water γlv ~72.8 mN/m
3% SDS γlv ~34.0 mN/m
2 mm
Hexadecane γlv ~27.1 mN/m
3% Triton-X100 γlv ~32.8 mN/m
2X B-PER γlv ~30.9 mN/m
f
Water γlv ~72.8 mN/m
3% SDS γlv ~34.0 mN/m
2 mm
Hexadecane γlv ~27.1 mN/m
3% Triton-X100 γlv ~32.8 mN/m
2X B-PER γlv ~30.9 mN/m
g
E. coli
10 mm

**Figure 3.1.** The fabrication and characterization of the paper-based *E. coli* detection devices. a) The steps required to manufacture a complete *E. coli* detection device, including $O_2$ plasma cleaning, vapor phase silanization with a fluorinated silane, printing of the $TiO_2$ channels and exposure of the devices to 254 nm

UV light. b) 20 μL of water wetting channels printed with and without ink containing $TiO_2$. The UV activated $TiO_2$ containing ink allows high surface energy water to easily wet the channel. c) The omniphilic channel printing apparatus developed using an XYZ stage can be utilized to print any device design. d) An SEM image shows the $TiO_2$ thin film on top of the silanized copy paper. e & f) Liquid drops repelled and contained on the omniphobic and superomniphilic regions, respectively. g) A channel in the shape of a single *E. coli* bacterium filled with dyed silicone oil ($\gamma_{lv}$ = 22 mN/m), demonstrates the ability to confine low surface tension liquids and to print any desired microfluidic channel shape with this technique.

After UV exposure, the $TiO_2$ printed channels were omniphilic enough to facilitate flow with both low and high surface tension liquids compared to our previously developed ink (Figure 3.1b). Figure 3.1a summarizes all fabrication steps, while Figure 3.1c shows the printing equipment setup. The deposited ink on omniphobic paper (Figure 3.1d) allowed a variety of liquids with high and low surface tensions to be contained within the omniphilic domains (Figure 3.1e,f). Controlled deposition of this material allowed the fabrication of microfluidic channels of any desired design (Figure 3.1g).

### *3.3.2 Optimization of the Printed Device Design*

Due to the laminar flow within microfluidic channels, with a low Reynolds number $R_e \approx$ 2.25 (assuming the density of the fluid is $\rho$ = 1,000 kg m$^{-3}$, the velocity of the fluid is $u$ = 1 mm s$^{-1}$, the characteristic linear dimension is $L$ = 2 mm, and the kinematic viscosity of water is $\mu$ = 8.9 x 10$^{-11}$ Pa s), it is difficult to achieve complete, homogenous mixing of two liquids. Therefore, we designed our device with two inlets leading into a serpentine mixing zone that ends at a detection patch. We simulated how adding 2, 3, 4 or 7 turns to the serpentine mixing zone affects the mixing of the two fluid streams with a simplified COMSOL model of the central section of the device. Figure 3.2a shows the concentration profiles obtained for the 0 and 7 turn open-channel devices. It is clear that increasing the amount of turns in the serpentine mixing section effectively increases the mixing between the two fluid streams.

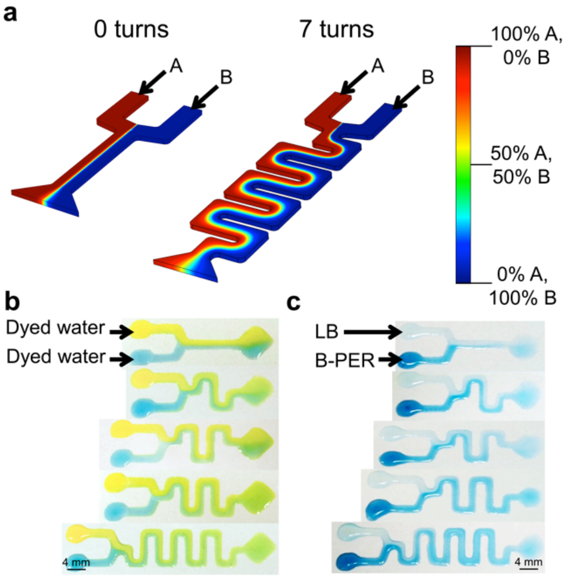

**Figure 3.2.** Optimization of device design to achieve complete mixing. a) Concentration profiles generated from COMSOL models of lysis devices with zero or seven turns in the mixing channel. Dark red represents a 100% concentration of liquid A and dark blue represents a 100% concentration of liquid B. (b-c) Images demonstrating the effective mixing in the serpentine region of the device with (b) dyed water and (c) LB and 2X B-PER. The addition of more turns in the serpentine region increased mixing, allowing for nearly homogenous mixing in the 7-turn device.

After fabricating all five devices, we experimentally tested the mixing effectiveness of the serpentine regions by adding water dyed yellow into one inlet and water dyed blue in the other. The results shown in Figure 3.2b exhibit that, as expected, adding more turns in the serpentine region increased mixing. There was a clearly defined interface in the detection region of the 0 turn device and as more turns were added, that interface became less clear until it was almost entirely mixed in the detection region of the 7 turn device. This matched the trend observed in the COMSOL model.

We also tested the mixing capability of all five devices for the *E. coli* assay by adding LB Broth (Lennox), the bacteria medium, in one inlet and blue-dyed 2X Bacterial Protein Extraction Reagent (B-PER), the lysis buffer, in the other, shown in Figure 3.2c. These results followed the same trend as those in Figure 3.2b, however, the two streams appeared to effectively mix within fewer turns when compared to the number of turns it took the dyed water to mix. This can be attributed to the Marangoni effect, which describes the mass transfer across an interface with a surface tension gradient,[80] as LB has an approximate surface tension of 72 mN m$^{-1}$ while 2X B-PER has an approximate surface tension of 31 mN m$^{-1}$. The Marangoni flow opposing the pressure-driven and capillary flows was clearly observable during the filling of the channels.

To optimize the design of the lysis-on-a-chip assay, two detection patch shapes, circles and diamonds, were considered because once the assay is performed, sensitive detection relies on the edge concentrating coffee ring effect.[81] Since the CPRG reagent is initially yellow and gradually transforms to a deep red, all three color channels (Red, Green, and Blue) need to be considered simultaneously. Figure 33a shows a schematic of all RGB colors and colors within the white box represent all possible colors that can be observed as the assay transforms from a bright yellow to a deep red.

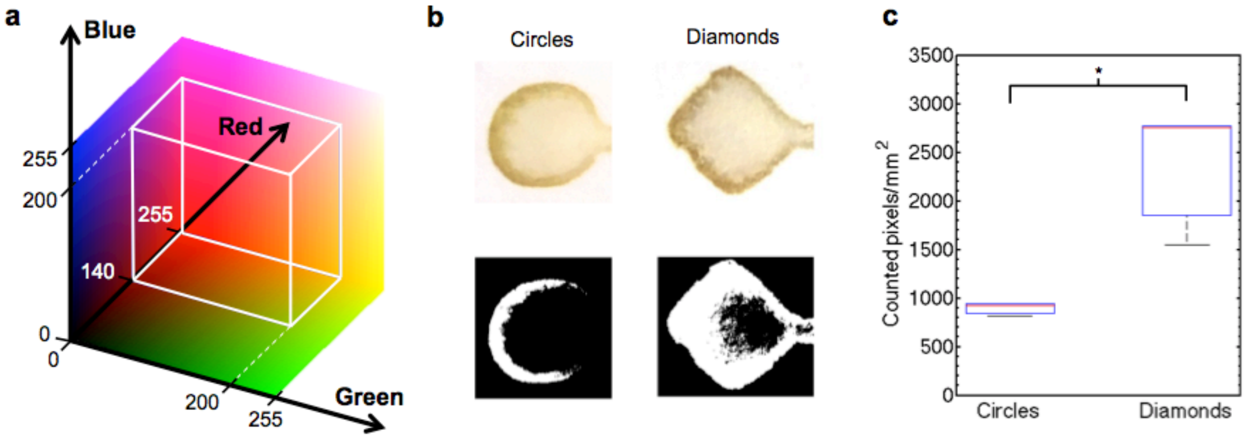

**Figure 3.3.** Optimization of the detection patch design. a) RGB schematic with a white outlined box showing the colors contained within the thresholding limits of R >140, G < 200, and B < 200. All pixels with RGB values within those limits indicate a color change and are counted, and pixels with RGB values outside those limits are ignored. b) Bright field images and corresponding processed images via thresholding for both circular and diamond shaped detection patches. c) Counted pixels per unit area of the processed images for both circular and diamond shaped detection patches. With a higher number of

counted pixels, diamond shaped detection patches exhibit a statistically significant ($p = 0.0228$) increase in sensitivity compared to circular detection patches.

Using these limits of R > 140, G < 200, and B < 200, we investigated which shape would be more optimal to maximize the coffee ring effect: circles or diamonds. Figure 3.3b shows the bright field images of the circular and diamond shaped patches along with their respective processed images via thresholding, where a white pixel indicates a pixel with RGB values within these limits. While it is visually clear that the diamond shaped patch has more white pixels or 'hits', Figure 3.3c plots the white counted pixels per unit area for both the circles and the diamonds. The statistically significant ($p = 0.0228$) difference in counts can be attributed to the increased perimeter to surface area ratio of the diamonds: for circles, the perimeter to surface area ratio is $2\pi r/\pi r^2 = 2/r$ and for diamonds, the ratio is $4r/r^2 = 4/r$. Thus, diamond shaped detection patches better enhance the coffee ring effect.

### *3.3.3 E. coli Detection*

To perform the lysis-on-a-chip assay, *E. coli* in LB with isopropyl *β*-D-1-thiogalactopyranoside (IPTG, a lactose-like molecule used to induce *β*-gal production)[82] and 2X B-PER were added to their respective inlets in the 7 turn mixing devices, as shown in Figure 3.4a. The 7 turn serpentine channel devices allowed for a residence time of about one minute, providing both diffusion across the interface and chaotic advection as mechanisms for mixing.[83] Figure 3.4a shows the time-lapse images of the *E. coli* (at a concentration of ~$10^7$ CFU $mL^{-1}$) mixing with the lysis buffer in the serpentine region of the device and the resultant color change after the solution reaches the detection patch. A color change initially becomes observable within 5 minutes after the liquid reaches the detection patch, but the change nearly reaches completion after about 15 minutes in the patch. Thus, the devices were not only able to contain the lysis buffer, but they successfully lysed the *E. coli*, releasing the $\beta$-gal within the cells and causing the CPRG to become chlorophenol red.

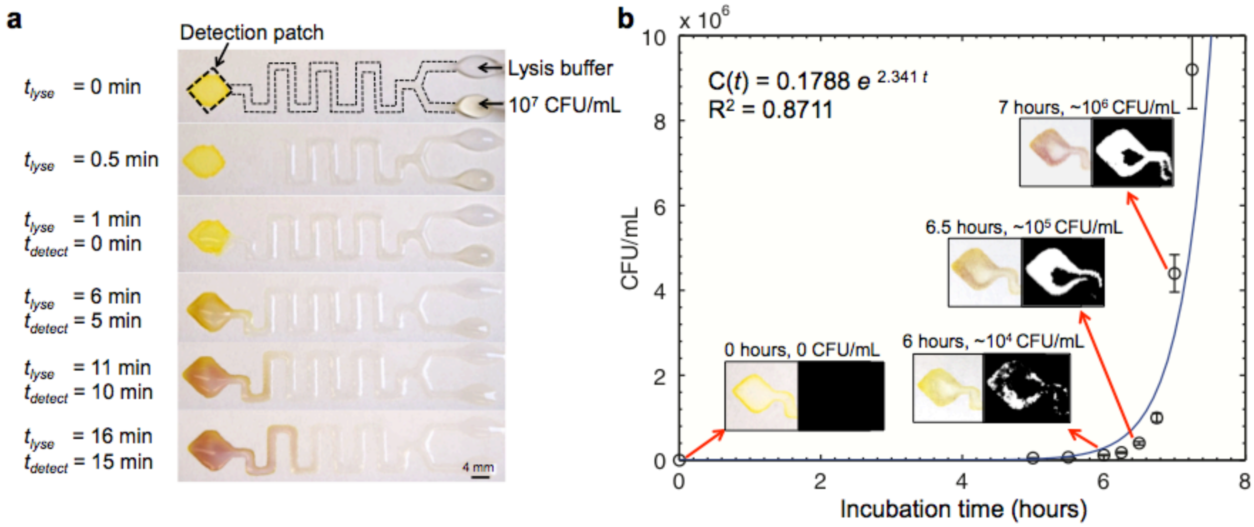

**Figure 3.4.** *E. coli* lysis and detection results on the paper-based device. a) *E. coli* lysed on chip at a concentration of ~$10^7$ CFU mL$^{-1}$ with the *E. coli* inlet, 2X B-PER lysis buffer inlet and the CPRG detection patch labeled. The *E. coli* spent approximately 1 minute mixing with the lysis buffer in the serpentine region before reaching the detection patch, and there was a noticeable color change within 5 minutes at the detection patch. After 15 minutes, the color change nearly reached completion. b) The growth curve and corresponding color change images with their respective processed images on the lysis devices for ~1 CFU mL$^{-1}$ incubated in medium over time. With a minimal detection limit of ~$10^4$ CFU/mL after 6 hours of incubation, there was a noticeable onset of color change.

For real-world applications, coliform detection devices need to be sensitive to much lower bacterial concentrations.[84] To address this issue, we incubated 1 CFU mL$^{-1}$ of *E. coli* in LB at 37 °C and tested the inoculum at various time points. Figure 3.4b shows the growth curve with the corresponding color changes and processed images within the diamond shaped patches indicated at their respective time points. With ~$10^4$ CFU/mL bacteria present after 6 hours, the color change started to become apparent to the naked eye, and after 7 hours, the color change nearly reached completion. Therefore, with minimal incubation time (> 6 hours), the diamond shaped devices were able to detect a low concentration of 1 CFU mL$^{-1}$, a concentration that is more applicable outside of the laboratory. However, without any incubation, the devices are capable of detection bacterial concentrations of ~$10^4$ CFU/mL.

## 3.4 Conclusion

In this work, we demonstrated the capability to create an all-in-one lab-on-a-chip device that can lyse and detect pathogenic *E. coli* within minutes. The device was composed of omniphilic channels fabricated on omniphobic paper with a direct printing technique, allowing rapid maskless fabrication of arbitrary channel geometries. The materials were engineered to contain the low surface tension lysing solution and to facilitate flow of the high surface tension bacteria sample. The channel was designed with a serpentine shape to ensure effective, homogenous mixing of the *E.* coli and the lysing solution prior to detection. After lysing, the enzyme, *β*-galactosidase, was used to determine the presence of *E. coli* (at a minimal concentration of $10^4$ CFU $mL^{-1}$) in the contaminated sample with a yellow to red colorimetric assay. A dilute sample at only 1 CFU $mL^{-1}$ was detectable by incubation prior to introduction to the device, allowing detection within 6 hours. While this device was only shown to detect *E. coli*, the printing fabrication method allows for versatility in developing essentially any 2D open-channel paper-based microfluidic device, opening the door to a plethora of potential bio-applications.

## 3.5 Acknowledgments

We thank the National Science Foundation Graduate Research Fellowship Program. This work was supported by the DOD OCRP Early Career Investigator Award W81XWH-13-1-0134 and DOD Pilot award W81XWH-16-1-0426. Research reported in this publication was supported by the National Cancer Institute of the National Institutes of Health under award number P30CA046592.

# Chapter 4. Long Lasting Antimicrobial Surfaces Based on the Crosslinking of Natural Oils within Polymer Networks

This work is an excerpt from a U.S. Patent Application with Serial No. 62/671,060 filed May 14, 2018. Sarah Snyder wrote the Patent Application and contributed to the majority of the experiments developing the surface as well as testing the surfaces against bacteria.

## 4.1 Introduction

Antifouling and antibacterial surfaces have been of extreme interest due to a plethora of potential applications ranging from saving lives with medical devices to preventing hospital acquired infections, and even prevention of marine biofouling. Currently, there is no surface that can completely resist bio-adhesion from a variety of biomolecules for an extended period of time.

To create antifouling surfaces, much research has gone into testing surfaces that will repel the attachment of microbes. In particular, surfaces with different wettabilities have been investigated as microbes preferentially adhere to hydrophobic surfaces (as cell proteins are comprised of long, hydrophobic carbon chains). Therefore, the approach of making antifouling surfaces out of hydrophilic surfaces has been extensively studied with polyethylene glycol (PEG) and zwitterionic polymer surfaces.[85] Superhydrophilic surfaces, i.e. surfaces with approximately a 0° contact angle with water,[2] have been shown to repel proteins better than hydrophilic surfaces.[86] However, as these hydrophilic or superhydrophillic surfaces can degrade, they can become more hydrophobic over time, allowing microbes to eventually attach.

Achieving a long effective lifetime of antifouling surfaces has been a challenge and several different approaches involving extreme wettabilities have been developed.[87] The first approach involves incorporating scales of roughness onto a hydrophobic polymer surface. With surface roughness, surfaces are in the Cassie-Baxter or composite state and microbes are effectively in contact with only a fraction of the surface with the liquid sitting on many tiny air bubbles.[88] Several groups have studied the anti-fouling effects of a microstructured polydimethylsiloxane (PDMS) surface,[89-92] a polystyrene and polylactic acid composite surface,[93] and a nano-rough polysiloxane surface.[94] Other techniques achieve superhydrophobicity and omniphobicity by combining different approaches. Slippery liquid-infused porous surfaces (SLIPs) are tethered polymer surfaces infused with an immobilized fluorinated liquid so a droplet in contact with the surfaces is only in contact with the fluorinated liquid.[95] Another technique utilizes an amphiphilic block copolymer design based on polystyrene and polyacrylate blocks,[96] and an additional method coats silica nanoparticles onto precipitated polymer spheres to get hierarchal microgel spheres that are then re-coated with a hydrophilic polymer.[97] However, all of these approaches focus on eliminating biomolecule attachment and have no cytotoxic components; microbes are simply relocated elsewhere and still persist in the environment.[98] Additionally, although textured hydrophobic surfaces initially reduce microbial attachment, bacteria still manage to overcome unfavorable surface topographies and attach to the entire surface.[99] Finally, the abrasion resistance of these surfaces has generally been poor, rendering them ineffective as surfaces that possess persistent (> 1 month) antimicrobial properties in real-life conditions.

Utilizing a cytotoxic component is a much simpler approach for antimicrobial activity. The properties of essential oils have been explored in a number of ways, as it is well known that many essential oils possess antibacterial properties.[100-103] Unfortunately, although essential oils are antimicrobial, they are extremely volatile and evaporate very quickly.[104] The most common solution to the volatility issue is to use some form of encapsulation.[105, 106] One particular system utilizes a surfactant to maintain a micro emulsion of essential oils in an aqueous phase for cleaners and disinfectants.[107] Other systems utilize sodium alginate[108] to encapsulate the essential oils for applications such as wound dressing.[109] Another solution to extreme volatility is to use physical methods to immobilize the molecules of the essential oils and to limit their evaporation. Suggested methods include oils coated onto nanoparticles,[110] oils mixed into a polymeric network via an extruder,[111] and adding a fragrance into a polyurethane foam for air freshening applications.[112] However, since these methods only physically immobilize the molecules of the essential oils, it is just a matter of time before all the molecules evaporate and the antimicrobial activity ceases to exist.

To the best of our knowledge, no one has chemically reacted in an essential oil into a crosslinked polymer network for long-lasting antimicrobial effects. In this work, we chemically react an antimicrobial essential oil, namely, tea tree oil, into the polymer simultaneously as the diisocyanate and polyol react to form a polyurethane. Tea tree oil is a well-known, natural, antibacterial oil[113] that has been used for the treatment of different infections[114-116] for over a century.[117, 118] The oil is non-toxic[118], has anti-inflammatory properties[117], and already approved as an active agent for use within wound care by the FDA[119]. Another natural antimicrobial oil, eucalyptus oil, can be similarly crosslinked within a polyurethane matrix, using the same polyol – isocyanate bond. The result is an antifouling polyurethane with a partial amount of ‘free’ essential oil within the polymer network stabilized by the rest of the crosslinked essential oil. The tea tree oil containing polyurethane is highly abrasion resistant, and is capable of reducing bacteria adhesion by at least 99% even when left exposed to air for 12 weeks.

## 4.2 Materials and Methods

### *4.2.1 Surface Fabrication*

Polystyrene (PS) surfaces – Surfaces were fabricated using sterile PS petri dishes obtained from Fischer Scientific. The surfaces were cleaned and then exposed to UV light for 30 minutes to guarantee sterility.

Polyurethane (PU) surfaces – Desmophen 670 BA (polyol) and Desmodur N3800 (diisocyanate) were purchased from Covestro and mixed at a weight ratio of 0.5363:0.4637, respectively. Essential oils, tea tree (TTO) and eucalyptus oil (purchased from Jedwards International, Inc.), and essential oil components (Sigma) were added to the uncured polyurethane mixture by weight percent, where 30% oil equals 30% of the total polyurethane plus oil weight. The solutions were then drop casted onto a glass slide, allowed to cure in a chemical fume hood for at least 4 days, and then exposed to UV light for 30 minutes to guarantee sterility. Typical coating thickness was about 1.5 - 2 mm.

Polydimethylsiloxane (PDMS) surfaces – Mold Max Stroke® (Smooth-On Inc.) was mixed in a 10:1 base:crosslinker ratio, following the manufacturer's instructions. 10 g of total material was taken and the mixture was vortexed until homogeneous. To make an antimicrobial sample, 30 wt% tea tree oil was added and vortexed. The mixture was then cast over a glass slide, allowed to cure in a chemical fume hood for at least 4 days, and then exposed to UV light for 30 minutes to guarantee sterility. Typical coating thickness was about 1.5 - 2 mm.

Epoxy surfaces – 100 parts of EpoxAcast® 650 (Smooth-On Inc.) was mixed thoroughly with 12 parts of 101 Hardener, following the manufacturer's instructions. 10g of total material was taken and the mixture was stirred until homogeneous. To make an antimicrobial sample, 30 wt% tea tree oil was added and vortexed. The mixture was then cast over a glass slide, allowed to cure in a chemical fume hood for at least 24 hours, and then exposed to UV light for 30 minutes to guarantee sterility. Typical coating thickness was about 1.5 - 2 mm.

### *4.2.2 Surface Characterization*

Contact angle measurements – Dynamic contact angles were measured with water on the polyurethane surfaces with a Ramé-Hart 200-F1 goniometer, using the sessile drop technique.

Thermogravimetric analysis (TGA) – Weight loss measurements were conducted on the Q5000IR by TA Instruments. The weight loss of the samples was observed under nitrogen atmosphere and an isothermal temperature of 200 °C for 200 minutes after a ramp of 10 °C/min. Weight loss percentage was recorded at 100 minutes for each sample.

Gas Chromatography - Mass Spectroscopy (GC-MS) – Oil sample composition was determined using the Shimadzu QP-2010 GCMS consisting of a Supelco SLB®-5ms Capillary GC Column (L × I.D. 30 m × 0.25 mm, df 0.25 μm). The sample was injected at a temperature of 200 °C using split mode (split ratio = 100), and the mass spectrometer was operated in scan mode with a mass range (m/z) of 35 to 400. Helium was used as the carrier gas.

### *4.2.3 Antibacterial Performance*

Bacteria culture and growth – Colonies of *Escherichia coli* (UTI89) and *Staphylococcus aureus* (COL) were grown overnight at 37°C onto Lysogeny broth (LB) agar (from Sigma-Aldrich) and Tryptic Soy Agar (TSA, from Sigma-Aldrich), respectively. All colonies were used within two weeks of growth. To perform experiments, one colony of *E. coli* or *S. aureus* scraped from the LB agar or TSA plate was grown in LB media (Sigma-Aldrich) or tryptic soy broth (1% glucose weight to volume, TSBG, Sigma-Aldrich), respectively, on a ThermoForma orbital shaker un-humidified at 37°C and 200 rpm. When the optical density (OD) at 600 nm reached 0.5 ± 0.1 (measured with an Ultrospec 2100 pro UV/Visible Spectrophotometer) for *E. coli* and 0.6 ± 0.1 for *S. aureus*, respectively, indicating an approximate concentration of $10^7$ colony forming units (CFU)/mL. The culture was then diluted until the OD reached 0.02 ± 0.005, representative of about one million CFUs in 100 microliters of culture, and then bacteria were used to test the antifouling capability of our surfaces. Here, the term colony forming units is used in place of number of cells because although a cell may be viable, it is not necessarily culturable.

Quantitative culture – The sterilized surfaces were cut to fit the width of the well in a 48 well plate (approximately 0.5 cm by 1 cm) and placed vertically in the well with approximately one million CFUs total in 1 mL of TSBG. The well plates were then placed on the orbital shaker at 37°C for 24 hours. After completion of the experiment, the incubated surfaces were removed from culture, rinsed and placed in sterile phosphate buffered saline (PBS, Thermo Fisher Scientific). They were then sonicated to remove adhered bacteria from the surface, 7 minutes and 12 minutes for *E. coli* and *S. aureus*, respectively, and the acquired solution was then serially diluted in PBS and 10 microliters of each dilution was drop-casted onto TSA plates. The plates were given time to incubate un-humidified at 37°C overnight and results were determined by colony enumeration to quantify the number of bacteria adhered to the antifouling polyurethane surfaces.

Contact plate experiments – The sterilized surfaces were cut to an approximate 1 cm x 1 cm square and bacteria were grown according to the aforementioned protocol. Once the culture reached half-log, it was then centrifuged for two minutes at 8000 RPM using a ThermoScientific Sorvall Legend Micro 17R centrifuge. The resulting bacteria pellet was resuspended in 1 ml of 1X PBS and this rinsing process was carried out two additional times. Finally, the culture was then diluted further and 1 mL of 1X PBS with approximately $10^6$ CFU/mL was pipetted onto each test surface and left in contact for 10 minutes. After the exposure time, the excess liquid was wicked off and dabbed lightly with a sterilized Kimwipe. The exposed surface was then gently placed in contact with agar plates (LB and TSA agar for *E. coli* and *S. aureus*, respectively) for one minute. After the contact time, the surface was removed, and the agar plates were incubated un-humidified at 37 °C for 24 hours. Three replicates were tested for each specimen and results were determined by colony enumeration for each of the samples.

ISO 22196 testing – International Organization for Standardization ISO 22196, Antibacterial Products – Test for Antibacterial Activity and Efficacy, was carried out by Microchem Laboratory (Round Rock, TX) with both *E. coli* (8739) and *S. aureus* (6538).

### *4.2.4 Durability Testing*

Linear TABER Abrasion – Mechanical abrasion was performed using a Linear Taber Abrasion machine with a CS-10 resilient abrader and a total weight of 1100 g. The abrader was refaced before each set of abrasion cycles using sand paper (from Taber). Refacing was done at 25 cycles/min for 25 cycles. For abrasion, samples were clamped down and abraded for up to 1000 cycles at 60 cycles/min and a stroke length of 50.8 mm. Percent mass loss was calculated over the abraded area.

Environmental exposure – To test the longevity of the antibacterial samples, samples were left in a chemical fume hood, uncovered, with a face velocity of 115 fpm at a 14 inch or 35.56 cm sash height.

## 4.3 Results & Discussion

### *4.3.1 Engineering the surface*

To create our unique antifouling surfaces, we combined the basis of a polyurethane rubber, a diisocyanate plus a polyol, with tea tree oil or eucalyptus oil. Tea tree oil and eucalyptus oil are natural oils comprised of many different organic molecules with compositions that can vary depending on the part of the globe the oil is harvested from and the time of year at which it is harvested. Table 4.1 shows the compositional make up of our oils; about 48% and 91% of the molecules in tea tree oil and eucalyptus oil, respectively, are capable of reacting with the diisocyanate as the polyurethane crosslinks, while the rest of the other molecules are most likely not going to react.

**Table 4.1.** The various individual tea tree and eucalyptus oil components and their relative weight percentages. About 48% of the tea tree oil is capable of reacting with the diisocyanate from the polyurethane while the rest of the tea tree oil is not.

| Component | % in Tea Tree Oil (by weight) | % in Eucalyptus Oil (by weight) | Structure |
|---|---|---|---|
| Terpinen-4-ol | 40.6 | - | 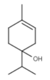 |
| γ – terpinene | 23.6 | 3.45 | 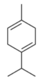 |
| (+)-4-carene | 12.4 | - | 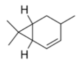 |
| Eucalyptol | 5.05 | 91.0 | 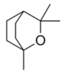 |
| (+)-2-carene | 4.13 | - | 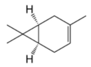 |
| p-cymene | 2.89 | 4.05 | 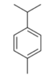 |
| α-pinene | 2.83 | - | 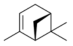 |
| α-terpineol | 2.27 | - | 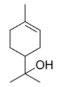 |
| Limonene | 1.29 | - | 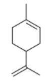 |

Therefore, the structure of our antifouling polyurethane consists of many polyurethane chains forming the backbone of our polymer network with a partial amount of the oil chemically crosslinked onto a few chain ends and the rest of the oil ‘free’ but stabilized within the network, as shown by Figure 4.1. Most of the ‘free’ oil assembles at the surface to reduce the overall free energy of the system, adding to the surface’s antibacterial capabilities. It is important to note that since tea tree oil contains fewer molecules with alcohol groups compared to eucalyptus oil, the ratio of ‘free’ oil to crosslinked oil will be higher in tea tree oil than eucalyptus oil.

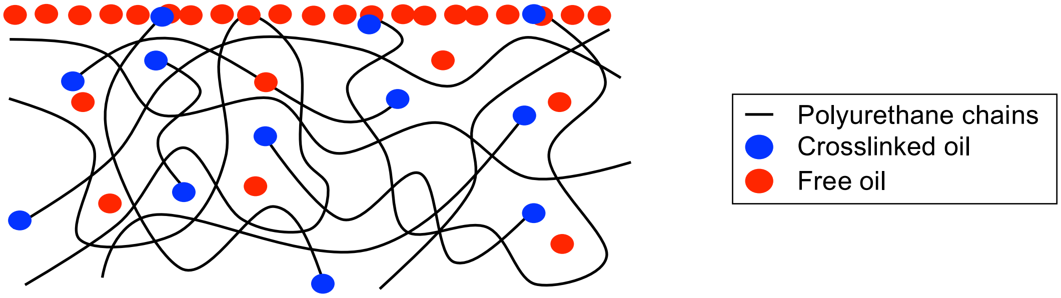

**Figure 4.1.** A schematic showing free oil (red circles) stabilized by oil crosslinked (blue circles) into the crosslinkable polymer (polyurethane in this case) network (black lines). While some free oil remains in the bulk, most assembles onto the surface.

While essential oils are the antibacterial component of our surface, they are very volatile and prone to quick evaporation, making stability a major factor in the surface's design. For one particular system, we reacted 30% of tea tree oil (TTO) into a Desmo polyurethane (PU) and compared it to a pure Desmo PU swelled 30% in TTO. Figure 4.2 displays the TGA curves for the pure Desmo PU, the Desmo PU reacted with 30% TTO (PU + 30%TTO) and the pure Desmo PU swelled in TTO at the 200 °C isotherm. Using the 2% weight loss from the pure Desmo PU as a baseline, results show that the swelled Desmo PU in TTO loses ~29 wt % while the Desmo PU reacted with 30% TTO loses only ~10 wt %. This indicates that the addition of the TTO prior to the PU reaction chemically crosslinks in ~20% of the TTO, proving an increase in stability compared to the PU simply swelled in TTO. It is this chemically reacted in 20% that increases the longevity of the additional 10% of 'free' oil, the fraction needed for long lasting antimicrobial effects.

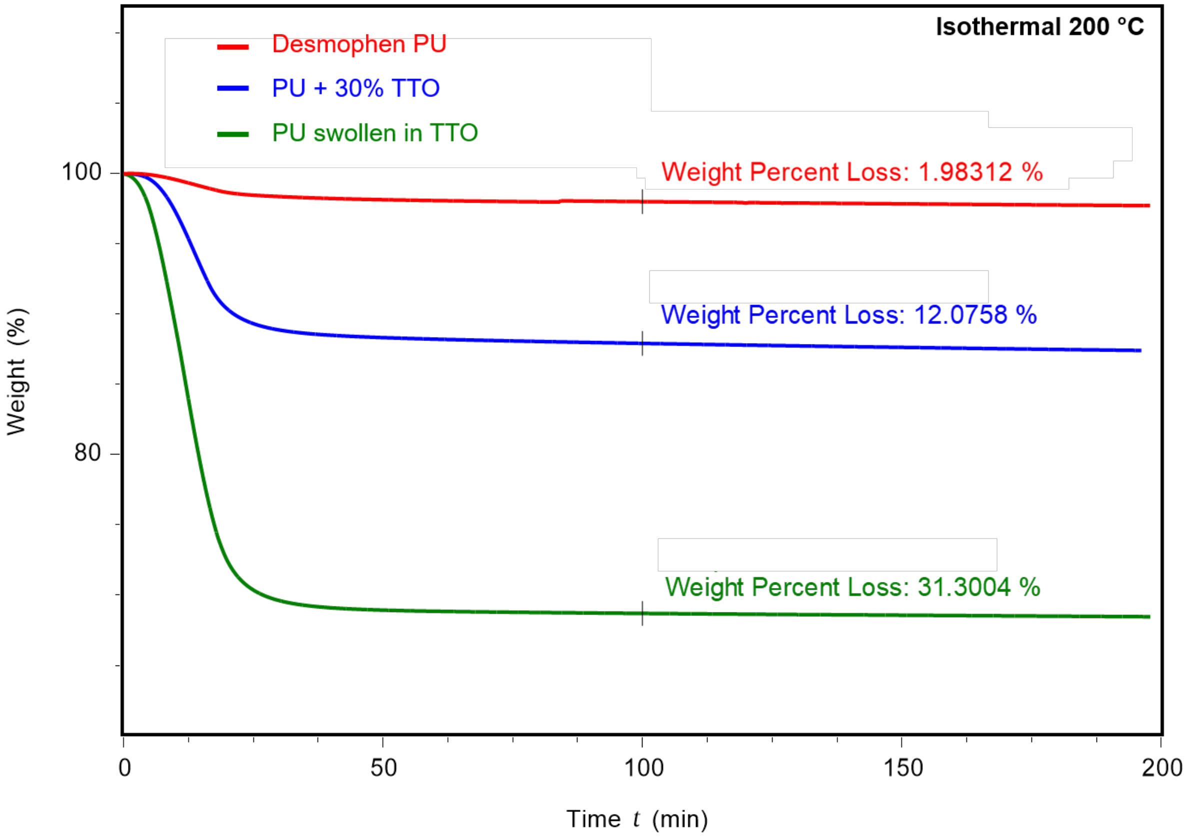

**Figure 4.2.** Thermogravimetric analysis (TGA) data of the Desmo PU (red), Desmo PU reacted with 30% TTO (blue), and Desmo PU swelled in TTO (green) at the 200 °C isotherm. Desmo PU loses ~2 wt % while Desmo PU reacted with TTO loses ~12 wt %, indicating the presence of ~10 wt % of free oil in the reacted samples. The Desmo PU that was simply swelled with TTO loses ~29 wt % and when compared to the Desmo PU reacted with TTO sample, the higher weight loss percentage is attributed to the lack of TTO stability within the Desmo PU network, both chemically and physically. Thus, reacting in the TTO with the Desmo PU instead of simply swelling the PU fabricates a more stable PU + TTO network.

### *4.3.2 Bacterial Testing*

Using this design, we tested the antibacterial effects of different essential oils and their components within our surfaces against *Escherichia coli* (gram-negative) and *Staphylococcus aureus* (gram-positive) via entire sample incubation with colony enumeration (quantitative culture) and surface incubation with colony enumeration (contact plating). Table 4.2 outlines every tested surface, with tea tree oil performing better than eucalyptus oil in the Desmo PU, even though both oils are antibacterial, due to tea tree oil's higher ratio of 'free' to crosslinked oil.

**Table 4.2.** Adhered bacteria per unit surface from quantitative culture experiments conducted on surfaces with various essential oils and essential oil components. The lower the number of colony forming units (CFU) on a tested surface, the better their antimicrobial performance. The data is presented as log(CFU). Tested surfaces had a surface area of 100 mm$^2$ and at least three replicates were tested for each surface.

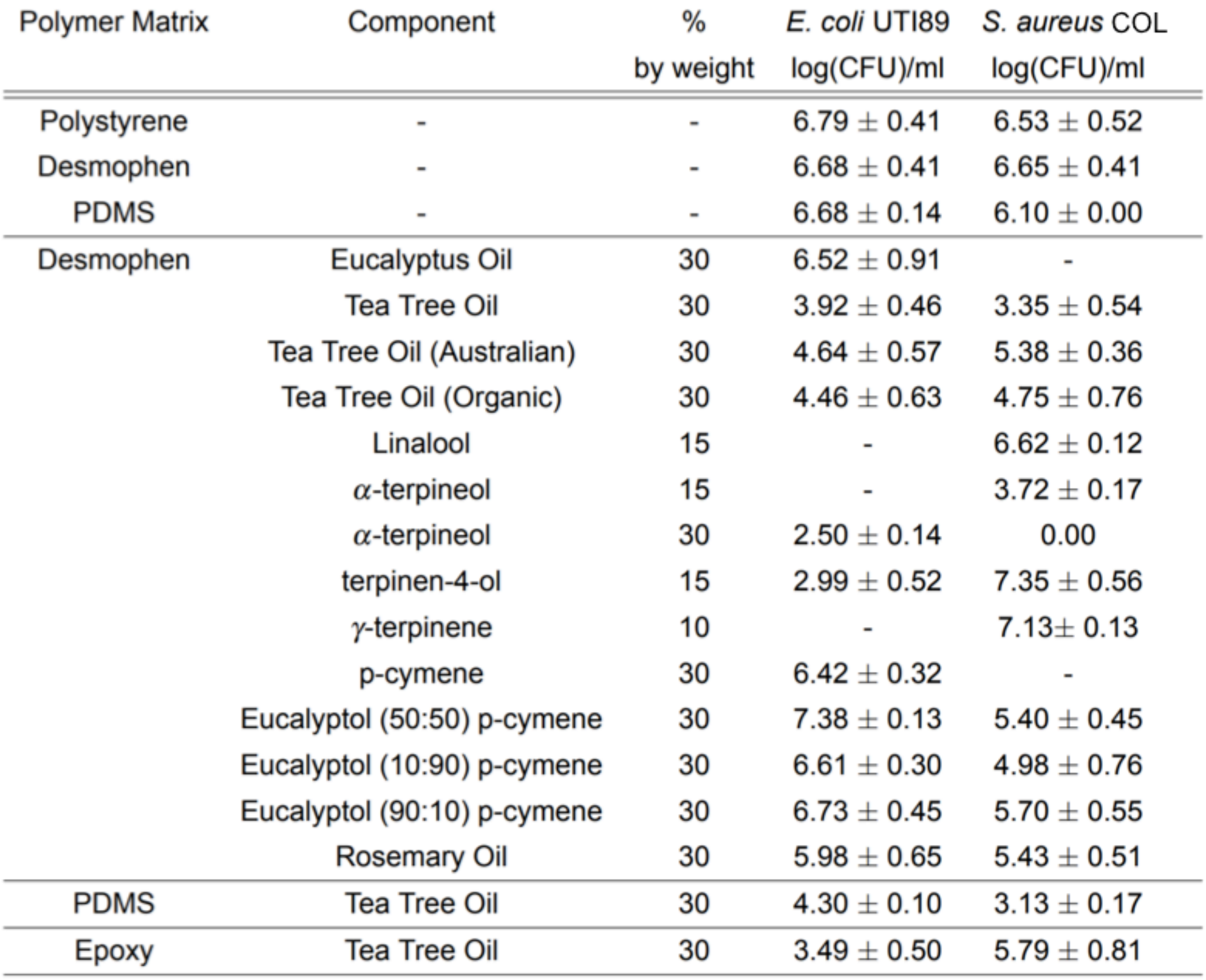

| Polymer Matrix | Component | % by weight | *E. coli* UTI89 log(CFU)/ml | *S. aureus* COL log(CFU)/ml |
|---|---|---|---|---|
| Polystyrene | - | - | 6.79 ± 0.41 | 6.53 ± 0.52 |
| Desmophen | - | - | 6.68 ± 0.41 | 6.65 ± 0.41 |
| PDMS | - | - | 6.68 ± 0.14 | 6.10 ± 0.00 |
| Desmophen | Eucalyptus Oil | 30 | 6.52 ± 0.91 | - |
| | Tea Tree Oil | 30 | 3.92 ± 0.46 | 3.35 ± 0.54 |
| | Tea Tree Oil (Australian) | 30 | 4.64 ± 0.57 | 5.38 ± 0.36 |
| | Tea Tree Oil (Organic) | 30 | 4.46 ± 0.63 | 4.75 ± 0.76 |
| | Linalool | 15 | - | 6.62 ± 0.12 |
| | $\alpha$-terpineol | 15 | - | 3.72 ± 0.17 |
| | $\alpha$-terpineol | 30 | 2.50 ± 0.14 | 0.00 |
| | terpinen-4-ol | 15 | 2.99 ± 0.52 | 7.35 ± 0.56 |
| | $\gamma$-terpinene | 10 | - | 7.13± 0.13 |
| | p-cymene | 30 | 6.42 ± 0.32 | - |
| | Eucalyptol (50:50) p-cymene | 30 | 7.38 ± 0.13 | 5.40 ± 0.45 |
| | Eucalyptol (10:90) p-cymene | 30 | 6.61 ± 0.30 | 4.98 ± 0.76 |
| | Eucalyptol (90:10) p-cymene | 30 | 6.73 ± 0.45 | 5.70 ± 0.55 |
| | Rosemary Oil | 30 | 5.98 ± 0.65 | 5.43 ± 0.51 |
| PDMS | Tea Tree Oil | 30 | 4.30 ± 0.10 | 3.13 ± 0.17 |
| Epoxy | Tea Tree Oil | 30 | 3.49 ± 0.50 | 5.79 ± 0.81 |

Since the crosslinked oil stabilizes the 'free' oil, we presume that the correct ratio of molecules with and without alcohol groups is key to designing an optimized, long-lasting antibacterial surface. It is worth noting, that the addition of tea tree oil into a polydimethyl siloxane (PDMS) network and into an epoxy network, where presumable the oil is only physically crosslinked, also greatly reduces bacteria adhesion at least initially, though these surfaces do not have the same longevity.

The data in Table 4.2 also shows that tea tree oil obtained from different sources can have different antimicrobial performance. This is likely due to differences in the composition of the oil harvested by different sources and / or at different times of the year. We were also able to identify a single component of tea tree oil that shows exceptional antimicrobial performance once crosslinked within a polyurethane. a-terpineol when crosslinked at 30 wt% within the polyurethane led to a > 4 log reduction (4 orders of magnitude) of both *E. coli* and *S. aureus* colonies. Crosslinked a-terpineol seems to have the best antimicrobial performance, at least initially, when compared with all compounds tested in this work. Other components of tea tree oil, such as p-cymene, a well-known antimicrobial compound[120], proved to be ineffective. This is likely because p-cymene cannot react with any of the polyurethane monomers (particularly isocyanates).

Utilizing polyurethane containing tea tree oil as our optimized surface, Figure 4.3 shows the resultant adhered bacteria per unit area from the quantitative culture experiments. When compared against the pure Desmo PU, our 30% TTO surface shows a 99.8% reduction (~2.7 log reduction) and 99.9% reduction (~3.3 log reduction) with both *E. coli* and *S. aureus*, respectively. Even after the samples were left uncovered in a chemical fume hood for 12 weeks, they still displayed 99% reduction (~2.5 log reduction) for *E. coli* and a 99% reduction (~3.2 log reduction) for *S. aureus*. In comparison, while epoxy and PDMS surfaces with 30% TTO showed an initial reduction in adhered bacteria (at least 99% or >2 log reduction for both bacteria), after two weeks of chemical fume hood exposure the surfaces completely fouled. This is due to how tea tree oil is only physically mixed into the epoxy and PDMS networks, further validating the requirement of chemically reacting in a fraction of oil to maintain the surface's stability over longer periods of time. Note that this is somewhat of an accelerated test, as there is always a high flow rate of air on top of the surface within the hood. This flow of air will likely increase the evaporation rate of the TTO significantly.

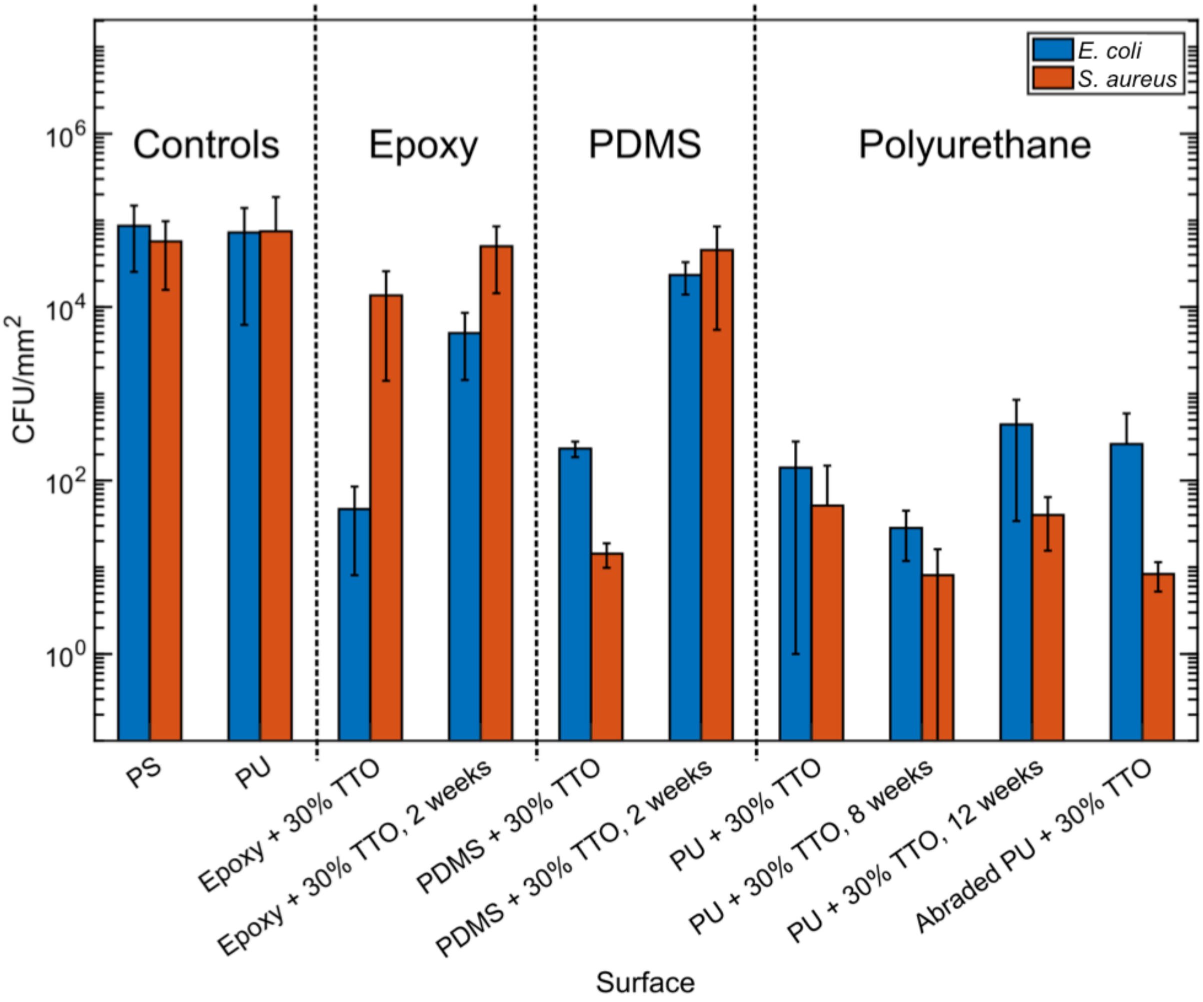

**Figure 4.3.** Bar graph representation of the adhered bacteria data for various surfaces and various surface testing conditions with both *E. coli* (blue) and *S. aureus* (red). All PU surfaces reacted with 30% TTO show at least a ~2.4 log reduction of adhered bacteria when compared to the PS and PU controls, with the fresh PU + 30% TTO samples showing a 99.8% and 99.9% reduction of adhered bacteria with *E. coli* and *S. aureus*, respectively, when compared to the Desmo PU. Results are similar with the abraded samples (99.6% and 99.9% of adhered *E. coli* and *S. aureus*, respectively, when compared to the Desmo PU), demonstrating the physical durability of the surface. Even after 8 and 12 weeks of exposure in a chemical fume hood, the PU + 30% TTO samples show a significant reduction in adhered bacteria: at least 99% for both *E. coli* and *S. aureus*, when compared to the Desmo PU. In comparison, while the Epoxy + 30% TTO and PDMS + 30% TTO surfaces initially show a ~2 log reduction in adhered bacteria, the Epoxy +

30% TTO, 2 weeks and PDMS + 30% TTO, 2 weeks surfaces showed significant fouling. This can be attributed to the fact that tea tree oil does not chemically crosslink into epoxy and PDMS, and therefore, the free oil is not stabilized in the polymeric network.

In addition, the Desmo PU reacted with 30% TTO surfaces were shipped to an independent, third party laboratory for ISO 22196 testing. Figure 4.4 displays their results with our 30% TTO samples reducing the adhesion of both *E. coli* and *S. aureus*, respectively, by 99.998% (~4.8 log reduction) and >99.995% (>5.0 log reduction) Our preliminary results combined with the results from an official ISO 22196 test foreshadow a long lifetime for the antibacterial capabilities of this surface, much longer than any surface currently on the market. Please note that the TTO containing polyurethane can be applied on to any underlying substrate, including different metals, polymers, or glass, by a simple dip-, spray- or brush-coating.

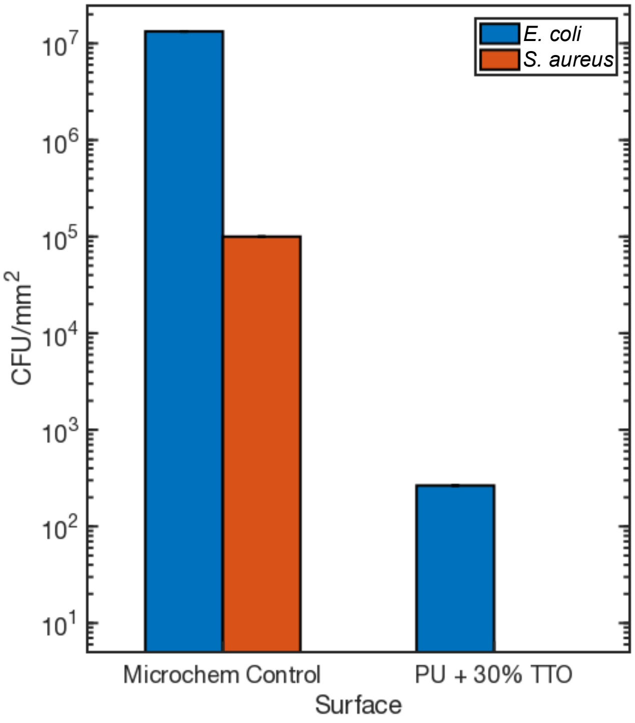

**Figure 4.4.** ISO 22196 test results as performed by Microchem Laboratory. Results indicate a 99.998% and a >99.995% reduction for *E. coli* and *S. aureus*, respectively, and are consistent with our antibacterial experiments.

Quantitative culture experiments were also used to evaluate abraded surfaces that have undergone 1000 abrasion cycles (0.26% mass loss over effectively 100 meters of abrasion) to mimic the wear and tear of everyday use. There was nearly no change in antibacterial properties with a 99.6% reduction (~2.8 log reduction) and 99.9% reduction (~4.1 log reduction) of adhered *E. coli* and *S. aureus*, respectively, when compared to the pure Desmo PU. These results indicate that the antibacterial performance of the surface will not falter even if it is scratched from every day use.

Alongside quantitative culture experiments, we utilized contact plating experiments to investigate how long it takes for the bactericidal properties of our surface to come into effect. Figure 4.5 displays the results of these experiments, with our 30% TTO surface showing a >99.99% reduction (>5 log reduction) in *E. coli* when compared to the pure PU.

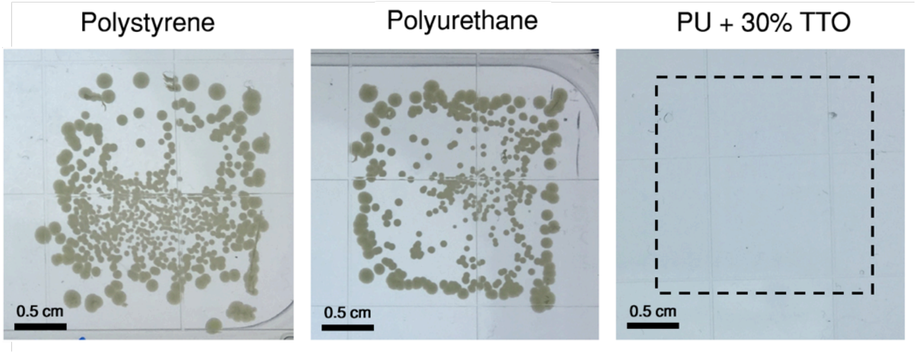

**Figure 4.5.** Contact plate experiments aimed at determining the time taken for the polyurethane crosslinked with tea tree oil surface to kill *S. aureus* bacteria. This image shows the total number of colonies of *S. aureus* that grow on an Agar plate after a 100,000 colonies of the bacteria come in contact with a polystyrene surface, a polyurethane surface or the same polyurethane surface crosslinked with tea tree oil for 10 minutes.

In just 10 minutes, our surface is capable of killing nearly all the bacteria it is exposed to, demonstrating its rapid effectiveness for real-time applications. Note that most antimicrobial wipes require a period of action of ~ 10 minutes. Thus, polyurethane surfaces with the crosslinked tea tree oil provide both immediate (microbial death in ~ 10 minutes) and persistent (after 12 weeks) antimicrobial effectiveness. We are unaware of any other active antimicrobial agent possessing both these typically disparate properties simultaneously. Note that apart from broad spectrum anti-bacterial properties[113], tea tree oil also possesses broad spectrum anti-fungal[121-125] and anti-viral[126-128] properties. Thus, we anticipate our tea tree oil containing polyurethane to similarly display anti-fungal and anti-viral properties.

Overall, because of their very unique and pertinent properties (immediate and persistent antimicrobial effectiveness, durability, broad spectrum anti-bacterial, anti-fungal and anti-viral), we believe the polyurethane – tea tree oil surfaces are ideally suited as antimicrobial coatings on different solid and porous substrates. We believe the approach of crosslinking a portion of the natural oil with a crosslinkable polymer network could be similarly used to fabricate antimicrobial surfaces using other volatile natural oils possessing antimicrobial properties. Such surfaces are expected to have a broad range of applications such as coatings for high touch areas within hospitals (to reduce hospital acquired infections), daycare facilities, retirement homes, coatings for sinks, furniture, and wall paint. Applications outside the healthcare space include antimicrobial coatings for touch screens (cell phones, tablets, displays), keyboards, computer mouse, shared automobiles, planes, trains, cruise liners, food contact areas in restaurants, food processing plants, and toilets amongst many others.

## 4.4 Conclusion

In this work, we present a novel antibacterial polymeric surface created by the addition of a volatile natural oil to a crosslinkable polymer, before the polymerization of the chain network. The polymeric network is chosen such that it can react with a portion of the chosen antibacterial natural oil. This results in a partial amount of 'free' oil stabilized by a fraction of the oil crosslinked into the network, thereby significantly reducing the evaporation rate of the oil from the surface. Our results and the results of the ISO 22196 testing indicate a reduction of adhered bacteria greater than 99% on the developed surfaces. Although most of the ‘free’ oil assembles at the surface, it does not quickly evaporate and even after 12 weeks of exposure to air, the surface still shows at least a 99% reduction in adhered bacteria when compared to a polyurethane without the natural oil. This surface is the first of its kind to exhibit exception mechanical durability as demonstrated by its abrasion resistance, as well as, immediate and persistent antimicrobial activity. We believe this approach could be similarly used to fabricate antimicrobial surfaces using other volatile natural oils possessing antimicrobial properties.

## 4.5 Acknowledgements

We thank the National Science Foundation Graduate Research Fellowship Program. This work was supported by the DOD OCRP Early Career Investigator Award W81XWH-13-1-0134 and DOD Pilot award W81XWH-16-1-0426. Research reported in this publication was supported by the National Cancer Institute of the National Institutes of Health under award number P30CA046592.

# Chapter 5. Summary and Future Work

## 5.1 Paper-Based Surfaces with Extreme Wettabilities for Novel, Open-Channel Microfluidic Devices

### *5.1.1 Fluoro-paper A*

With the ability to generate all four extreme wettabilities on fluoro-paper A, there are a plethora of future work applications available to explore. First, the generation of 2D and 3D channels, as shown in Figure 2.7, can be used to incorporate different biological assays on different sides of the paper-based device and can also be used to create hanging drops for 3D tumor research. It is well known that *in vitro* 2D cell cultures do not accurately predict *in vivo* 3D cell interactions, thus researchers have been striving to create *in vitro* 3D models for more accuracy. With a controlled amount of liquid, stable hanging drops can be fabricated on the 3D paper device and when seeded with cells, these hanging drops can be utilized not only for cancer tumor research, but possibly even for personalized point-of-care diagnostics.

Also, since Fluoro-paper A has been shown to continuously separate oil and water (Figure 2.10), devices can be engineered to explore any phase-based separations in protein chemistry, including removing nucleic acids away from the cytosome of the cell.

Additionally, surface emulsification for particle fabrication (Figure 2.15) can be used for single cell encapsulation. To enhance specific cancer treatments, researchers have focused on capturing single cancer cells to study population heterogeneity and to map individual cell responses. Also, this application could potentially be used to create an open-channel microfluidic polymerase chain reaction (PCR) device for point-of care diagnostics. With the expensive PCR reagents contained within the small, aqueous droplets, the outer fluid oil will act as a barrier to evaporation as the droplets float over heaters with pre-fixed temperatures to carry out the repeated polymerase chain reactions.[129, 130]

### *5.1.2 Fluoro-paper C*

This work shows the ability to pattern an isolated ovarian cancer cell line (Figure 2.19), and future work will involve growing out the individual cancer cells and specific cancer cell populations to study cell heterogeneity and to determine causes of differentiation. We envision that these devices would essentially rival Transwell® devices, permeable inserts that can be used to study cell-cell interaction without the two cell types physically interacting with each other.[131] With omniphilic domains patterned onto an omniphobic background, the air plastron will act as the physical barrier for the different cell types (Figure 5.1). However, the 3D network of the cellulose paper fibers in our device will more closely imitate the 3D network of *in vivo* cells when compared to the traditional 2D Transwell® device.

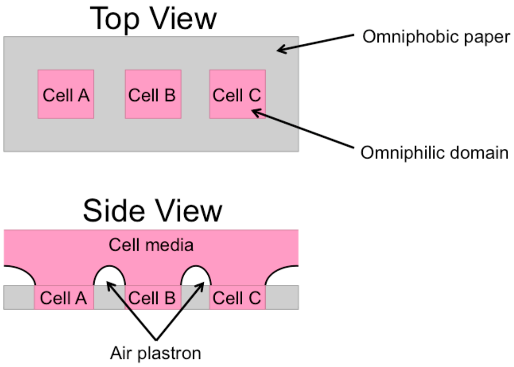

**Figure 5.1.** Top view and side view schematics of patterned fluoro-paper C being utilized as a Transwell® like device.

## 5.2 Lysis and Detection of Coliforms on a Printed Paper-based Microfluidic Device

This work demonstrates the detection of pathogenic *E. coli* on a cheap, all-in-one device and we envision that future work will involve creating multiplexed detection devices for point-of-care diagnostics. In particular, a device can be created to help detect and diagnose various bacterium causes of malaria, as shown in Figure 5.2. For example, Immunoglobin M (IgM) monoclonal anti- HRP-2 can be used to specifically identify *Plasmodium falciparum* as HRP-2 is not present in other malaria causing microorganisms.[132] However, this platform can be adapted to detect any bacterial disease by simply changing out the reagents seeded onto the paper, microfluidic device.

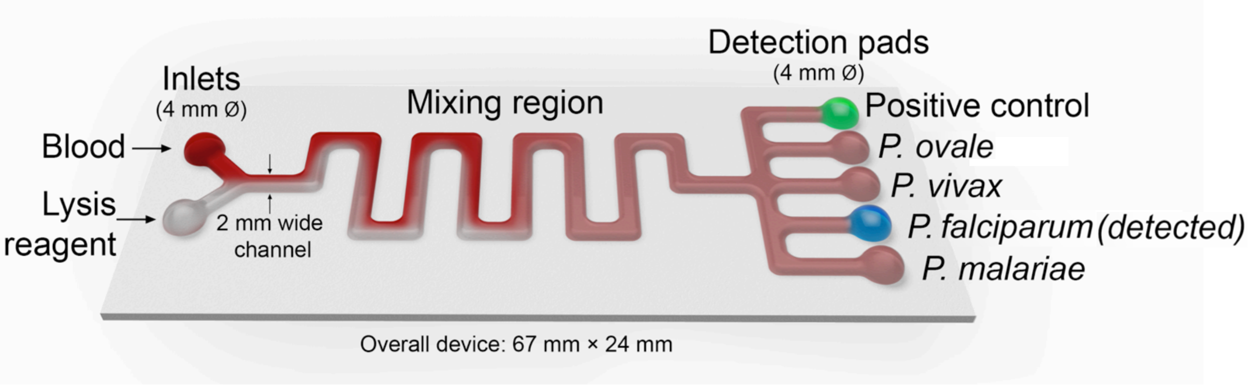
Inlets
(4 mm Ø)
Blood
Lysis reagent
2 mm wide channel
Mixing region
Detection pads
(4 mm Ø)
Positive control
P. ovale
P. vivax
P. falciparum (detected)
P. malariae
Overall device: 67 mm × 24 mm

**Figure 5.2.** Example schematic of malaria detection on an all-in-one, open-channel, paper-based microfluidic device.

## 5.3 Long Lasting Antimicrobial Surfaces Based on the Crosslinking of Natural Oils within Polymer Networks

Since the fabrication of this antimicrobial surface is so simple, there is an endless amount of possibilities in terms of surfaces to coat and future applications to explore. Most obviously, the surface production could be scaled up so that every door handle, steering wheel, bus seat, toilet seat, desk, kitchen counter, or any commonly used surface could be coated to prevent the spread of infectious disease. Additionally, this antimicrobial surface is currently being explored as a coating for wound dressings, eliminating the need of constant dressing replacement since the surface cannot get infected.

## 5.4 Closing Remarks

Surfaces with extreme wettabilities can be utilized for a wide range of biological applications. In the field of paper-based microfluidics, we have developed several different device fabrication methodologies and designs that can be applied to a plethora of biological applications including, but not limited to, cancer cell research, bacterial detection, and point-of-care diagnostics. In the field of anti-biofouling, we have designed an antimicrobial polyurethane based surface that remains antimicrobial after abrasion and after extended periods of time. While only a few specific applications have been presented, the amount of possible biological applications for surfaces with extreme wettabilities is endless and I look forward to seeing the future applications developed from this work.

# Appendix: Supplementary Information

## 1. Paper-Based Surfaces with Extreme Wettabilities for Novel, Open-Channel Microfluidic Devices

### *1.1 Capillary Flow on Multiplexed Fluoro-Paper A*

Seven different liquids were selected to demonstrate the capability of the $O_2$ plasma patterning technique, covering both polar and non-polar liquids, with surface tensions $\gamma_{lv}$ = 18.4–72.8 mN/m (at 20 °C) (Table 0.1).

**Table S.1.** Liquid properties (surface tension, viscosity, polarity index, boiling point) of the seven test liquids.

| | **Water** | **DMF** | **Chloroform** | **Acetone** | **Ethanol** | **Hexane** | **Hexadecane** |
|---|---|---|---|---|---|---|---|
| **Surface tension [mN/m at 20 °C]** | 72.8 | 36.8 | 27.2 | 23.3 | 22.3 | 18.4 | 27.5 |
| **Viscosity [mPa·s at 20 °C]** | 1.00 | 0.92 | 0.57 | 0.31 | 1.10 | 0.31 | 3.01 (25 °C) |
| **Polarity index** | 10.2 | 6.4 | 4.1 | 5.1 | 5.2 | 0.1 | 0.1 |
| **Boiling point [°C]** | 100.0 | 152.0 | 61.2 | 56.0 | 78.4 | 68.7 | 271.0 |

Seven straight channels 50 mm long × 2 mm wide were fabricated on each fluoro-paper A substrate (390 μm thick) (Methods; Figure 2.5). 20 μL droplets of each of the seven test liquids were then placed at the end of its corresponding channel, and the lateral flow behavior under room temperature and atmospheric pressure was observed (Figure 2.6a). Three parameters, which directly relate to device design and applications, were systematically studied: maximum wetting length in the channel (Table 2.3), average wetting velocity (maximum wetting length divided by the total wetting time) (Table 2.4), and wetting depth (the vertical distance the liquid wets into the channel) (Table 2.5, Figure 2.6b).

The wetting length of a liquid in a capillary tube is described by Washburn's equation as follows[133]

$$L^2 = \frac{\gamma D t \cos\theta}{4\eta}$$

here $L$ is the wetting length, $\gamma$ is the liquid surface tension, $D$ is the capillary diameter, $\theta$ is the contact angle, and $\eta$ is the viscosity of the liquid. If the capillary tube is fully wettable, $\theta = 0°$, and the average wetting velocity of capillary flow ($\Delta L/\Delta t$) for the seven test liquids should increase with increasing surface-tension to viscosity ratio ($\gamma / \eta$) as follows (Table VI): acetone > water > hexane > chloroform > DMF > ethanol > hexadecane.

However, etching fluoro-paper A for 5–900 sec did not produce a surface with simultaneously high wetting rates for all liquids, nor one that exhibited variation in wetting rates consistent with Washburn's equation. For all etching times, the channels exhibited some finite resistance to wetting by at least one of the liquids. This is further evidence for the fluorine redeposition effect that selectively reduces the wettability and wetting rates for nonpolar liquids after extended $O_2$ plasma etching times, rather than continually increasing the solid surface energy and thereby increasing the wetting rates for all liquids.

Moreover, it should be noted that, for each of the seven test liquids, the average wetting velocity (total wetting length $L$ divided by total time $t$) reached a peak value within the $O_2$ plasma etching times tested (Table 2.3). The decline in wetting rate after the peak value can be attributed to the fluorine recovery effect on wettability as discussed in the main manuscript.

A similar peak was also observed for maximum wetting length versus etching time for each liquid (Table 2.2). For certain liquids, especially those with relatively low boiling points, the maximum wetting length was found to be strongly influenced by evaporation. Acetone, chloroform, and hexane could not fill an entire 50 mm long channel with 20 μL of test liquid, even when their optimal wetting velocity was achieved. In comparison, liquids such as water, DMF, and ethanol with relatively high boiling points could fill 50 mm channels over a wide range of etching times (Table VI; Figure 2.6a).

### *1.2 Optimization of Three-dimensional Channels on Fluoro-Paper A*

First, a set of three-dimensional channels with one bridge each was prepared (Figure 2.8a). When added to one end of each of the channels, water, DMF, ethanol, and heptane all smoothly transferred through the bridge, reaching the other side (Figure 2.8b-d). The $O_2$ plasma etching (200 W) times for each single-bridge channel were 900 sec for water, 120 sec for DMF and ethanol, and 15 sec for heptane, longer than those required for simple two-dimensional channels. $O_2$ plasma power had to be increased to 350 W to produce three-dimensional channels with multiple bridges. A set of channels with two bridges each were prepared, and wetting time was characterized with the four test liquids previously mentioned. The etching times at 350 W were optimized so that the liquids would completely wet the channels in the minimum possible time: 300 sec for water, 60 sec for DMF, 15 sec for ethanol, and 30 sec for heptane.

Based on the optimized 350 W $O_2$ plasma treatment for channels with two bridges each, finally a set of channels with four bridges each was prepared with perpendicular channels underneath the bridges (Figure 2.7a-c). The optimized etching times for this geometry were: 180 sec for water channels, 60 sec for DMF channels, 30 sec for heptane channels, and 15 sec for ethanol channels.

# References

1. Tuteja, A., et al., *Robust omniphobic surfaces.* Proc Natl Acad Sci U S A, 2008. **105**(47): p. 18200-5.
2. Kobaku, S.P., et al., *Patterned superomniphobic-superomniphilic surfaces: templates for site-selective self-assembly.* Angew Chem Int Ed Engl, 2012. **51**(40): p. 10109-13.
3. Young, T., *An Essay on the Cohesion of Fluids.* Philosophical Transactions of the Royal Society of London, 1805. **95**: p. 65-87.
4. Gao, L. and T.J. McCarthy, *Contact Angle Hysteresis Explained.* Langmuir, 2006. **22**(14): p. 6234-6237.
5. Li, C., et al., *Paper-Based Surfaces with Extreme Wettabilities for Novel, Open-Channel Microfluidic Devices.* Advanced Functional Materials, 2016. **26**(33): p. 6121-6131.
6. Shuttleworth, R. and G.L.J. Bailey, *The spreading of a liquid over a rough solid.* Discussions of the Faraday Society, 1948. **3**: p. 16-22.
7. Johnson, R.E. and R.H. Dettre, *Contact Angle Hysteresis*, in *Contact Angle, Wettability, and Adhesion*, F.M. Fowkes, Editor. 1964, American Chemical Society: Washington, D.C. p. 112-144.
8. Wenzel, R.N., *Resistance of solid surfaces to wetting by water.* Industrial and Engineering Chemistry, 1936. **28**: p. 988-994.
9. Cassie, A.B.D. and S. Baxter, *Wettability of Porous Surfaces.* Transactions of the Faraday Society, 1944. **40**: p. 0546-0550.
10. Patankar, N.A., *On the Modeling of Hydrophobic Contact Angles on Rough Surfaces.* Langmuir, 2003. **19**: p. 1249-1253.
11. Marmur, A., *Wetting on Hydrophobic Rough Surfaces: To Be Heterogeneous or Not To Be?* Langmuir, 2003. **19**(20): p. 8343-8348.
12. Nosonovsky, M., *Multiscale roughness and stability of superhydrophobic biomimetic interfaces.* Langmuir, 2007. **23**(6): p. 3157-61.
13. Pan, S., et al., *Superomniphobic surfaces for effective chemical shielding.* J Am Chem Soc, 2013. **135**(2): p. 578-81.
14. Tuteja, A., et al., *Designing superoleophobic surfaces.* Science, 2007. **318**(5856): p. 1618-22.
15. Tuteja, A., et al., *Robust omniphobic surfaces.* Proceedings of the National Academy of Sciences of the United States of America, 2008. **105**(47): p. 18200-5.
16. Choi, W., et al., *Fabrics with Tunable Oleophobicity.* Advanced Materials, 2009. **21**(21): p. 2190-+.
17. Kota, A.K., et al., *Hygro-responsive membranes for effective oil-water separation.* Nature Communications, 2012. **3**: p. 1025.

18. Kobaku, S.P., et al., *Patterned superomniphobic-superomniphilic surfaces: templates for site-selective self-assembly.* Angewandte Chemie International Edition, 2012. **51**(40): p. 10109-13.
19. Kota, A.K., W. Choi, and A. Tuteja, *Superomniphobic surfaces: Design and durability.* MRS Bulletin, 2013. **38**(5): p. 383-390.
20. Kwon, G., E. Post, and A. Tuteja, *Membranes with selective wettability for the separation of oil–water mixtures.* MRS Communications, 2015. **5**(03): p. 475-494.
21. Rolland, J.P. and D.A. Mourey, *Paper as a novel material platform for devices.* MRS Bulletin, 2013. **38**(04): p. 299-305.
22. Martinez, A.W., et al., *Patterned paper as a platform for inexpensive, low-volume, portable bioassays.* Angew Chem Int Ed Engl, 2007. **46**(8): p. 1318-20.
23. Nge, P.N., C.I. Rogers, and A.T. Woolley, *Advances in microfluidic materials, functions, integration, and applications.* Chemical Reviews, 2013. **113**(4): p. 2550-2583.
24. Martinez, A.W., et al., *Diagnostics for the developing world: microfluidic paper-based analytical devices.* Analytical Chemistry, 2010. **82**(1): p. 3-10.
25. Martinez, A.W., *Microfluidic paper-based analytical devices: from POCKET to paper-based ELISA.* Bioanalysis, 2011. **3**(23): p. 2589-92.
26. Li, X., D.R. Ballerini, and W. Shen, *A perspective on paper-based microfluidics: Current status and future trends.* Biomicrofluidics, 2012. **6**(1): p. 11301-1130113.
27. Cate, D.M., et al., *Recent developments in paper-based microfluidic devices.* Analytical Chemistry, 2015. **87**(1): p. 19-41.
28. Carrilho, E., A.W. Martinez, and G.M. Whitesides, *Understanding Wax Printing A Simple Micropatterning Process for Paper Based Microfluidics.* Analytical Chemistry, 2009. **81**: p. 7091-7095.
29. Nie, Z., et al., *Electrochemical sensing in paper-based microfluidic devices.* Lab on a Chip, 2010. **10**(4): p. 477-83.
30. Li, X., et al., *Paper-based microfluidic devices by plasma treatment.* Analytical Chemistry, 2008. **80**(23): p. 9131-4.
31. Li, X., et al., *Fabrication of paper-based microfluidic sensors by printing.* Colloids and Surfaces B, 2010. **76**(2): p. 564-70.
32. Olkkonen, J., K. Lehtinen, and T. Erho, *Flexographically printed fluidic structures in paper.* Analytical Chemistry, 2010. **82**(24): p. 10246-50.
33. Cate, D.M., et al., *Simple, distance-based measurement for paper analytical devices.* Lab on a Chip, 2013. **13**(12): p. 2397-404.
34. Santhiago, M., et al., *Construction and electrochemical characterization of microelectrodes for improved sensitivity in paper-based analytical devices.* Analytical Chemistry, 2013. **85**(10): p. 5233-9.
35. Martinez, A.W., S.T. Phillips, and G.M. Whitesides, *Three-dimensional microfluidic devices fabricated in layered paper and tape.* Proceedings of the National Academy of Sciences of the United States of America, 2008. **105**(50): p. 19606-11.
36. Martinez, A.W., et al., *Programmable diagnostic devices made from paper and tape.* Lab on a Chip, 2010. **10**(19): p. 2499-504.
37. Lewis, G.G., M.J. DiTucci, and S.T. Phillips, *Quantifying analytes in paper-based microfluidic devices without using external electronic readers.* Angewandte Chemie International Edition, 2012. **51**(51): p. 12707-10.

38. Schilling, K.M., D. Jauregui, and A.W. Martinez, *Paper and toner three-dimensional fluidic devices: programming fluid flow to improve point-of-care diagnostics.* Lab on a Chip, 2013. **13**(4): p. 628-31.
39. Liu, H. and R.M. Crooks, *Three-dimensional paper microfluidic devices assembled using the principles of origami.* Journal of the American Chemical Society, 2011. **133**(44): p. 17564-6.
40. Ge, L., et al., *3D origami-based multifunction-integrated immunodevice: low-cost and multiplexed sandwich chemiluminescence immunoassay on microfluidic paper-based analytical device.* Lab on a Chip, 2012. **12**(17): p. 3150-8.
41. Yetisen, A.K., M.S. Akram, and C.R. Lowe, *Paper-based microfluidic point-of-care diagnostic devices.* Lab on a Chip, 2013. **13**(12): p. 2210-51.
42. Osborn, J.L., et al., *Microfluidics without pumps: reinventing the T-sensor and H-filter in paper networks.* Lab on a Chip, 2010. **10**(20): p. 2659-65.
43. Fu, E., et al., *Transport in two-dimensional paper networks.* Microfluidics and Nanofluidics, 2011. **10**(1): p. 29-35.
44. Spicar-Mihalic, P., et al., *CO2 laser cutting and ablative etching for the fabrication of paper-based devices.* Journal of Micromechanics and Microengineering, 2013. **23**(6): p. 067003.
45. Lisowski, P. and P.K. Zarzycki, *Microfluidic Paper-Based Analytical Devices (muPADs) and Micro Total Analysis Systems (muTAS): Development, Applications and Future Trends.* Chromatographia, 2013. **76**: p. 1201-1214.
46. Glavan, A.C., et al., *Omniphobic "RF Paper" Produced by Silanization of Paper with Fluoroalkyltrichlorosilanes.* Advanced Functional Materials, 2013. **24**(1): p. 60-70.
47. Wang, J., et al., *Hydrophobic sol-gel channel patterning strategies for paper-based microfluidics.* Lab on a Chip, 2014. **14**(4): p. 691-5.
48. Lan, W.J., et al., *Paper-based electroanalytical devices with an integrated, stable reference electrode.* Lab on a Chip, 2013. **13**(20): p. 4103-8.
49. Butt, H.-J., K. Graf, and M. Kappl, *Physics and Chemistry of Interfaces*. 3rd ed. 2013, Weinheim, Germany: Wiley-VCH.
50. Lai, J.N., et al., *Study on hydrophilicity of polymer surfaces improved by plasma treatment.* Applied Surface Science, 2006. **252**(10): p. 3375-3379.
51. Lam, Y.L., C.W. Kan, and C.W.M. Yuen, *Effect of plasma pretreatment on enhancing wrinkle resistant property of cotton fiber treated with BTCA and TiO2 System.* Journal of Applied Polymer Science, 2012. **124**(4): p. 3341-3347.
52. Morra, M., E. Occhiello, and F. Garbassi, *Surface characterization of plasma-treated PTFE.* Surface and Interface Analysis, 1990. **16**(1-12): p. 412-417.
53. Schutzius, T.M., et al., *Surface tension confined (STC) tracks for capillary-driven transport of low surface tension liquids.* Lab on a Chip, 2012. **12**(24): p. 5237-42.
54. Mary, P., V. Studer, and P. Tabeling, *Microfluidic droplet-based liquid-liquid extraction.* Analytical Chemistry, 2008. **80**(8): p. 2680-7.
55. Utada, A.S., et al., *Dripping, jetting, drops, and wetting: The magic of microfluidics.* MRS Bulletin, 2007. **32**(9): p. 702-708.
56. Anna, S.L., N. Bontoux, and H.A. Stone, *Formation of dispersions using "flow focusing" in microchannels.* Applied Physics Letters, 2003. **82**(3): p. 364.
57. Teh, S.Y., et al., *Droplet microfluidics.* Lab on a Chip, 2008. **8**(2): p. 198-220.

58. Joensson, H.N. and H. Andersson Svahn, *Droplet microfluidics--a tool for single-cell analysis.* Angewandte Chemie International Edition, 2012. **51**(49): p. 12176-92.
59. Simon, M.G. and A.P. Lee, *Microfluidic Droplet Manipulations and Their Applications*, in *Microdroplet Technology: Principles and Emerging Applications in Biology and Chemistry*, P. Day, A. Manz, and Y. Zhang, Editors. 2012, Springer-Verlag: New York. p. 23-50.
60. Zhao, B., J.S. Moore, and D.J. Beebe, *Surface-directed liquid flow inside microchannels.* Science, 2001. **291**(5506): p. 1023-6.
61. Kaigala, G.V., R.D. Lovchik, and E. Delamarche, *Microfluidics in the "open space" for performing localized chemistry on biological interfaces.* Angewandte Chemie International Edition, 2012. **51**(45): p. 11224-40.
62. Ueda, E. and P.A. Levkin, *Emerging applications of superhydrophilic-superhydrophobic micropatterns.* Advanced Materials, 2013. **25**(9): p. 1234-47.
63. Vasquez, G., E. Alvarez, and J.M. Navaza, *Tension of Alcohol + Water from 20 to 50 °C.* Journal of Chemical and Engineering Data, 1995. **40**: p. 611-614.
64. Croxen, M.A., et al., *Recent advances in understanding enteric pathogenic Escherichia coli.* Clinical microbiology reviews, 2013. **26**(4): p. 822-880.
65. Nugen, S.R. and A.J. Baeumner, *Trends and opportunities in food pathogen detection.* Anal Bioanal Chem, 2008. **391**(2): p. 451-4.
66. Shafiee, H., et al., *Paper and flexible substrates as materials for biosensing platforms to detect multiple biotargets.* Sci Rep, 2015. **5**: p. 8719.
67. Li, C.Z., et al., *Paper based point-of-care testing disc for multiplex whole cell bacteria analysis.* Biosens Bioelectron, 2011. **26**(11): p. 4342-8.
68. Park, T.S. and J.-Y. Yoon, *Smartphone Detection of Escherichia coli From Field Water Samples on Paper Microfluidics.* IEEE Sensors Journal, 2015. **15**(3): p. 1902-1907.
69. Govindarajan, A.V., et al., *A low cost point-of-care viscous sample preparation device for molecular diagnosis in the developing world; an example of microfluidic origami.* Lab Chip, 2012. **12**(1): p. 174-81.
70. Tallon, P., et al., *Microbial Indicators of Faecal Contamination in Water: A Current Perspective.* Water, Air, and Soil Pollution, 2005. **166**(1): p. 139-166.
71. Jokerst, J.C., et al., *Development of a paper-based analytical device for colorimetric detection of select foodborne pathogens.* Anal Chem, 2012. **84**(6): p. 2900-7.
72. Wang, J., et al., *Hydrophobic sol-gel channel patterning strategies for paper-based microfluidics.* Lab Chip, 2014. **14**(4): p. 691-5.
73. Zhang, Y., et al., *Paper-Based Hydrophobic/Lipophobic Surface for Sensing Applications Involving Aggressive Liquids.* Advanced Materials Interfaces, 2016. **3**(22): p. 1600672.
74. Yamada, K., et al., *Paper-based inkjet-printed microfluidic analytical devices.* Angew Chem Int Ed Engl, 2015. **54**(18): p. 5294-310.
75. Rajendra, V., et al., *Printing silicone-based hydrophobic barriers on paper for microfluidic assays using low-cost ink jet printers.* Analyst, 2014. **139**(24): p. 6361-5.
76. Glavan, A.C., et al., *Omniphobic "RFPaper" Produced by Silanization of Paper with Fluoroalkyltrichlorosilanes.* Advanced Functional Materials, 2014. **24**(1): p. 60-70.
77. Lan, W.J., et al., *Paper-based electroanalytical devices with an integrated, stable reference electrode.* Lab Chip, 2013. **13**(20): p. 4103-8.
78. Schutzius, T.M., et al., *Surface tension confined (STC) tracks for capillary-driven transport of low surface tension liquids.* Lab Chip, 2012. **12**(24): p. 5237-42.

79. Hashimoto, K., H. Irie, and A. Fujishima, *TiO2Photocatalysis: A Historical Overview and Future Prospects.* Japanese Journal of Applied Physics, 2005. **44**(12): p. 8269-8285.
80. Scriven, L.E. and C.V. Sternling, *The Marangoni Effects.* Nature, 1960. **187**: p. 186-188.
81. Deegan, R.D., et al., *Capillary flow as the cause of ring stains from dried liquid drops.* Nature, 1997. **389**(6653): p. 827-829.
82. Jobe, A. and S. Bourgeois, *Lac represser-operator interaction.* Journal of Molecular Biology, 1973. **75**(2): p. 303-313.
83. Glavan, A.C., et al., *Rapid fabrication of pressure-driven open-channel microfluidic devices in omniphobic RF paper.* Lab on a chip, 2013. **13**(15): p. 2922-2930.
84. Rompré, A., et al., *Detection and enumeration of coliforms in drinking water: current methods and emerging approaches.* Journal of microbiological methods, 2002. **49**(1): p. 31-54.
85. Banerjee, I., R.C. Pangule, and R.S. Kane, *Antifouling coatings: recent developments in the design of surfaces that prevent fouling by proteins, bacteria, and marine organisms.* Advanced Materials, 2011. **23**(6): p. 690-718.
86. Patel, P., C.K. Choi, and D.D. Meng, *Superhydrophilic surfaces for antifogging and antifouling microfluidic devices.* Journal of the Association for Laboratory Automation, 2010. **15**(2): p. 114-119.
87. Genzer, J. and K. Efimenko, *Recent developments in superhydrophobic surfaces and their relevance to marine fouling: a review.* Biofouling, 2006. **22**(5): p. 339-360.
88. Cassie, A. and S. Baxter, *Wettability of porous surfaces.* Transactions of the Faraday Society, 1944. **40**: p. 546-551.
89. Hou, S., et al., *Microtopographic patterns affect Escherichia coli biofilm formation on poly (dimethylsiloxane) surfaces.* Langmuir, 2011. **27**(6): p. 2686-2691.
90. Chung, K.K., et al., *Impact of engineered surface microtopography on biofilm formation of Staphylococcus aureus.* Biointerphases, 2007. **2**(2): p. 89-94.
91. Vasudevan, R., et al., *Microscale patterned surfaces reduce bacterial fouling-microscopic and theoretical analysis.* Colloids and Surfaces B: Biointerfaces, 2014. **117**: p. 225-232.
92. Bers, A.V. and M. Wahl, *The influence of natural surface microtopographies on fouling.* Biofouling, 2004. **20**(1): p. 43-51.
93. Lourenço, B.N., et al., *Wettability influences cell behavior on superhydrophobic surfaces with different topographies.* Biointerphases, 2012. **7**(1): p. 46.
94. Zhang, H., R. Lamb, and J. Lewis, *Engineering nanoscale roughness on hydrophobic surface—preliminary assessment of fouling behaviour.* Science and Technology of Advanced Materials, 2005. **6**(3): p. 236-239.
95. Leslie, D.C., et al., *A bioinspired omniphobic surface coating on medical devices prevents thrombosis and biofouling.* Nature biotechnology, 2014.
96. Krishnan, S., et al., *Comparison of the fouling release properties of hydrophobic fluorinated and hydrophilic PEGylated block copolymer surfaces: attachment strength of the diatom Navicula and the green alga Ulva.* Biomacromolecules, 2006. **7**(5): p. 1449-1462.
97. Chen, K., S. Zhou, and L. Wu, *Self-Healing Underwater Superoleophobic and Anti-Biofouling Coatings Based on the Assembly of Hierarchical Microgel Spheres.* ACS nano, 2015.

98. Page, K., M. Wilson, and I.P. Parkin, *Antimicrobial surfaces and their potential in reducing the role of the inanimate environment in the incidence of hospital-acquired infections.* Journal of Materials Chemistry, 2009. **19**(23): p. 3819-3831.
99. Friedlander, R.S., et al., *Bacterial flagella explore microscale hummocks and hollows to increase adhesion.* Proceedings of the National Academy of Sciences, 2013. **110**(14): p. 5624-5629.
100. Hammer, K.A., C.F. Carson, and T.V. Riley, *Antimicrobial activity of essential oils and other plant extracts.* Journal of applied microbiology, 1999. **86**(6): p. 985-990.
101. Nazzaro, F., et al., *Effect of essential oils on pathogenic bacteria.* Pharmaceuticals, 2013. **6**(12): p. 1451-1474.
102. Harkenthal, M., et al., *Comparative study on the in vitro antibacterial activity of Australian tea tree oil, cajuput oil, niaouli oil, manuka oil, kanuka oil, and eucalyptus oil.* Die Pharmazie, 1999. **54**(6): p. 460-463.
103. Swamy, M.K., M.S. Akhtar, and U.R. Sinniah, *Antimicrobial properties of plant essential oils against human pathogens and their mode of action: an updated review.* Evidence-Based Complementary and Alternative Medicine, 2016. **2016**.
104. Markus, A., et al., *Formulations containing microencapsulated essential oils*. 2015, Google Patents.
105. Nelson, G., *Application of microencapsulation in textiles.* International journal of pharmaceutics, 2002. **242**(1): p. 55-62.
106. María, M.M.S., et al., *Aroma Finishing of Cotton Fabrics by Means of Microencapsulation Techniques.* Journal of Industrial Textiles, 2010. **40**(1): p. 13-32.
107. Petri, M., et al., *Hard surface cleaning and disinfecting compositions comprising essential oils*. 2000, Google Patents.
108. de Oliveira, E.F., H.C.B. Paula, and R.C.M.d. Paula, *Alginate/cashew gum nanoparticles for essential oil encapsulation.* Colloids and Surfaces B: Biointerfaces, 2014. **113**(Supplement C): p. 146-151.
109. Liakos, I., et al., *All-natural composite wound dressing films of essential oils encapsulated in sodium alginate with antimicrobial properties.* International journal of pharmaceutics, 2014. **463**(2): p. 137-145.
110. Chifiriuc, C., et al., *Hybrid magnetite nanoparticles/Rosmarinus officinalis essential oil nanobiosystem with antibiofilm activity.* Nanoscale Research Letters, 2012. **7**(1): p. 209.
111. Pelissari, F.M., et al., *Antimicrobial, mechanical, and barrier properties of cassava starch− chitosan films incorporated with oregano essential oil.* Journal of Agricultural and Food Chemistry, 2009. **57**(16): p. 7499-7504.
112. Buchanan, M.S., *Fragrance-emitting polyurethane foams*. 1986, Google Patents.
113. Carson, C., K. Hammer, and T. Riley, *Melaleuca alternifolia (tea tree) oil: a review of antimicrobial and other medicinal properties.* Clinical microbiology reviews, 2006. **19**(1): p. 50-62.
114. Walker, M., *Clinical investigation of Australian Melaleuca alternifolia oil for a variety of common foot problems.* Curr. Podiatry, 1972. **1972**: p. 7-15.
115. Satchell, A.C., et al., *Treatment of interdigital tinea pedis with 25% and 50% tea tree oil solution: A randomized, placebo-controlled, blinded study.* Australasian journal of dermatology, 2002. **43**(3): p. 175-178.
116. Satchell, A.C., et al., *Treatment of dandruff with 5% tea tree oil shampoo.* Journal of the American Academy of Dermatology, 2002. **47**(6): p. 852-855.

117. Halcón, L. and K. Milkus, *Staphylococcus aureus and wounds: a review of tea tree oil as a promising antimicrobial.* American Journal of Infection Control, 2004. **32**(7): p. 402-408.
118. Sailer, R., et al., *Pharmaceutical and medicinal aspects of Australian tea tree oil.* Phytomedicine, 1998. **5**(6): p. 489-495.
119. *FDA Executive Summary: Classification of Wound Dressings Combined with Drugs*. Prepared for the Meeting of the General and Plastic Surgery Devices Advisory Panel September 20-21, 2016.
120. Marchese, A., et al., *Update on monoterpenes as antimicrobial agents: A particular focus on p-cymene.* Materials, 2017. **10**(8): p. 947.
121. Bassett, I., D. Pannowitz, and R. Barnetson, *A comparative study of tea-tree oil versus benzoylperoxide in the treatment of acne.* The Medical Journal of Australia, 1990. **153**(8): p. 455-458.
122. Christoph, F., P.-M. Kaulfers, and E. Stahl-Biskup, *A comparative study of the in vitro antimicrobial activity of tea tree oils sl with special reference to the activity of β-triketones.* Planta Medica, 2000. **66**(06): p. 556-560.
123. D'auria, F., et al., *In vitro activity of tea tree oil against Candida albicans mycelial conversion and other pathogenic fungi.* Journal of chemotherapy, 2001. **13**(4): p. 377-383.
124. Nenoff, P., U.-F. Haustein, and W. Brandt, *Antifungal activity of the essential oil of Melaleuca alternifolia (tea tree oil) against pathogenic fungi in vitro.* Skin Pharmacology and Physiology, 1996. **9**(6): p. 388-394.
125. Rushton, R., et al., *The effect of tea tree oil extract on the growth of fungi.* Lower Extremity, 1997. **4**: p. 113-116.
126. Bishop, C.D., *Antiviral activity of the essential oil of Melaleuca alternifolia (Maiden amp; Betche) Cheel (tea tree) against Tobacco Mosaic Virus.* Journal of Essential Oil Research, 1995. **7**(6): p. 641-644.
127. Schnitzler, P., K. Schön, and J. Reichling, *Antiviral activity of Australian tea tree oil and eucalyptus oil against herpes simplex virus in cell culture.* Die Pharmazie, 2001. **56**(4): p. 343-347.
128. Minami, M., et al., *The inhibitory effect of essential oils on herpes simplex virus type-1 replication in vitro.* Microbiology and immunology, 2003. **47**(9): p. 681-684.
129. Li, C., M. Boban, and A. Tuteja, *Open-channel, water-in-oil emulsification in paper-based microfluidic devices.* Lab on a Chip, 2017. **17**(8): p. 1436-1441.
130. Park, S., et al., *Advances in microfluidic PCR for point-of-care infectious disease diagnostics.* Biotechnology Advances, 2011. **29**(6): p. 830-839.
131. Marshall, J., *Transwell® invasion assays.* Cell Migration: Developmental Methods and Protocols, 2011: p. 97-110.
132. Moody, A., *Rapid Diagnostic Tests for Malaria Parasites.* Clinical Microbiology Reviews, 2002. **15**(1): p. 66.
133. Washburn, E.W., *The dynamics of capillary flow.* Physical Review, 1921. **17**(3): p. 273-283.